Coherent Rayleigh time domain reflectometry: novel applications for optical fibre sensing

THÈSE N^{O} 7104 (2016)

PRÉSENTÉE LE 29 SEPTEMBRE 2016

À LA FACULTÉ DES SCIENCES ET TECHNIQUES DE L'INGÉNIEUR

GROUPE SCI STI LT

PROGRAMME DOCTORAL EN PHOTONIQUE

ÉCOLE POLYTECHNIQUE FÉDÉRALE DE LAUSANNE

POUR L'OBTENTION DU GRADE DE DOCTEUR ÈS SCIENCES

PAR

Xin LU

acceptée sur proposition du jury:

Prof. C. S. Brès, présidente du jury
Prof. L. Thévenaz, directeur de thèse
Prof. M. Gonzalez-Herraez, rapporteur
Prof. L. Palmieri, rapporteur
Dr H. Limberger, rapporteur

ÉCOLE POLYTECHNIQUE
FÉDÉRALE DE LAUSANNE

Suisse
2016

Acknowledgement

Life as a doctor student is never easy, and it can be even more difficult without the support and help from my supervisor, colleagues, friends and family.

First and foremost, I would like to express my gratefulness to my supervisor, Prof. Luc Thévenaz, for his constant guidance and encouragement throughout my academic studies. I appreciate his advice and encouragement for professional and personal lives.

Besides my respectful supervisor, I gratefully acknowledge Prof. Miguel González-Herráez from University of Alcalá for his helpful suggestions on distributed fibre sensing and being my jury member. I would also like to thank other jury members: Prof. Luca Palmieri from University of Padova, MER Dr. Hans Limberger from EPFL and Prof. Camille-Sophie Brès from EPFL who is the present of the thesis jury.

My appreciation is extended to the former and current colleagues in the Group for Fibre Optics at EPFL: postdoctoral fellow Marcelo Soto and Kenny Hey Tow, and doctor assistant Nikoley Primerov, Andrey Denisov, Mehdi Alem, Flavien Gyger and Desmond Chow for their discussion and endless help about life and science. My thanks also go to our visitors: Prof. Pingyu Zhu from Guangzhou University, Zhisheng Yang from Beijing University of Posts and Telecommunications, Zhiyong Zhao from Huazhong University of Science and Technology, Liang Zhang from Shanghai Jiao Tong University and Wei Chen from National University of Defense Technology. Special thanks to Hugo Martins from University of Alcalá for working on the birefringence measurement.

In addition, I acknowledge the former and current administrative assistants in the Group for Fibre Optics and the doctoral program in photonics, Alexandra Morrison, Svetlana Machkina, Pierrette Paulou-Vaucher and Cathy Buchs for helping me with all the paperwork.

I am very thankful to Dr. Kay Schuster from IPHT Jena for providing an ORMOCER® coated fibre which was used in temperature sensing, and AMS Technologies and Fiberguide for providing the Al-coated fibre for electrical heating.

Last but not least, my parents deserve my deepest gratitude for their unconditional love and continuous support throughout my life.

Abstract

A distributed optical fibre sensor is a system that exploits an optical fibre as the sensing medium to realise continuous measurements in temporal and spatial domains. This type of sensor demonstrates a wide range of applications owing to its advantages, such as lightweight, small size, low cost and immunity to electromagnetic interferences. So far, fibre sensors have been applied in diverse fields and the scientific research on fibre sensing keeps improving to meet new industrial demands. In this thesis, a novel distributed fibre sensor based on coherent Rayleigh scattering is investigated to realise best accuracy measurements.

After introducing several optical effects related to fibre sensing, coherent Rayleigh scattering is thoroughly studied. It is found to be essentially assimilated to a random walk process, thus its statistical properties are theoretically analysed based on the mature theory on random walk. Then the spectral characteristics of the Rayleigh backscattered light is investigated for different incident pulse shapes. The spectral distribution of the trace amplitude turns out to be identical to the spectrum of the incident pulse. Meanwhile, a theoretical model is proposed to describe the coherent Rayleigh trace in time and frequency domains. Experiments are carried out to validate the theoretical analysis and the proposed model. Then the statistical properties and the visibility of the coherent Rayleigh traces obtained by experiment and simulation are investigated for different detection bandwidth. The minimum 3 dB bandwidth required to resolve all features of a coherent Rayleigh intensity trace is determined to be 2 times larger than the bandwidth of the incident rectangular pulse.

Then coherent Rayleigh scattering is applied to distributed sensing using the optical time-domain reflectometry technique. The working principle is explained by the restorability of the Rayleigh trace in time domain and by a spectral shift in frequency domain, in total similarity with a fibre Bragg grating sensor. The temperature sensitivity is calculated over a wide range from 300 K down to 4.5 K based on the thermo-optic effect and the thermal expansion of the silica fibre. The experimental results in a standard fibre with acrylate coating and a fibre specially coated with ORMOCER® confirm the high temperature sensitivity (over 1 GHz/K) obtained by the theoretical analysis and demonstrate a temperature resolution in the milliKelvin range even under cryogenic conditions, enabling this sensor for very precise measurements. The fibre with the ORMOCER® coating exhibits a higher temperature sensitivity at room temperature than the acrylate coated fibre due to the extra strain induced by the temperate change in the coating and a more stable sensing behaviour because the polymers forming the coating stabilise the mechanical and thermal responses of the fibre.

The sensors based on coherent Rayleigh scattering are also applied to retrieve the phase birefringence distribution along polarisation-maintaining and standard single mode fibres since it is able to measure the small refractive index changes induced by birefringence. The minimum detectable birefringence reaches 3×10^{-7} when the spatial resolution is 2 m and even smaller value can be resolved using longer optical pulses. In addition, this birefringence measurement is capable of distributed temperature and strain sensing in a PANDA and an elliptical-core polarisation-maintaining fibres since the birefringence is sensitive to environmental variations. The experimental results demonstrate that this method is one order of magnitude more sensitive than a fibre

sensor based on Brillouin scattering. Moreover, discriminated temperature and strain sensing is realised by a combination of this birefringence measurement and a standard COTDR sensor.

This thesis is concluded by a discussion of further research directions on coherent Rayleigh scattering based distributed sensing.

Keywords : fibre optics, Rayleigh scattering, distributed fibre sensing, birefringence measurement

Résumé

Un capteur réparti à fibre optique est un système qui exploite une fibre optique en tant que milieu sensible, pour réaliser des mesures en continu le long de la fibre dans les domaines temporel et spatial. Ce type de capteur démontre une large gamme d'applications en raison de ses avantages propres, tels que poids léger, petite taille, faible coût et immunité aux interférences électromagnétiques. A ce jour, les capteurs à fibres ont été employés dans des domaines très divers et la recherche scientifique sur les capteurs à fibre s'efforce constamment de trouver des solutions innovantes pour répondre aux nouvelles exigences de l'industrie. Dans cette thèse, un capteur réparti à fibre, basé sur la diffusion Rayleigh cohérente, est mis en œuvre pour réaliser des mesures de meilleure précision, à la pointe de la recherche.

Après avoir présenté les effets optiques qui importent pour les capteurs à fibre, la diffusion Rayleigh cohérente est étudiée en profondeur. Sa réponse se trouve être fondamentalement assimilable à un processus de marche aléatoire; ainsi, ses propriétés statistiques sont théoriquement analysées dans le cadre de la théorie bien établie de la marche aléatoire. Ensuite, le spectre de la lumière Rayleigh rétrodiffusée est étudié pour différentes formes d'impulsion incidente. La distribution spectrale de l'amplitude de la trace se révèle être identique au spectre de l'impulsion incidente. En parallèle, un modèle théorique est proposé pour décrire la trace Rayleigh cohérente dans les domaines temporel et fréquentiel. Des expériences ont été réalisées pour valider l'analyse théorique et le modèle proposé. Ensuite, les propriétés statistiques et la visibilité des traces Rayleigh cohérentes obtenues expérimentalement et par simulation sont étudiées pour différentes bandes passantes de détection. La bande passante minimale à 3 dB, requise pour résoudre toutes les variations d'intensité sur une trace Rayleigh cohérente, est établie comme devant être 2 fois plus élevée que la largeur de bande de l'impulsion rectangulaire incidente.

Ensuite, la diffusion Rayleigh cohérente est appliquée à la détection répartie continue en utilisant la technique de réflectométrie optique dans le domaine temporel. Le principe de fonctionnement est justifié par la possibilité de restaurer la trace Rayleigh dans le domaine temporel par un décalage spectral dans le domaine des fréquences, en similarité totale avec un capteur à réseau de Bragg en fibre. La sensibilité à la température est calculée sur une large gamme allant de 300 K à 4,5 K, basée sur l'effet thermo-optique et la dilatation thermique de la fibre en silice. Les résultats expérimentaux, dans une fibre standard avec un revêtement d'acrylate et d'une fibre spécialement revêtue d'ORMOCER®, confirment la grande sensibilité à la température (au-dessus de 1 GHz/K) obtenue par l'analyse théorique et présentent une résolution de température dans la gamme du milliKelvin, ce qui permet à ces capteurs d'effectuer des mesures très précises, même dans un environnement cryogénique. La fibre avec le revêtement ORMOCER® présente une réponse thermique supérieure à température ambiante, par rapport à une fibre revêtue d'acrylate. Ceci est dû à la contrainte supplémentaire induite dans le revêtement par le changement de température, en sus d'une réponse thermique plus uniforme provenant d'une meilleure stabilité mécanique et thermique des polymères formant ce type de revêtement.

Les capteurs basés sur la diffusion Rayleigh cohérente ont été également mis en œuvre pour extraire la distribution de biréfringence de phase le long des fibres à maintien de polarisation, ainsi que des fibres

unimodales standards. Ceci est rendu possible en raison de la capacité de ces capteurs à mesurer de faibles variations d'indice de réfraction, telles que celles induites par la biréfringence. La biréfringence minimale détectable atteint 3×10^{-7} pour une résolution spatiale de 2 m, et une encore meilleure résolution peut être obtenue en utilisant des impulsions optiques de plus longue durée. Par ailleurs, puisque la biréfringence est sensible aux variations des conditions ambiantes, cette mesure de biréfringence peut évaluer la distribution de température et de contrainte le long de fibres à maintien de polarisation, de type PANDA ou à cœur elliptique. Les résultats expérimentaux démontrent que cette méthode est d'un ordre de grandeur plus sensible qu'un capteur à fibre basé sur la diffusion Brillouin. De plus, les effets de température et de contrainte ont été discriminés en combinant cette mesure de la biréfringence avec celle obtenue par la technique standard COTDR.

Cette thèse se termine par une discussion sur les nouvelles orientations de recherche pour les capteurs répartis basés sur la diffusion Rayleigh cohérente.

Mots-clés : fibre optique, la diffusion Rayleigh, distribuée de détection de la fibre, la mesure de la biréfringence

Contents

Acknowledgement i

Abstract iii

Résumé v

List of Figures xi

List of Tables xv

Chapter 1 Introduction 1

Chapter 2 Fundamentals of Optical Time Domain Reflectometry 5

2.1 Light propagation and some properties ... 5

2.1.1 Perturbed wave equation ... 6

2.1.2 Coherence of light ... 6

2.1.3 Polarisation of light ... 7

2.2 Spontaneous light scattering ... 9

2.2.1 Rayleigh scattering ... 10

2.2.2 Spontaneous Brillouin scattering ... 11

2.2.3 Spontaneous Raman scattering ... 14

2.3 Optical time domain reflectometry ... 15

2.3.1 Working principle of an optical time domain reflectometry ... 15

2.3.2 Temperature sensing based on the standard OTDR ... 17

2.3.3 Polarisation optical time domain reflectometry ... 17

2.3.4 Coherent optical time domain reflectometry ... 18

2.3.5 Brillouin optical time domain reflectometry ... 18

2.3.6 Raman optical time-domain reflectometry ... 19

2.4 Nonlinear processes in the fibre ... 20

2.4.1 Self-phase modulation ... 21

2.4.2 Modulation instability ... 21

2.4.3 Four-wave mixing ... 21

2.4.4 Stimulated Brillouin scattering ... 22

2.4.5 Stimulated Raman scattering ... 23

Chapter 3 Properties of Coherent Optical Time Domain Reflectometry 25

3.1 Theoretical model for coherent Rayleigh scattering ... 26

3.2 Temporal properties of coherent Rayleigh traces 28
3.2.1 Theory of the statistical properties of COTDR traces 28
3.2.2 Simulation and experiment for the temporal property of coherent Rayleigh trace 31
3.3 Spectral properties of coherent Rayleigh traces 33
3.3.1 Theory of the spectral feature of COTDR trace 33
3.3.2 Experiment and simulation of the spectral properties of COTDR trace 35
3.3.3 Effects of photodetector bandwidth on the COTDR trace 38
3.3.4 Conclusions 40
3.4 Sensing range increase for COTDR 41
3.4.1 Pre-amplification for a COTDR system 42
3.4.2 In-line Brillouin amplification for a COTDR system 43
3.4.3 Conclusions 45
Chapter 4 Coherent Optical Time Domain Reflectometry for Distributed Sensing 47
4.1 Working principle of a COTDR sensor 48
4.1.1 Working theory of a FBG sensor 48
4.1.2 Sensing theory of a COTDR sensor 49
4.1.3 Sensitivity of a COTDR fibre sensor 51
4.1.4 Simulation of distributed temperature sensing based on COTDR 56
4.1.5 Conclusion 57
4.2 Experimental validation 57
4.2.1 Laser frequency stabilisation 57
4.2.2 Experimental setup 59
4.2.3 Experiment result at room temperature 61
4.2.4 Experimental results at cryogenic temperatures 65
4.2.5 Conclusion 69
4.3 Fibre heating methods 69
4.3.1 Optical heating 70
4.3.2 Electrical heating 72
4.3.3 Experiment validation for electrical heating 74
4.3.4 Conclusion 77
Chapter 5 Distributed Fibre Sensing Based on Coherent Rayleigh Scattering Measurements of Birefringence 79
5.1 COTDR for birefringence measurement 79
5.1.1 Working principle for birefringence measurement 80
5.1.2 Birefringence measurement for PM fibres 81
5.1.3 Birefringence measurement for standard SMFs 85
5.1.4 Alternative scheme for measuring standard SMFs 87

5.1.5 Conclusion 89
5.2 Fibre sensing based on the birefringence measurement 89
5.2.1 Experiment and results 90
5.2.2 Discrimination of temperature and strain 93
5.2.3 Conclusion 96
Chapter 6 Conclusions and Perspectives 97
6.1 Main contributions 97
6.2 Future work 98
Appendix 101
Bibliography 103
List of Acronyms 111
List of Symbols 113

List of Figures

Figure 2-1. State of polarisation changes randomly in the standard fibre. 8

Figure 2-2. Different types of polarisation-maintaining fibres. 8

Figure 2-3. Different scattering processes inside the optical fibre. 9

Figure 2-4. Radiation of the oscillating dipole caused by incident electric field. 10

Figure 2-5. Momentum conservation for (a) Stokes and (b) anti-Stokes components of Brillouin scattering. 13

Figure 2-6. Energy level diagrams for Raman (a) Stokes and (b) anti-Stokes scattering. 14

Figure 2-7. Typical OTDR system. 15

Figure 2-8. Propagation of an optical pulse in the fibre and its Rayleigh scattered light at time (a) t_0, (b) t_0+t' and (c) $t_0+\tau_w/2$. 16

Figure 2-9. An OTDR trace of 50 km fibre measured by Anritsu MT9083A2. 17

Figure 2-10. Reported result on the temperature dependence of (a) Brillouin frequency shift and (b) Brillouin linewidth of a standard single mode fibre [46]. 19

Figure 2-11. Normalised ratio of anti-Stokes and Stokes waves as a function of the fibre temperature. 20

Figure 3-1. Typical coherent Rayleigh trace. 25

Figure 3-2. Discrete 1D model for coherent Rayleigh scattering. 26

Figure 3-3. Scheme of random process in case of (a) destructive and (b) constructive resultant. 27

Figure 3-4. The simulated coherent Rayleigh trace shows dependence on (a) optical frequency and (b) refractive index. 28

Figure 3-5. Experimental setup to validate the temporal property of the coherent Rayleigh trace. DFB: distributed feedback laser, EOM: electro-optic modulator, EDFA: erbium-doped fibre amplifier, AWG: arbitrary waveform generator, PC: polarisation controller, BPF: band pass filter, FBG: fibre Bragg grating. 32

Figure 3-6. Probability density of coherent Rayleigh trace in (a) amplitude and (b) intensity. 32

Figure 3-7. Detection scheme to obtain the spectrum of coherent Rayleigh trace. ESA: electric spectrum analyser, OSA: optical spectrum analyser. 36

Figure 3-8. Generated (a) rectangular and (b) sinc optical pulse. 36

Figure 3-9. (a) Amplitude and (b) intensity spectra of a COTDR trace with a 10-ns rectangular input pulse. 37

Figure 3-10. (a) Amplitude and (b) intensity spectra of a COTDR trace with a 10-ns sinc input pulse, inset is the intensity spectrum in linear scale. 37

Figure 3-11. Probability distribution of COTDR intensity trace with 10-ns incident pulse obtained with a photodetector bandwidth of (a) 1GHz, (b) 250 MHz, (c) 125 MHz and (d) 50 MHz. 39

Figure 3-12. Influence of bandwidth on the visibility of the coherent Rayleigh trace obtained by (a) simulation and (b) experiment. 40

Figure 3-13. Averaged visibility of the simulated and experimental coherent Rayleigh trace under different bandwidth. 40

Figure 3-14. Coherent Rayleigh trace for 50 km fibre. Inset, zoom in of the end of the fibre. 41

Figure 3-15. Pre-amplified 50 km coherent Rayleigh trace under different condition. Inset: end of the fibre. (a) high noise EDFA and broad FBG, (b) high noise EDFA and narrow FBG, (c) low noise EDFA and broad FBG, (d) low noise EDFA and narrow FBG. 42

Figure 3-16. Visibility of the coherent Rayleigh trace pre-amplified by (a) high noise EDFA and (b) low noise EDFA. 43

Figure 3-17. Experimental setup of the COTDR with Brillouin amplification. LD: laser diode, EOM: electro-optic modulator, EDFA: erbium-doped fibre amplifier, SOA: semiconductor optical amplifier. 44

Figure 3-18. (a) Amplified trace and (b) optical spectrum at the far end of fibre in the case of forward Brillouin amplification. 45

Figure 3-19. Amplified trace by backward Brillouin amplification. 45

Figure 4-1. Typical structure of a fibre Bragg grating and its spectral response. 48

Figure 4-2. Reflection spectra of a fibre Bragg grating under different temperature conditions. 49

Figure 4-3. Simulation of the restorability of the coherent Rayleigh trace. 50

Figure 4-4. (a) Frequency spectrum of the coherent Rayleigh scattered light at a given position and (b) cross-correlation result of the simulated spectra. 50

Figure 4-5. Principle of fibre sensing based on the coherent Rayleigh scattering. 51

Figure 4-6. Refractive index of Corning 7980 fused silica at 1534 nm obtained by the Sellmeier model [92]. 53

Figure 4-7. Thermo-optic coefficient and thermal expansion coefficient as function of temperature. 54

Figure 4-8. Calculated result of the thermal sensitivity at different temperature. 54

Figure 4-9. Comparison of the temperature induced frequency shift obtained by theory and reported result in the temperature range from 300 K to 4.2 K. 55

Figure 4-10. Simulation of temperature sensing. (a) Cross-correlation result, and (b) frequency shift as function of distance, inset: the temperature change at 964 m. 56

Figure 4-11. Laser frequency stabilisation. (a) Implemented scheme and (b) absorption spectrum of acetylene gas used for the locking system, inset: cross-section of the used hollow-core photonic crystal fibre. 58

Figure 4-12. Experimental demonstration of the laser frequency stabilisation scheme. 58

Figure 4-13. Implemented COTDR system for distributed temperature sensing. 59

Figure 4-14. Copper box used to provide a stable and uniform temperature distribution along the sensing fibre. A thermal resistor is placed inside to monitor the fibre temperature required in the characterisation. 60

Figure 4-15. Container for cryogenic measurement when the copper box is (a) immersed in and (b) hung above the liquid Nitrogen. 60

Figure 4-16. Restorability of the coherent Rayleigh trace obtained experimentally. 61

Figure 4-17. Cross-correlation between two successive measurements with a small temperature change, inset: quadratic fitting of the correlated peak. 62

Figure 4-18. Frequency shift versus temperature change for different fibres at room temperature. 62

Figure 4-19. Longitudinal section of a coated fibre. 63

Figure 4-20. Comparison of the temperature change measured by COTDR and Pt-1000 in thermal cycles. 64

Figure 4-21. Cross-correlation result for 2 km standard SMF, inset: enlarged view of the hot spot. 64

Figure 4-22. Cross-correlation result for 50 km standard SMF with pre-amplification. 65

Figure 4-23. Measured frequency variation when temperature changes around 80 K with (a) negative and (b) positive steps. 66

Figure 4-24. Frequency shift measured for both kinds of fibres when the fibre temperature is increased at around (a) 102 K, (b) 133 K, (c) 210 K and (d) 250 K. 67

Figure 4-25. Temperature sensitivity of both fibres obtained by the implemented COTDR sensor at different temperatures. 68

Figure 4-26. Comparison of the sensitivities obtained by the experiment and the theory for the ORMOCER® coated fibre... 68

Figure 4-27. Temperature resolution obtained by the implemented COTDR sensor in the thermal cycle. 69

Figure 4-28. Thermal transfer in optical heating, the heat generated in fibre core transfers to cladding and finally dissipates into the air. 70

Figure 4-29. Thermal distribution of optical heating under different convection along the fibre at (a) 300 K and (b) 77 K. the heating is more efficient at cryogenic condition or in vacuum. 71

Figure 4-30. Theoretical comparison of thermal distribution along an optical fibre at 77 K using both single and dual pumping scheme..... 72

Figure 4-31. Thermal transfer in electrical heating: thermal energy generated in the metal coating transfers to the fibre and raises the temperature and the rest dissipates into the air. 73

Figure 4-32. Increased temperature of Al coated fibre under different current and thermal conditions at (a) ambient pressure and (b) very low pressure. 74

Figure 4-33. Frequency scanning of the probe to obtain Brillouin frequency in a Brillouin optical time domain analyser..... 75

Figure 4-34. Experimental setup to validate the electrical heating by a double-pulse Brillouin optical time domain analyser. 75

Figure 4-35. Brillouin frequency shift versus temperature change for Al-coated optical fibre..... 76

Figure 4-36. (a) Measured Brillouin frequency and (b) averaged Brillouin spectrum along the Al-coated fibre with different electrical power. 77

Figure 4-37. Comparison of experimental result and simulation for electrical heating. 77

Figure 5-1. Experimental setup to measure the birefringence distribution along the PM fibre. DFB: distributed-feedback laser, SOA: semiconductor optical amplifier, EOM: electro-optic modulator, FBG: fibre Bragg grating, EDFA: erbium-doped fiber amplifier, BPF: band pass filter, PSw: polarisation switch, PC: polarisation controller, FUT: fibre under test. 82

Figure 5-2. Measured phase birefringence distribution along (a) a 90 m PANDA and (b) a 100 m elliptical-core PM fibres. Left-hand side vertical axis: Measured frequency shift. Right-hand side vertical axis: Birefringence value calculated using Eq. 5-5. 83

Figure 5-3. A Sagnac loop to validate the birefringence measurement based on coherent Rayleigh scattering. PC: polarisation controller, OSA: optical spectrum analyser. 83

Figure 5-4. Output of the Sagnac loop with PANDA fibre at 1534 nm. 84

Figure 5-5. Cross-correlation result for a Philips fibre. 85

Figure 5-6. Distributed profile of phase birefringence versus distance along (a) a Cabloptic IV and (b) a Philips I SMFs. 86

Figure 5-7. Proposed scrambling module to generate two incoherent lightwaves: (a) scheme using an unbalanced Mach-Zehnder interferometer, (b) scheme using a PM mirror and a Faraday mirror. PM: polarisation-maintaining, and PC: polarisation controller. 87

Figure 5-8. Distributed profile of phase birefringence versus distance along a (a) Cableoptic IV and a (b) Philips I SMFs, obtained from the auto-correlation of a single Rayleigh measurement. 88

Figure 5-9. Correlation spectrum of Cableoptic IV at a position of 200 m. 89

Figure 5-10. Experimental setup for distributed sensing based on birefringence measurement. OSA: optical spectrum analyser, EOM: electro-optic modulator, PM: polarisation maintaining, BPF: band pass filter, EDFA: erbium-doped fiber amplifier, PC: polarisation controller. 90

Figure 5-11. (a) Obtained Rayleigh trace for both axes and (b) cross-correlation result of Rayleigh trace. 91

Figure 5-12. Frequency shift versus distance under different (a) temperature and (b) strain conditions for the elliptical core PM fibre. 91

Figure 5-13. Measured frequency shift versus (a) temperature and (b) strain for the elliptical core PM fibre. 92

Figure 5-14. Measured frequency shift versus (a) temperature and (b) strain for a PANDA PM fibre. 92

Figure 5-15. Temperature sensitivity measured in PM fibres with different birefringence. 93

Figure 5-16. (a) Temperature and (b) strain sensitivities of the elliptical-core PM fibre measured by a COTDR sensor. 94

Figure 5-17. (a) Frequency shift obtained from a standard COTDR sensor and (b) frequency difference of birefringence measurements. 95

Figure 5-18. Retrieved (a) temperature and (b) strain variation profiles along the elliptical core PM fibre. 95

Figure A-1. Cross-section of (a) a standard SMF and (b) a ORMOCER® coated SMF. 101

List of Tables

Table 4-1 Parameters in the Sellmeier model for Corning 7980 fused silica, valid in the temperature range from 30 K to 300 K and the wavelength range from 0.4 μm to 2.3 μm [92]. 52

Table A-1. Thermal and mechanical information of the standard and ORMOCER® coated SMF. 101

Chapter 1

Introduction

Optical fibre is a very thin piece of glass that can guide light inside based on the total internal reflection. In 1966, Charles Kao envisioned that it is possible to fabricate an optical waveguide with substantially lower attenuation [1]. Since then, the optical fibre has been under intensive investigations and being applied to different fields. Besides its ultra-low loss, the optical fibre demonstrates other advantages, such as large bandwidth, immunity to electromagnetic (EM) interference, low cost, small size and light weight. As a result, it becomes the foundation of current telecommunication systems and Charles Kao was jointly awarded the 2009 Nobel Prize in Physics for "*ground-breaking achievements concerning the transmission of light in fibers for optical communication*".

All the intrinsic advantages also make the optical fibre an ideal medium for sensing, especially in harsh environments. The optical fibre sensor can be seen as an optoelectronic system that exploits the optical fibre to transmit signal (extrinsic sensor) or measure physical, chemical, biological or other quantities (intrinsic sensor) by detecting the variations of optical properties, such as intensity, frequency, polarisation and phase. The fibre sensor has attracted researchers' interests since its first advert in 1960s [2]. The fibre sensing technique grows fast and gets commercialised due to the low price of the involved optoelectronic components thanks to the significant development in the field of the fibre communications [3]. Nowadays, fibre sensors are being widely used in the fields of civil engineering, energy industry, military surveillance, among others.

Fibre optic sensors can be loosely classified between point sensors and distributed fibre sensors.

The point sensors, such as fibre Bragg gratings (FBG), measure the environmental variations only at its precise location. Most of the point sensors are based on the interference, thus they demonstrate high sensitivities. And many sensors can be multiplexed to acquire the interested parameter over a certain range, but this will increase the system complexity and cost.

For distributed sensors, the whole fibre acts as a continuous sensing medium, thus a single distributed fibre sensor (DFS) is equivalent to a large quantity of point sensors connected together, substantially reducing the cost. Because of this advantage, the annual market reached about $ 550 million in 2010, much larger than the market of point sensors [4]. Distributed sensing is usually realised by techniques such as optical time domain reflectometry (OTDR) or optical frequency-domain reflectometry (OFDR). Time domain measurements provide a metre or sub-metre spatial resolution over several tens of kilometre sensing range; while the spatial resolution of the frequency-domain methods is in the millimetre or sub-millimetre range but their sensing distance is usually limited within several kilometres. Recently, distributed sensing could also be realised in correlation-domain [5]. Generally, this method offers intermediate spatial resolution and sensing distance between the techniques of OTDR and OFDR.

Currently, most of the DFS are based on the various natural scattering processes in the fibre, i.e. Rayleigh, Brillouin and Raman scatterings. Traditional OTDR techniques based on the Rayleigh scattering are able to measure the fibre attenuation and monitor the fibre links in communication networks. Raman scattering based fibre sensors are widely used to measure the temperature distribution along an optical fibre, and its typical sensing distance range is 10 km. The sensors based on Brillouin scattering have the ability to retrieve the temperature and strain profile over a range exceeding 100 km. In the 1990s, a novel OTDR scheme using a coherent light source was proposed [6], which is called phase-sensitive OTDR (ϕOTDR) or coherent OTDR (COTDR) because this system utilises the coherence properties of light. The sensing system is based on the phase interference of the Rayleigh scattered light and is widely used in vibration and intrusion detection [7].

All the distributed fibre sensors mentioned above have been commercialised and are being intensively employed in different fields. The application area of the distributed fibre sensing therefore keeps expanding due to the advantages of the optical fibre. Meanwhile, higher standard requirements stimulate the development of fibre sensing. For example, different sensing techniques have been proposed to enhance the sensing distance over 100 km, improve the spatial resolution down to micrometre scale and increase the number of resolved sensing points beyond 2 000 000 [8-10]. In addition, the already existing techniques are modified for new applications. The COTDR sensor was applied to measure temperature and strain distribution in 2006 [11] and achieved a much higher measurand resolution than the DFS based on Brillouin and Raman scatterings.

In this dissertation, a thorough investigation of the COTDR sensing system is carried out to essentially determine its full operational characteristics, widely ignored of at the beginning of this work. A part of this thesis is dedicated to theoretically and experimentally analyse the received signal in time and frequency domain in order to determine the minimum photodetector bandwidth in a COTDR sensor. Another part focuses on analysing the sensing performance of this system and expanding its application field.

The content of this thesis is specified hereafter:

Chapter 2 presents different optical effects inside the fibre that are of importance for an OTDR system. The spontaneous light scattering processes inside the fibre, i.e. Rayleigh, Brillouin and Raman scatterings, are theoretically described. Then some fundamental concepts of distributed fibre sensing are introduced and the working principles of the OTDR sensors based on different scattering processes are explained. In the last section, several common nonlinear optical effects in the fibre, such as Kerr effect, stimulated Brillouin scattering and stimulated Raman scattering, are introduced and their impact on the sensing performance of different OTDR systems is presented.

In Chapter 3, the scattering process in a COTDR system is explained using the random walk theory and a theoretical model is built to simulate the temporal trace obtained in this system. Then, the statistical property of the signal acquired by coherent detection and direct detection is analysed. The spectrum of the signal is investigated with different incident pulse shapes and the minimum detection bandwidth is determined with the help of the proposed model. Finally, pre-amplification and Brillouin amplification methods are studied to improve the sensing distance of a COTDR sensor.

Chapter 4 is devoted to characterising the thermal response of a COTDR sensor. By modelling the optical fibre as a weak FBG, the temperature sensitivity is obtained at room temperature and cryogenic environments based on the FBG sensing theory. A standard single mode fibre (SMF) coated with acrylate and a fibre with ORMOCER® coating are tested simultaneously in a COTDR sensor with a precise optical frequency control. The experimental results demonstrate a high temperature resolution in the order of mK, although the resolution

becomes worse at 77 K due to the reduced sensitivity under cryogenic conditions. In order to enhance the sensing performance at cryogenic environment, two thermal models are established for electrical and optical heating that can increase the fibre temperature. The model on electrical heating is experimentally validated by a Brillouin sensor under room condition.

In Chapter 5, the COTDR technique is applied to measure the phase birefringence profile along polarisation-maintaining (PM) fibres and standard SMFs. A minimum measurable birefringence of the order of 10^{-7} is obtained due to the high accuracy of the COTDR technique. And a novel DFS is proposed based on this birefringence measurement because temperature and strain will change the local birefringence. In addition, the cross-sensitivity between temperature and strain, a common problem in most DFSs, is worked out by using the combination of the birefringence measurement and the COTDR sensing technique.

In Chapter 6, conclusions are drawn on the main achievements in this thesis and a few perspectives on the COTDR sensing are presented.

Chapter 2

Fundamentals of Optical Time Domain Reflectometry

The OTDR is a very important technique that has been widely used in optical communication and fibre sensing since its first demonstration in 1976 by Barnoski and Jensen [12]. This method is based on light scattering inside the fibre. While light propagates through a medium, several scattering processes will occur based on different light-matter interactions, thus the incident light is deflected into all directions in a bulk inhomogeneous material [13]. However, only forward and backward directions are considered in the optical fibre because the diameter of the cross-section is usually negligible compared with the fibre length.

In an OTDR system, an intense optical pulse is launched into an optical fibre and the optical power of the backscattered light is measured as a function of time. The term OTDR usually refers to the technique based on Rayleigh scattering, which is able to measure the fibre attenuation distribution and locate the fault. With a polarisation analyser at the detection part, the traditional OTDR becomes polarisation-OTDR (POTDR) that measures the state of polarisation (SOP) of the backscattered light [14]. In addition, there is another OTDR technique, so called ϕOTDR or COTDR, that is based on the interference of Rayleigh backscattered light within the pulse width as mentioned in Chapter 1 [15]. The acronym COTDR is used in this thesis to highlight this technique is based on coherent interference of the Rayleigh backscattered light. The OTDR technique can also be realised by measuring Raman or Brillouin backscattered light, named Raman OTDR [16] and Brillouin OTDR (BOTDR) [17], respectively. All of the techniques mentioned above have been commercialised for distributed sensing.

In this chapter, the fundamentals and applications of different OTDR techniques are discussed, the related optical phenomena inside the fibre are introduced and their impacts on the OTDR systems are presented. Firstly, light propagation in a medium is generally described and two features of light, polarisation and coherence, are presented in section 2.1. Then all the spontaneous light scatterings inside an optical fibre are introduced in section 2.2. In the following section, the working principles of different kinds of OTDR techniques are explained and their applications in distributed sensing are discussed. Finally, several nonlinear optical effects are introduced and their influence on the sensing performance of different OTDR systems is discussed in section 2.4.

2.1 Light propagation and some properties

In an OTDR system, an optical pulse passes through the optical fibre and the backscattered light due to different scattering processes is detected. Thus understanding the propagation of light in the medium is very important to

analyse the working principle of any OTDR system. In addition, the coherence and the polarisation of light are introduced because they have the impact on the OTDR performance.

2.1.1 Perturbed wave equation

Light as an electromagnetic field is governed by the well-known Maxwell's equations [18]. The propagation of the lightwave in a medium can be described by the perturbed wave equation derived from Maxwell's equations as [19]:

$$\nabla^2\mathbf{E} - \frac{1}{c^2}\frac{\partial^2\mathbf{E}}{\partial t^2} = \mu_0\frac{\partial^2\mathbf{Pol.}}{\partial t^2}, \tag{2-1}$$

where $c \approx 3\times10^8$ m/s is the light speed in vacuum, **E** is the electric field of the light, **Pol.** is the polarisation field induced by the electrical dipoles in the medium, t represents time, $\mu_0 = 1/\varepsilon_0 c^2$ is the magnetic permittivity in vacuum and ε_0 is the dielectric permittivity in vacuum. In the linear regime, the polarisation **Pol.** is proportional to the electric field **E**: $\mathbf{Pol} = \varepsilon_0\chi\mathbf{E}$, where χ is the linear dielectric susceptibility.

In an isotropic and homogenous medium, the tensor χ reduces to a scalar so that the polarisation depends linearly on the electric field: $\mathbf{Pol.}_L = \varepsilon_0\chi\mathbf{E}$ [19]. Thus Eq. 2-1 can be rewritten as:

$$\nabla^2\mathbf{E} - \frac{n^2}{c^2}\frac{\partial^2\mathbf{E}}{\partial t^2} = 0, \tag{2-2}$$

with the refractive index $n = (\varepsilon/\varepsilon_0)^{1/2} = (1+\chi)^{1/2}$ and ε is the dielectric constant of the medium. But the medium is neither isotropic nor homogeneous in reality. Thus the additional polarisation field $\mathbf{Pol.}_N$ introduced by the dielectric susceptibility variation $\Delta\chi$ should be considered and the expression of polarisation becomes [19]

$$\mathbf{Pol.} = \mathbf{Pol.}_L + \mathbf{Pol.}_N = \varepsilon_0\chi\mathbf{E} + \Delta\boldsymbol{\varepsilon}\mathbf{E}, \tag{2-3}$$

where $\Delta\boldsymbol{\varepsilon} = \varepsilon_0\Delta\chi$ is the dielectric fluctuation. Applying Eq. 2-3 to Eq. 2-1, the perturbed equation becomes:

$$\nabla^2\mathbf{E} - \frac{n^2}{c^2}\frac{\partial^2\mathbf{E}}{\partial t^2} = \mu_0\frac{\partial^2\mathbf{Pol.}_N}{\partial t^2}. \tag{2-4}$$

The right-hand side of the equation accounts for the birefringence, mode coupling, nonlinear effects, etc., but only the scattering processes are considered in this chapter.

The tensor $\Delta\boldsymbol{\varepsilon}$ in Eq. 2-3 represents the medium fluctuations that cause different kinds of light scatterings and it is the sum of two parts: a scalar contribution $\Delta\varepsilon\cdot\delta_{ik}$ and a tensor contribution $\Delta\varepsilon_{ik}^{(t)}$. The scalar contribution is induced by the thermodynamic fluctuations inside the material such as pressure, temperature and entropy changes, which account for Brillouin and Rayleigh scattering [19]. On the other hand, the tensor contribution can be further decomposed into the symmetric part $\Delta\varepsilon_{ik}^{(s)}$ and antisymmetric part $\Delta\varepsilon_{ik}^{(a)}$. The symmetric part is induced by the fast reorientation of molecules and leads to Rayleigh-wing scattering. The anti-symmetric part is due to the molecular vibrations in the presence of the electric field and gives rise to Raman scattering [19].

2.1.2 Coherence of light

Coherence is one of the most important properties of light and is of great importance in a COTDR system. A perfectly monochromatic light is considered as coherent because the phases at different locations or different

times have a fixed relationship. In reality, all lasers demonstrate a certain linewidth, so that the light in practice is partially coherent.

The degree of coherence can be quantified by the correlation of the phase at different points in terms of time or distance, corresponding to temporal coherence and spatial coherence, respectively. In the general case, for stationary and nonstationary waves, the coherence is defined as [20]:

$$Coh(z_1,t_1;z_2,t_2)=\frac{R\left[E^*(z_1,t_1)E(z_2,t_2)\right]}{\sqrt{R\left[\left|E(z_1,t_1)\right|^2\right]R\left[\left|E(z_2,t_2)\right|^2\right]}}, \tag{2-5}$$

where (z_1, t_1) and (z_2, t_2) represent two different points in space-time domain and R represents the auto-correlation function. For a stationary wave, Eq. 2-5 can be simplified, so the degree of temporal coherence is expressed as [21]

$$Coh(\tau)=\frac{R\left[E^*(t)E(t+\tau)\right]}{R\left[E(t)E^*(t)\right]}, \tag{2-6}$$

where τ is the delay time.

It is obvious that the temporal coherence equals to 1 when $\tau = 0$. And the coherence usually decreases as the delay time τ increases. The coherent time τ_c is conveniently defined as the delay time that makes the coherence equal to $1/e$. And the coherent length L_c can be expressed based on the coherent time: $L_c = \tau_c \cdot c/n$. The coherence is inversely proportional to the spectral width of a light source, thus a narrower optical spectrum leads to higher coherence.

2.1.3 Polarisation of light

In the quasi-plane wave approximation, the complex amplitude vector of monochromatic light can be decomposed into two orthogonal components in a plane tangential to the propagation direction. The phases and amplitudes of the components are generally different. Polarisation is a vector to describe the evolution of the two components over the course of an optical cycle [22]. Light is linearly polarised if the phase difference between the two components is 0 or an integer multiple of π, and it is circularly polarised when the phase difference is an odd integer multiple of π/2 and the amplitudes of the components are the same [23]. Otherwise, the light is elliptically polarised.

In an ideal fibre with perfect circular cross-section, the linearly polarised light oscillating in the orthogonal directions would propagate with the same velocity, as long as the material of the fibre is homogeneous and isotropic. In reality, the cross-section cannot be perfectly geometrically symmetric and the fibre shows anisotropy, leading to birefringence that is the refractive index difference between the principle axes in the optical fibre and expressed as:

$$B = n_x - n_y, \tag{2-7}$$

where n_x, n_y are the refractive indices for the two principle axes. The axis with larger refractive index is usually called *slow axis* because the light travels slowlier along this axis, while the other one is called *fast axis*. The birefringence can also be induced by bending, twisting, and environmental perturbations such as temperature and

strain. Nowadays, the typical birefringence of a SMF is in the scale of 10^{-7} [22] due to the fibre spinning technique and there is no particular axis in such a fibre. As a result, the SOP of the light travelling inside a standard optical fibre will change randomly due to the stochastic orientation of the principle axes and the extrinsic perturbations, as shown in Fig. 2-1.

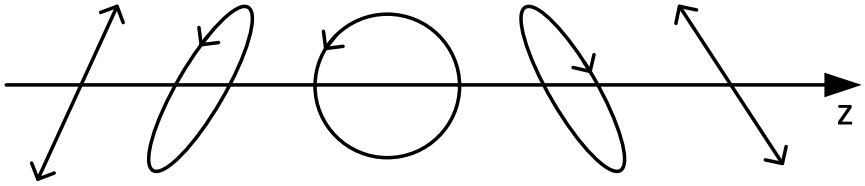

Figure 2-1. State of polarisation changes randomly in the standard fibre.

The existence of birefringence leads to a velocity difference between the orthogonally polarised light waves. In this case, the optical pulse would be broadened after a transmission over a long distance if it contains both polarisation components. This is called polarisation mode dispersion that causes delay between different polarisations and undermines the performance of optical fibre communication systems [22].

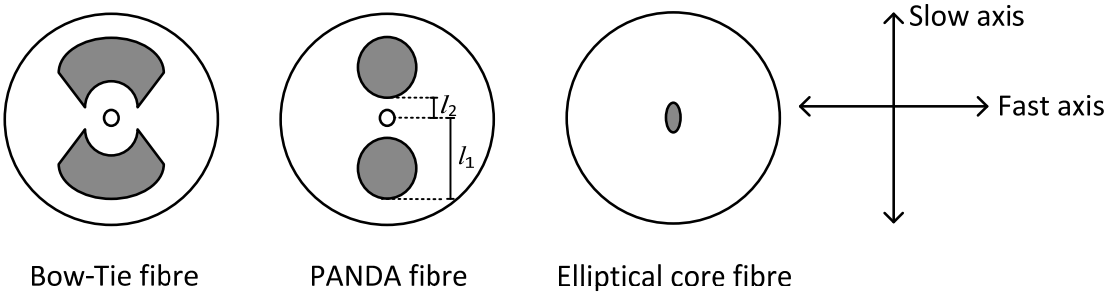

Figure 2-2. Different types of polarisation-maintaining fibres.

Polarisation-maintaining (PM) fibres are proposed to preserve the polarisation of the light. During the fabrication, an asymmetric stress or asymmetric doping is introduced intentionally into the fibre, so that light coupling between the orthogonally polarised modes becomes difficult. Different types of PM fibres have been developed in the last 30 years and the cross-sections of some common ones, Bow-Tie, PANDA and elliptical core fibre, are shown in Fig. 2-2. The PANDA fibre is mainly used in fibre communication and the other types are widely used in the field of fibre sensing [24].

The birefringence of an elliptical core fibre is the sum of the geometric birefringence B_{ge}, expressed as [25]

$$B_{ge} \approx 0.2\frac{2\pi}{\lambda}\left(\frac{l_a}{l_b}-1\right)\left(n_1-n_2\right)^2, \tag{2-8}$$

where l_a and l_b are major and minor core radii of the elliptical core fibre, n_1 and n_2 are refractive indices of the core and cladding, respectively; and of the birefringence B_{so} induced by the core-cladding thermal expansion difference in the asymmetrical core, which can written as [26]:

$$B_{so} = \frac{u^2}{u^2+v^2}\left(1-\frac{l_a}{l_b}\right)B_m \quad with \quad B_m = \frac{\gamma\cdot\Delta T\cdot n_1^3\left(p_{11}-p_{12}\right)}{4\left(1-\sqrt{u^2+v^2}\right)}, \tag{2-9}$$

where $v = |\boldsymbol{k}|(n_1^2 - n^2)^{1/2} \cdot (l_a + l_b)/2$, $u = |\boldsymbol{k}|(n^2 - n_2^2)^{1/2} \cdot (l_a + l_b)/2$, $\boldsymbol{k}$ is the wave vector so that $|\boldsymbol{k}|$ is the corresponding wave number γ is the thermal expansion coefficient of the fibre, ΔT represents difference between the ambient temperature and the softening temperature of the glass, $p_{i,j}$ are strain-optic constants. B_m may be considered as a characteristic constant of glass. .

On the other hand, the birefringence of a PANDA fibre is induced by the stress-applying parts, and can be expressed as [26]

$$B = 4B_m \frac{l_1 - l_2}{l_1 + l_2}\left[1 - \frac{3}{b^4}(l_1 - l_2)^4\right], \tag{2-10}$$

where b is the radius of the cladding, and l_1 and l_2 are the outer and inner radii of the stress-applying parts, respectively.

2.2 Spontaneous light scattering

It is safe to claim that currently all types of scattering processes inside the fibre have been applied to distributed fibre sensing. Hence it is important to understand the light scattering mechanisms in order to investigate the working principles of different DFSs.

In general, light scattering can be categorised as spontaneous and stimulated processes. In the spontaneous case, the material responses are unmodified by the incident light. On the other hand, the optical property of the medium would change if the optical intensity is beyond a certain threshold, leading to stimulated scattering. This section focuses on the spontaneous scattering because it is at the origin of the OTDR technique.

In another way, scatterings can be classified as elastic and inelastic scatterings. In the elastic case, there is no energy exchange between the incident light and the medium. However, the scattered light loses or gains energy compared with the incident light and experiences a frequency shift in inelastic scatterings. The inelastic scatterings can be further classified as “Stokes-type” scattering, in which the incident light frequency is down-shifted; and “anti-Stokes-type” scattering, in which the frequency is up-shifted.

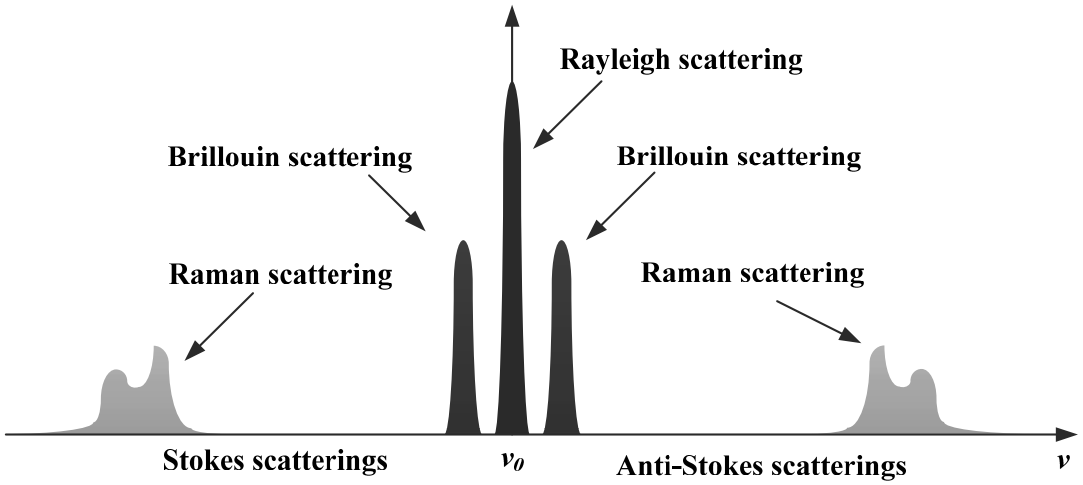

Figure 2-3. Different scattering processes inside the optical fibre.

The spectrum of the scattered light inside the optical fibre is plotted in Fig. 2-3. Rayleigh, Brillouin and Raman scattering processes demonstrate different amplitudes and different frequency shift compared with the incident light frequency v_0. And the inelastic scattering, i.e. Brillouin and Raman scattering, show both Stokes and anti-Stokes components. All the scattering types shown in Fig. 2-3 will be introduced in the rest of this section.

2.2.1 Rayleigh scattering

Rayleigh scattering is caused by the non-propagating fluctuations of medium density and temperature. It can be seen as the radiation of the dipole induced by the applied EM field in the small molecules [27]. As shown in Fig. 2-4, the incident electrical field causes the electrons inside small particles to oscillate, resulting in dipoles that radiate EM field with the same frequency as incident wave into all directions.

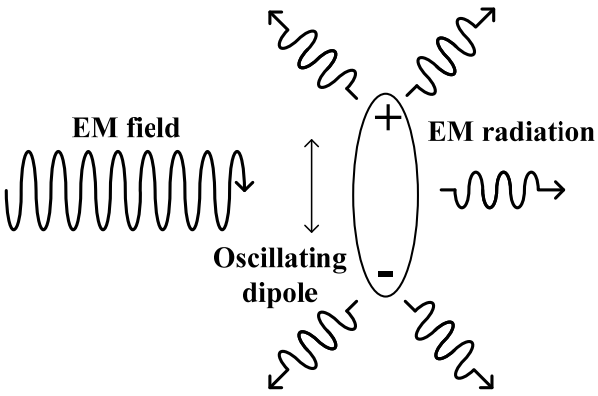

Figure 2-4. Radiation of the oscillating dipole caused by incident electric field.

The diploe moment induced by a monochromatic plane wave traveling in z direction can be written as [28]:

$$\boldsymbol{p} = \hat{\boldsymbol{x}} p_\alpha(\omega) E_0 \cos\left[\omega\left(t - \frac{z}{c}\right)\right], \tag{2-11}$$

where $p_a(\omega)$ is the dipole polarizability and ω represents the angular frequency. And the instantaneous irradiated power is related to the second derivative of dipole moment with respect to time t [28], expressed as:

$$P_{wr} = \left(\frac{1}{4\pi\varepsilon_0}\right)\frac{2}{3c^3}\left(\frac{d^2\boldsymbol{p}}{dt^2}\right)^2 = \frac{\omega^4}{6\pi\varepsilon_0 c^3} p_\alpha^2(\omega) E_0^2 \cos^2\left[\omega\left(t - \frac{z}{c}\right)\right] = \frac{8\pi\omega^4/c^4}{3\left(4\pi\varepsilon_0\right)^2} p_\alpha^2(\omega)\left|\boldsymbol{S}_P\right|, \tag{2-12}$$

where $\boldsymbol{S}_P$ is the Poynting vector. Equations 2-11 and 2-12 show that both the induced dipole and the radiation power oscillate at the same frequency of the applied EM field. Thus Rayleigh scattering is an elastic process in which the scattered light keeps the same optical frequency as the incident light.

Equation 2-12 shows a linear relationship between the total radiated power and the modulus of Poynting vector which represents the power in unit area. Thus the constant of proportionality in Eq. 2-12 has the dimensions of an area [28], which is called scattering cross section and is written as

$$\sigma(\omega) = \frac{8\pi\omega^4}{3\left(4\pi\varepsilon_0 c^2\right)^2} p_\alpha^2(\omega), \tag{2-13}$$

for a single atom according to Eq. 2-12. In the case of a continuous medium that contains M atoms per unit volume, the cross section is expressed as

$$\sigma'(\omega) = \frac{8\pi^3}{3\varepsilon_0^2\lambda^4} p_\alpha^2(\omega) = \frac{8\pi^3}{3\lambda^4 M^2}\left(n^2-1\right)^2, \tag{2-14}$$

where λ represents the wavelength of incident light, and using the dependence of mean polarisability on the atom density M and the refractive index of the medium [28]:

$$p_\alpha = \frac{\varepsilon_0}{M}\left(n^2-1\right). \tag{2-15}$$

It is clear that Rayleigh scattering is stronger at shorter wavelength because Eq. 2-14 shows the dependence of cross section on λ^{-4}.

As explained in Section 2.1.1, Rayleigh scattering has its origin in the dielectric variation $\Delta\varepsilon$ caused by the fluctuations of density ($\Delta\rho$) and temperature (ΔT) [19]:

$$\Delta\varepsilon = \left(\frac{\partial\varepsilon}{\partial\rho}\right)_T \Delta\rho + \left(\frac{\partial\varepsilon}{\partial T}\right)_\rho \Delta T\,. \tag{2-16}$$

For silica fibres, the second term on the right-hand side of Eq. 2-16 can be ignored because it contributes to less than 2% to the change on the dielectric constant [29]. The density fluctuation is determined by the entropy s and pressure p, which are independent thermodynamic variables, and can be expressed as

$$\Delta\rho = \left(\frac{\partial\rho}{\partial p}\right)_s \Delta p + \left(\frac{\partial\rho}{\partial s}\right)_p \Delta s\,. \tag{2-17}$$

The first term on the right hand of Eq. 2-17 represents the adiabatic density fluctuations that causes Brillouin scattering. And the second term is the isobaric density fluctuations induced by the entropy variations, which leads to the Rayleigh scattering inside the optical fibre.

The entropy fluctuation is described by the diffusion equation [19]:

$$\rho c_p \frac{\partial\Delta s}{\partial t} - \kappa\nabla^2\Delta s = 0\,, \tag{2-18}$$

where c_p is the specific heat at constant pressure and κ is the thermal conductivity. The solution to Eq. 2-18 is $\Delta s = \Delta s_0 e^{-\delta t - \boldsymbol{q}\cdot\boldsymbol{r}}$ with the damping rate $\delta = \kappa|\boldsymbol{q}|^2/(\rho\cdot c_p)$ and $\boldsymbol{q}$ is the wave vector of the pressure wave [19]. With the solution of Eq. 2-18, the dielectric constant fluctuation can be obtained based on Eqs. 2-16 and 2-17, so Rayleigh scattering can be described by the perturbed equation expressed as Eq. 2-4 for a given electric field.

2.2.2 Spontaneous Brillouin scattering

Brillouin scattering is based on the propagating pressure of the medium and it can be described as the interaction between photon and acoustic phonon in the view of quantum mechanics. Unlike Rayleigh scattering, Brillouin scattering is an inelastic process in which the incident light is scattered with a frequency shift due to Doppler effect.

As mentioned above, Brillouin scattering is caused by dielectric change arising from the thermodynamic quantity variations. Thus, the equations of the dielectric change used to analyse Rayleigh scattering are also valid to describe spontaneous Brillouin scattering. Inserting Eq. 2-17 into Eq. 2-16, the expression of the density fluctuation becomes

$$\Delta\rho = \left(\frac{\partial\varepsilon}{\partial\rho}\right)_T \left(\frac{\partial\rho}{\partial p}\right)_s \Delta p + \left(\frac{\partial\varepsilon}{\partial\rho}\right)_T \left(\frac{\partial\rho}{\partial s}\right)_p \Delta s \,. \tag{2-19}$$

As mentioned in the previous section, the first term on the right-hand side of Eq. 2-19 represents the dielectric fluctuations at constant entropy and is responsible for Brillouin scattering. But the second term, accounting for Rayleigh scattering, is neglected in this section.

The pressure variation is crucial to describe the Brillouin scattering according to Eq. 2-19 and it is governed by the following equation [19]

$$\frac{\partial^2\Delta p}{\partial t^2} - \Gamma'\nabla^2\frac{\partial\Delta p}{\partial t} - V_a^2\nabla^2\Delta p = 0\,, \tag{2-20}$$

where V_a is the velocity of sound and Γ' is the damping parameter. The acoustic velocity depends on the properties of the material and can be expressed by the thermodynamic variables [19]:

$$V_a = \sqrt{\frac{K}{\rho}} = \sqrt{\frac{1}{C_s\rho}}\,, \tag{2-21}$$

where K is the bulk modulus and C_s is the adiabatic compressibility. The parameter Γ' is written as [19]

$$\Gamma' = \frac{1}{\rho}\left[\frac{4}{3}\eta_s + \eta_b + \frac{\kappa}{C_p}\left(\gamma_r - 1\right)\right] \tag{2-22}$$

with η_s the shear viscosity coefficient, η_b bulk viscosity coefficient, C_p is the compressibility at constant pressure and γ_r the adiabatic index.

The solution to Eq. 2-20 is expressed as [19]:

$$\Delta p = \Delta p_0 \exp\left[i\left(-\boldsymbol{q}\cdot\boldsymbol{r} - \Omega_B t\right)\right] + c.c.\,, \tag{2-23}$$

where $\Omega_B = V_a|\boldsymbol{q}|$ is the frequency of the pressure wave and *c.c.* represents the complex conjugate. Considering a monochromatic incident optical field $\boldsymbol{E}_0(z,t) = A_0(z,t)\exp[\mathrm{i}(\boldsymbol{k}\cdot\boldsymbol{r}-\omega t)]$ + c.c., the perturbed wave equation, as shown by Eq. 2-4, is rewritten as [19]:

$$\begin{aligned}\nabla^2 E - \frac{n^2}{c^2}\frac{\partial^2 E}{\partial t^2} = -\frac{\gamma_e C_s}{c^2}\Big\{&\left(\omega-\Omega\right)^2 A_0\Delta p^* \exp\left[i\left(\boldsymbol{k}-\boldsymbol{q}\right)\cdot\boldsymbol{r} - i\left(\omega-\Omega_B\right)t\right] \\ &+\left(\omega+\Omega\right)^2 A_0\Delta p \exp\left[i\left(\boldsymbol{k}+\boldsymbol{q}\right)\cdot\boldsymbol{r} - i\left(\omega+\Omega_B\right)t\right] + c.c.\Big\}\end{aligned}\,, \tag{2-24}$$

where * denotes the conjugation, A_0, ω and $\boldsymbol{k}$ represent the amplitude, angular frequency and wave vector of the incident light, respectively, and γ_e is the electrostrictive constant. The light-matter interaction gives rise to new frequency components for the Brillouin scattering due to the polarisation of the material. The two terms on the

right-hand side of Eq. 2-24 represent respectively the Stokes part at frequency $\omega - \Omega_B$ and anti-Stokes part at frequency $\omega + \Omega_B$.

During the scattering process, the coupling between the incident wave, the scattered wave and the acoustic wave must obey the dispersion relations [30]:

$$|\boldsymbol{k}| = \omega\frac{n}{c} \quad |\boldsymbol{k}_s| = \omega_s\frac{n}{c} \quad |\boldsymbol{k}_{as}| = \omega_{as}\frac{n}{c} \quad |\boldsymbol{q}| = \frac{\Omega_B}{V_a}, \tag{2-25}$$

where the subscript *s* and *as* denote Stokes and anti-Stokes parts, respectively. Additionally, the momentum conservation must be satisfied for all the involved waves, as shown in Fig. 2-5. As a result, the wave vectors in Brillouin scattering process follow the relation:

$$\boldsymbol{k}_s = \boldsymbol{k} - \boldsymbol{q} \qquad \boldsymbol{k}_{as} = \boldsymbol{k} + \boldsymbol{q} \tag{2-26}$$

for Stokes and anti-Stokes components, respectively.

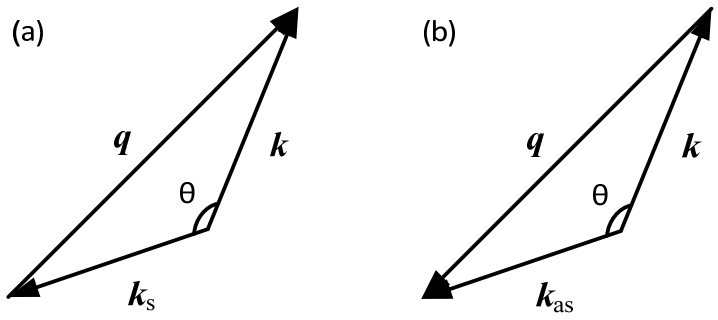

Figure 2-5. Momentum conservation for (a) Stokes and (b) anti-Stokes components of Brillouin scattering.

Since the frequency Ω of the acoustic wave is much smaller than the optical frequency, the wave vector of incident and scattered light are approximately the same: $|\boldsymbol{k}| = |\boldsymbol{k}_s| = |\boldsymbol{k}_{as}|$. As a result, the acoustic wave vector is expressed as $|\boldsymbol{q}| = 2|\boldsymbol{k}|\sin(\theta/2)$ based on the geometric relation shown in Fig. 2-5. With the dispersion relations shown in Eq. 2-25, the frequency of the acoustic wave at scattering angle θ is [19]

$$\Omega_B = 2n\omega\frac{V_a}{c}\sin\left(\frac{\theta}{2}\right). \tag{2-27}$$

According to Eq. 2-27, there is obviously no induced frequency shift for the forward scattering ($\theta = 0$), but the acoustic frequency reaches the maximum at the backward direction ($\theta = \pi$), which is the case in a standard optical fibre.

From the quantum mechanics point of view, Brillouin scattering is the interaction between photons and acoustic phonons. For Stokes process of Brillouin scattering, an incident photon is absorbed and gives rise to an acoustic phonon and a new photon at lower energy. But a photon with higher energy is generated in the anti-Stokes process as the incident photon and an acoustic phonon are annihilated. According to energy conservation, the angular frequencies of the generated photon are expressed as

$$\omega_s = \omega - \Omega_B \qquad \omega_{as} = \omega + \Omega_B, \tag{2-28}$$

for Stokes and anti-Stokes components, respectively. Equation 2-28 shows the scattered light experiences a frequency shift that equals to the acoustic frequency, the same as the result obtained from Eq. 2-24. Thus the Brillouin frequency shift in the fibre is expressed as

$$\nu_B = \frac{\Omega_B(\theta=\pi)}{2\pi} = 2n\frac{V_a}{\lambda}. \tag{2-29}$$

The typical value of Brillouin frequency shift in optical fibre is 10.8 GHz at 1550 nm considering the acoustic velocity in silica V_a = 5900 m/s [31] and the refractive index n = 1.46.

2.2.3 Spontaneous Raman scattering

Raman scattering is a process in which the molecules inside a medium deflect inelastically the incident wave, discovered by C. V. Raman in 1928. Spontaneous Raman scattering is a thermally activated process and is usually explained by the energy level diagrams as shown in Fig. 2-6, for Stokes and anti-Stokes processes, respectively. An incident photon with angular frequency ω could excite a molecule from ground state to the final state at a higher energy level E_1 through a virtual state, shown in Fig 2-6a. The transition of virtual state to excited state produces a new photon with frequency $\omega_s = \omega - \Omega_A$, based on the energy conservation law, where Ω_A is the frequency related to the vibrational mode. On the other hand, the incident photon can absorb the quantum energy from the molecule that is at the higher energy level E_1, as shown in Fig. 2-6b. In this case, the frequency $\omega_{as} = \omega + \Omega_A$ of the emitted photon is higher than that of the incident photon, so this is an anti-Stokes scattering.

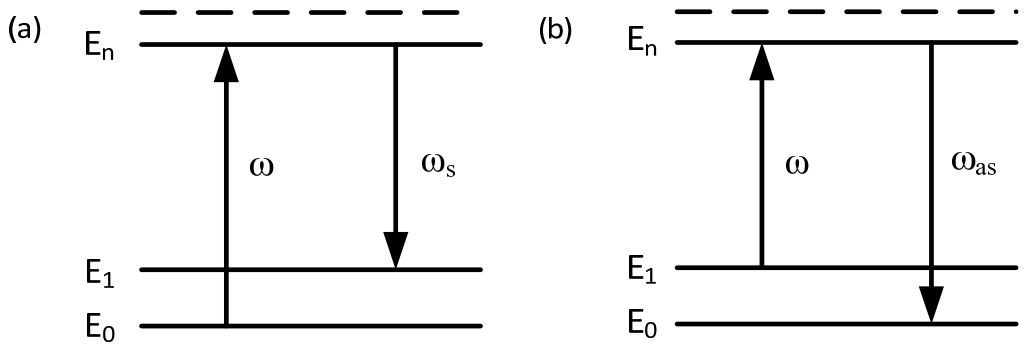

Figure 2-6. Energy level diagrams for Raman (a) Stokes and (b) anti-Stokes scattering.

The strength of spontaneous Raman scattering is dependent on the average number of thermally activated phonons in the material, which is governed by the Bose-Einstein distribution [31]:

$$N_{ave} = 1\Big/\left[\exp\left(h\nu_R \Big/ K_B T\right) - 1\right], \tag{2-30}$$

where h is the Planck constant, K_B is the Boltzmann constant, $\nu_R = \Omega_A/2\pi$ is the Raman frequency shift and T is the absolute temperature in Kelvin.

In the Stokes process, the incident photon is annihilated and gives rise to a phonon so the scattering strength is proportional to $N_{ave} + 1$. However, the scattering efficiency is proportional to N_{ave} in the anti-Stokes process because an incident photon and a phonon are annihilated to create a new photon.

2.3 Optical time domain reflectometry

2.3.1 Working principle of an optical time domain reflectometry

The general setup for a typical OTDR system is shown in Fig. 2-7. The optical pulses from an intensity modulated laser diode are injected into the optical fibre. The backscattered light from the fibre is guided into a photodetector through a circulator or a coupler. Then the received signal is digitalised and processed.

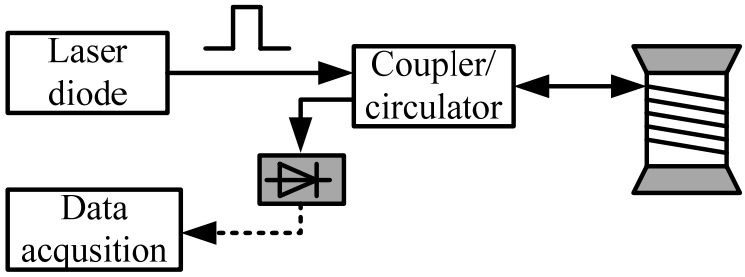

Figure 2-7. Typical OTDR system.

While the optical pulse is traveling along the fibre, light is deflected into all directions at the inhomogeneities in the fibre and most of the Rayleigh scattered light travels out of the fibre core because the scattering angle is too large with respect to the fibre axis. Thus only a small portion of scattered light is recaptured by the fibre and propagates backward. As a result, the optical power of the Rayleigh scattered light at an infinitesimal small region is dependent on the power loss due to Rayleigh scattering at that section and the recaptured factor of the fibre [32]:

$$dP_{RS}(z) = S \cdot P(z)\alpha_{RS}dz\,, \tag{2-31}$$

where the optical power $P(z)$ at position z is expressed as $P(z) = P(0)\cdot\exp(-\alpha z)$ with the input optical peak power $P(0)$ and the total loss coefficient of the fibre α, α_{RS} is the fibre loss due to Rayleigh scattering and the recapture factor S is expressed as [32]

$$S = \frac{3/2}{(W_0/a)^2 V^2}\frac{(\text{N.A.})^2}{n_1^2} = \frac{3}{8\pi^2 n_1^2}\left(\frac{\lambda}{W_0}\right)^2, \tag{2-32}$$

where W_0 is the spot size of the light beam, a is the radius of the fibre core, $V = 2\pi a\text{N.A.}/\lambda$ is the normalised frequency of the fibre, $\text{N.A.} = (n_1^2 - n_2^2)^{1/2}$ is the numeric aperture, n_1 and n_2 are the refractive indices of the core and the cladding, respectively.

Based on Eq. 2-31, the received optical power of the light backscattered at position z in a traditional OTDR system with spatial resolution Δw, which will be explained later, can be derived as:

$$P_{RS}(z) = \Delta w \cdot S \cdot \alpha_{RS}(z) \cdot P(0)\exp\left[-2\int_0^z \alpha(x)dx\right] = \Delta w \cdot R_R \cdot P(0)\exp\left[-2\int_0^z \alpha(x)dx\right], \tag{2-33}$$

where $R_R = S\cdot\alpha_{RS}$ is the equivalent Rayleigh reflection coefficient. It is obvious that the received optical power decays exponentially along the fibre due to the fibre loss, which eventually limits the sensing distance. But

Eq. 2-33 shows that longer optical pulse leads to higher power of the backscattered light thus improves the sensing distance.

As the manufacturing technique develops, the attenuation coefficient α of current optical fibre at 1550 nm could reach 0.2 dB/km ≈ 4.5×10^{-5} m^{-1}. And Rayleigh scattering loss coefficients in different fibres are measured to be very close to 0.2 dB/km at 1550 nm [33], so that α_{RS} is approximately same as α. As a result, the Rayleigh reflection coefficient R_R is calculated to be −72.3 dB/m at 1550 nm for a current standard SMF with a typical recapture factor S = 0.13 % [34].

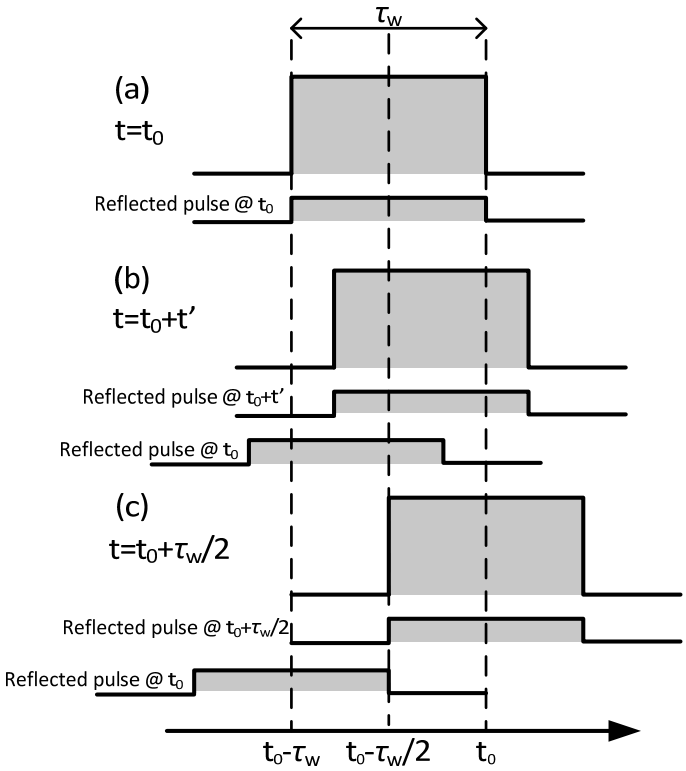

Figure 2-8. Propagation of an optical pulse in the fibre and its Rayleigh scattered light at time (a) t_0, (b) t_0+t' and (c) $t_0+\tau_w/2$.

For all distributed sensors, spatial resolution is an important parameter, which refers to the minimum distinguishable distance between two points along the fibre. The spatial resolution for the OTDR system is explained in Fig. 2-8. An optical pulse with temporal width τ_w is propagating through an optical fibre at a group velocity $v_g = c/n_g$, where n_g is the group refractive index of the fibre. The reflected pulse is excited at every scattering point and propagates backward. Figure 2-8a shows the optical pulse is reflected when its leading edge reaches a location at time $t = t_0$. Then the pulse continues traveling and another RP is exited at time $t = t_0+t'$. But the optical pulse reflected at time t_0 and t_0+t' would overlap if $0<t'<\tau_w/2$ as presented in Fig. 2-8b. The reflected pulse can only be distinguishable when their reflection time difference is larger than $\tau_w/2$, shown in Fig. 2-8c. Thus the spatial resolution is expressed as

$$\Delta w = \frac{\tau_w}{2}\cdot v_g = \frac{\tau_w c}{2n_g}. \tag{2-34}$$

Assuming the group refractive index of the fibre is 1.5, a pulse duration of 10 ns corresponds to a 1 m spatial resolution. Equation 2-34 shows that narrower pulses leads to better spatial resolutions; however, a lower optical

power is received in the case of narrower incident pulses, resulting in short sensing distances for a given detection system according to Eq. 2-33, so there is a trade-off between the sensing distance and spatial resolution for OTDR systems.

Equation 2-33 shows the received optical power decays exponentially as a function of distance. Thus the power in log scale becomes linearly dependent on the distance and the slope represents the fibre attenuation coefficient according to Eq. 2-33. This result is confirmed by a standard OTDR trace of 50 km SMF measured by a commercial equipment (Anritsu MT9083A2), as shown in Fig. 2-9. The slope is measured to be ~ 0.2 dB/km, the same as the standard fibre loss.

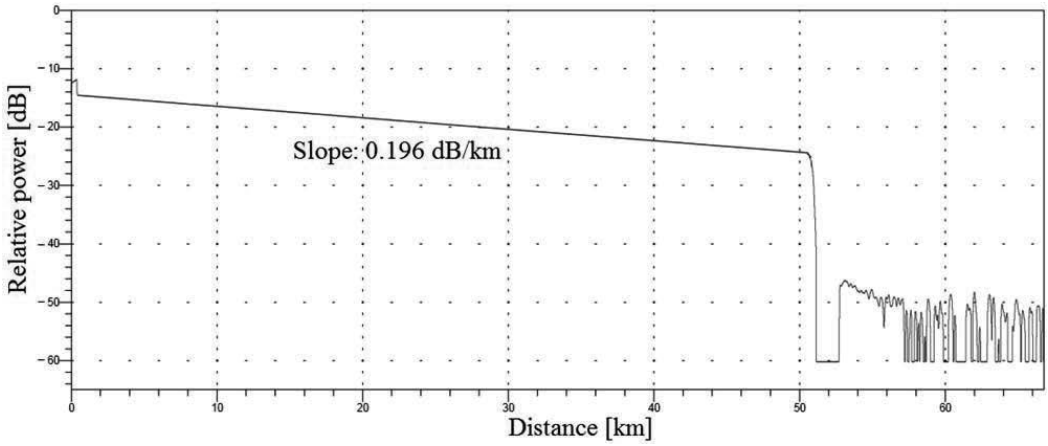

Figure 2-9. An OTDR trace of 50 km fibre measured by Anritsu MT9083A2.

Although the analysis above focuses on the OTDR based on Rayleigh scattering, it can be applied directly to the Brillouin and Raman OTDR systems by replacing R_R with the equivalent Brillouin or Raman coefficient. And the shape in Fig. 2-9 can be seen in all types of OTDR in the ideal case.

2.3.2 Temperature sensing based on the standard OTDR

As presented in Eq. 2-31, the power of the backscattered light in an OTDR system is dependent on the local conditions of the fibre, such as Rayleigh scattering coefficient and the recapture factor. The standard OTDR can be applied for distributed temperature sensing because these parameters may be temperature dependent.

The distributed temperature sensing based on a standard OTDR was first realised in a liquid-core optical fibre [35], in which the scattering coefficient is temperature dependent. A measurand resolution of 1 K is obtained over a 100 m fibre with 1 m resolution. But the liquid core requires strict working conditions to avoid unreliable measurement.

Later, OTDR sensing was realised in solid core fibres with a cladding very sensitive to temperature [36]. The refractive index difference between the core and cladding is subject to the temperature variation, which would change the coupling rate from core into the cladding and lead to a different power of the backscattered light. This method could reach a temperature resolution of ± 5 K.

2.3.3 Polarisation optical time domain reflectometry

As mentioned in Section 2.2.3, the polarisation will change as the light propagating along the standard fibre because of fibre asymmetries originating from the imperfect manufacturing and external perturbations. A

polarisation OTDR is based on monitoring the SOP for the backscattered light by inserting a polarisation analyser in the traditional OTDR system [14]. In a simpler scheme, the polarisation analyser is replaced by a polariser so the SOP change of the backscattered light is converted into optical power variations. The POTDR technique has been widely used in the field of fibre communication to characterise the polarisation property of the fibre such as polarisation mode dispersion and polarisation dependent loss.

Since the polarisation is vulnerable to environmental variations, POTDR has also been applied to distributed sensing. For example, it is widely used in intrusion detection and vibration measurement as the SOP change induced by environmental perturbations leads to a received power variation in the simpler scheme [37]. In addition, POTDR is able to measure the magnetic field because the direction of polarisation for the linearly polarised light rotates in the magnetic field according to the Faraday effect [38, 39].

2.3.4 Coherent optical time domain reflectometry

As science and technology progress, lasers with narrower linewidth have been proposed and applied to the traditional OTDR system. Contrary to common sense, a light source with better coherence leads to a worse OTDR signal, the obtained trace presents a jagged appearance instead of a smooth line as shown in Fig. 2-9 [40]. Later, it is found out that this speckle-like shape is dependent on the phase responses of the backscattered light and cannot be averaged out [41].

At first, the interference of the Rayleigh backscattered light was considered as noise in the OTDR system [42]. Later, researchers realised that this phenomenon originating from the random interference process has a potential for sensing applications. So far, COTDR has been applied to vibration, temperature and strain distributed measurement [15, 43]. Thorough investigation will be presented in the following chapters.

2.3.5 Brillouin optical time domain reflectometry

Brillouin OTDR refers to the traditional OTDR system that measures the Brillouin backscattered light. Equation 2-36 obviously presents the Brillouin coefficient depends on temperature. Actually, it is also strain dependent because the refractive index, fibre density and acoustic velocity are related to strain. Thus the optical power of the Brillouin backscattered light can be used to measure environmental variations. The temperature and strain sensitivities based on the Brillouin power are 0.36 %/K and -8×10^{-4} %/με, respectively [44]. The obtained Brillouin signal needs to be normalised by the Rayleigh scattered light to compensate for the bending or splicing loss. In practice, the intensity ratio between Rayleigh and Brillouin scattered light, known as Landau-Placzek ratio, is measured in BOTDR system to monitor environmental variations [45].

Distributed sensing can also be realised by measuring the Brillouin frequency which is proportional to the speed of the acoustic wave, as presented by Eq. 2-33. Since the acoustic velocity depends on the material density ρ according to Eq. 2-25, which is sensitive to temperature and longitudinal strain, the Brillouin frequency shifts in response to local environmental variations.

To obtain the Brillouin frequency shift, coherent detection is usually used in the BOTDR system. The Brillouin backscattered light is mixed with an optical local oscillator (LO) and their beating is detected by the receiver. By scanning the LO frequency, the Brillouin spectrum is precisely obtained and the Brillouin frequency shift can be determined by a Lorentzian fitting [44]. In this case, the sensitivity is measured to be 1.07 MHz/K and 0.048 MHz/με, respectively for temperature and strain [44]. The spontaneous temperature and strain sensing

can be realised in a BOTDR system combining the measurement of the Brillouin frequency and the corresponding optical power.

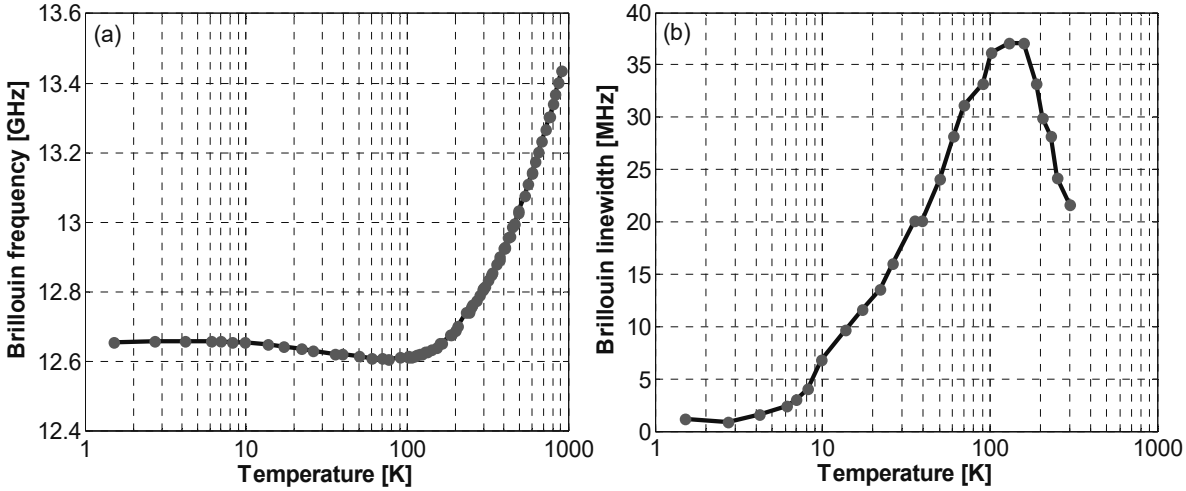

Figure 2-10. Reported result on the temperature dependence of (a) Brillouin frequency shift and (b) Brillouin linewidth of a standard single mode fibre [46].

Although the Brillouin sensor works well at room temperature, the frequency shift, intensity and spectrum width all behave unexpectedly under cryogenic conditions due to the nonlinearities of acoustic velocity and attenuation at low temperature [47]. For example, the Brillouin frequency shift and the gain spectrum width measured in a standard SMF over a wide temperature range from 4.5 K to 1000 K are presented [46] in Fig. 2-10a and 2-10b, respectively. The Brillouin frequency is at around 13 GHz because the measurement is taken at 1319 nm. It clearly shows that neither the frequency shift nor the linewidth is linearly dependent on the fibre temperature at low temperatures. Particularly, the relationship of Brillouin frequency and temperature becomes non-monotonic below 150 K, as shown in Fig. 2-10a. Thus the temperature cannot be determined easily in this range because the Brillouin frequency corresponds to more than one temperature value.

2.3.6 Raman optical time-domain reflectometry

In a Raman OTDR system, the Raman backscattered light is detected by a standard OTDR technique. As stated in Section 2.2.3, the strength of the spontaneous Raman scattering is proportional to the average number of thermally activated phonons, and the optical power of the anti-Stokes component is $P_{AS} \propto N_{ave}$ while for the Stokes component it is $P_S \propto N_{ave}+1$ because of the different resulting number of phonons. According to Eq. 2-30, N_{ave} is related to the fibre temperature and Raman frequency shift. Raman frequency shift is dependent on the material and it is measured to be 13.2 THz in fused silica [48], leading to $N_{ave} \approx 0.14$ under ambient conditions. Thus the Stokes component is about 8 times larger than the anti-Stokes part and it is also less temperature dependent since $N_{ave} << 1$.

The power of the anti-Stokes component in Raman scattering is measured to be quasi-linearly dependent on temperature [16]. In practice, the ratio between optical power of spontaneous anti-Stokes and Stokes/Rayleigh waves is used to retrieve the temperature information in order to compensate extra loss induced by bending or splicing like in the BOTDR technique. For example, the ratio between anti-Stokes and Stokes waves at a given fibre position z is expressed as [49]:

$$\frac{P_{AS}(z)}{P_S(z)} = C_R \exp\left[-(\alpha_{AS} - \alpha_S)z\right] \exp\left(-\frac{h\nu_R}{K_B T}\right), \tag{2-35}$$

where C_R is a constant related to the receiver response, α_{AS} and α_S are the fibre attenuation coefficients for the anti-Stokes and Stokes components.

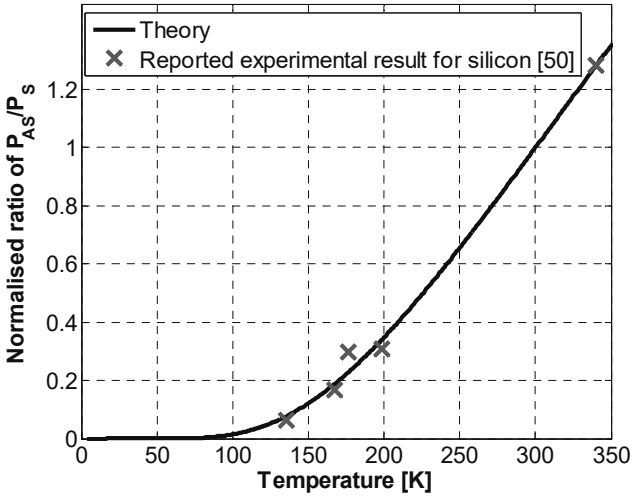

Figure 2-11. Normalised ratio of anti-Stokes and Stokes waves as a function of the fibre temperature.

For the Raman sensor, there is no cross sensitivity between the temperature and strain because the Raman scattered light depends only on temperature, which is an advantage compared with other OTDR sensors. However, spontaneous Raman scattering is essentially a thermal activated process so the scattered light becomes weak at low temperature, especially for the anti-Stokes component. This trend would definitely undermine the sensing performance of the Raman sensor at cryogenic condition. The result is plotted as a function of temperature in Fig. 2-11. Although the ratio changes linearly at room temperature, it becomes a quasi-parabolic function for temperatures from 200 K to 100 K and starts to vanish quickly below 100 K. This trend is confirmed by the reported results in silicon [50]. The optical power ratio between anti-Stokes and Stokes waves is normalised to its value at 300 K to make the comparison easier. The weak Raman scattering at cryogenic temperature leads to low signal-to-noise ratio (SNR) of the measurement and results in a degraded temperature resolution.

2.4 Nonlinear processes in the fibre

If the intensity of the light is above a certain threshold, the optical properties of a material will change due to the presence of an intense light. As a result, the polarisation becomes a nonlinear function of the electric field [51]:

$$Pol. = \varepsilon_0 \left(\chi^{(1)}.E + \chi^{(2)} : EE + \chi^{(3)} \vdots EEE + \cdots\right), \tag{2-36}$$

where $\chi^{(i)}$ is the ith-rank tensor of susceptibility. The first rank of susceptibility is related to the linear part of the polarisation and corresponds to the refractive index and the linear absorption of the material. And the third-rank term dominates the nonlinear part of the polarisation for standard optical fibres because the second-rank susceptibility is zero due to the centro symmetrical character of silica [51]. The contribution of higher-rank terms is negligible. The third-rank susceptibility accounts for the stimulated scatterings and Kerr effect.

In this section, several nonlinear effects that have impacts on the performance of different OTDR systems are presented. Generally speaking, the OTDR sensing distance is limited because the peak power of the optical pulse should be under a certain threshold to avoid nonlinear effects. But some nonlinearities can provide in-line amplification to increase the sensing distance and can even be applied directly for distributed sensing.

2.4.1 Self-phase modulation

While an intense optical pulse is traveling along the fibre, the refractive index would be changed by the product of the light intensity and the nonlinear part of the refractive index n_n which is related to the third order susceptibility tensor. This index variation induces phase shift to the optical pulse and leads to a spectrum change of the incident light.

Self-phase modulation will shift the optical frequency of the incident pulse by [52]

$$\delta\nu = -\frac{n_n z}{\lambda_0}\frac{\partial \delta n}{\partial t} = -\frac{n_n z}{A_{eff}\lambda_0}\frac{\partial P(t)}{\partial t}, \tag{2-37}$$

where A_{eff} is the effective cross section area, z is the propagation length of the optical pulse and P(t) is the power of the optical pulse in time domain. This frequency shift would cause trouble for the OTDR system with coherent detection because the frequency difference between the Rayleigh backscattered light and the LO should be very stable. In addition, self-phase modulation would induce spectral broadening of the optical pulse, which will broaden the Brillouin gain spectrum, leading to the measurement error in the Brillouin sensing [53].

2.4.2 Modulation instability

Modulation instability (MI) is a widely observed phenomenon in the fields of nonlinear optics and fluid dynamics. In optics, it is the result of the interplay between the Kerr effect and dispersive effect, leading to the breakup of a continuous wave beam into a train of ultrashort pulses in time domain. And MI manifests itself in frequency domain by two gain sidelobes located symmetrically with respect to the incident light wavelength. During light propagation, the optical power would be exchanged quasi-periodically between the incident light and the generated sidelobes [51].

The detrimental effects of MI have been observed in many sensing systems. In a BOTDR system, the generated sidelobes contaminate the Brillouin spectrum and lead to a measurement error [54]. In addition, these sidebands broaden the incident light spectrum, degrading the coherence of the optical pulse. As a result, the interference fading occurs in a COTDR system [55].

2.4.3 Four-wave mixing

Four-wave mixing (FWM) is an interaction among at least two light beams with different frequencies propagating in a nonlinear medium, which will create new frequency components through the third order nonlinear polarisation. FWM originates from the nonlinear response of bound electrons in a material to the applied EM field [51]. The beating of incident lightwaves modulates the refractive index of the medium which creates waves at different frequencies. Actually, it is another sequence of Kerr effect, just like MI.

To maximise the efficiency of FWM, a phase-matching condition must be satisfied, which depends on chromatic dispersion. Thus FWM has been applied to map chromatic dispersion along the fibre with the help of a Brillouin based sensor to probe the optical power of the generated wave [56].

2.4.4 Stimulated Brillouin scattering

Stimulated Brillouin scattering (SBS) in optical fibres is based on electrostriction, which is the tendency of materials to compress in the presence of electric field. The induced electrostatic pressure would cause density variations in the material, generating an acoustic wave which deflects the incident light.

There are three waves interacting in the optical fibre for the SBS process: a strong pump E_p (incident light), a counter-propagating weak probe $E_{pro.}$ (incident or scattered light at Stokes frequency shift) and the acoustic wave. The interference of pump and probe light creates an optical intensity wave oscillating at the frequency difference between the pump and probe waves. And the intensity wave introduces electrostriction, leading to a density change of the material. The density change causes refractive index variations so that the propagating density wave works as a moving fibre Bragg grating (FBG) resonating at the pump frequency. The frequency of the light scattered by the moving grating is down-shifted compared to the incident light frequency due to the Doppler effect. The scattered light adds constructively to the probe light and the amplified probe would enhance the acoustic wave.

The pump and probe waves counter-propagating in the optical fibre are defined as

$$\begin{aligned} \boldsymbol{E}_p &= \boldsymbol{e}_p A_p(z,t)\exp\left[i\left(k_p z-\omega_p t\right)\right]+c.c. \\ \boldsymbol{E}_{pro.} &= \boldsymbol{e}_{pro.} A_{pro.}(z,t)\exp\left[i\left(-k_{pro.} z-\omega_{pro.} t\right)\right]+c.c. \end{aligned}, \tag{2-38}$$

where $\boldsymbol{e}_p$ and $\boldsymbol{e}_{pro.}$ represent unit polarisation vectors for pump and signal waves, A_p and $A_{pro.}$ are respectively the corresponding complex envelops of pump and probe light. The nonlinear polarisation for the pump and probe are expressed as [19]:

$$P_{p,pro.}^{NL} = \varepsilon_0 \Delta\varepsilon E_{p,pro.}(z,t) = \varepsilon_0 \frac{\gamma_e}{\rho_0}\Delta\rho(z,t) E_{p,pro.}(z,t), \tag{2-39}$$

with the density variation $\Delta\rho$ related to the acoustic wave [19]:

$$\Delta\rho(z,t) = Q_a(z,t)\exp\left[i\left(qz-\Omega t\right)\right]+c.c., \tag{2-40}$$

where Q_a(z,t) and $\Omega = \omega_p - \omega_{pro.}$ are respectively the slowly-varying envelope and angular frequency of the acoustic wave. The density variation obeys the following equation [19]:

$$\frac{\partial^2\Delta\rho}{\partial t^2} - \Gamma'\nabla^2\frac{\partial\Delta\rho}{\partial t} - V_a^2\nabla^2\Delta\rho = -\nabla.F_e \tag{2-41}$$

with Γ' the damping parameter and F_e. the electrostrictive force In the presence of pump and probe light, the term on the right-hand side of Eq. 2-41 can be expressed as [19]

$$\nabla.F = \eta\gamma_e q^2 A_p(z,t) A_{pro.}^*(z,t)\exp\left[i\left(qz-\Omega t\right)\right]+c.c., \tag{2-42}$$

where $\eta = |\boldsymbol{e}_p \cdot \boldsymbol{e}_{pro.}|$ is the polarisation mixing efficiency. Equations 2-38, 2-39 and 2-41 connect pump, probe and acoustic waves together.

The pump and probe waves are governed by the perturbed equation with the nonlinear polarisation shown as Eq. 2-39 and the acoustic wave can be obtained by Eqs. 2-40, 2-41 and 2-42. Using the slow varying envelope approximation, the second space and time derivatives of the wave amplitudes are neglected. Hence the three-wave coupling process is presented as [19]

$$\begin{aligned}
&\frac{\partial A_p(z,t)}{\partial z}+\frac{n}{c}\frac{\partial A_p(z,t)}{\partial z}=\frac{i\omega_p\gamma_e}{2nc\rho_0}A_{pro.}(z,t)Q_a(z,t)\\
&-\frac{\partial A_{pro.}(z,t)}{\partial z}+\frac{n}{c}\frac{\partial A_{pro.}(z,t)}{\partial z}=\frac{i\omega_{sig.}\gamma_e}{2nc\rho_0}A_{p.}(z,t)Q_a^*(z,t)\\
&-2iqV_a^2\frac{\partial Q_a(z,t)}{\partial z}-2i\Omega\frac{\partial Q_a(z,t)}{\partial t}+\Gamma_A Q_a(z,t)=\varepsilon_0\gamma_e q^2 A_p(z,t)E_{pro.}^*(z,t)
\end{aligned}, \tag{2-43}$$

with $\Gamma_A=\Omega_B{}^2-\Omega^2-i\Omega\Gamma_B$ the detuning factor. The coupled equations in Eq. 2-43 fully describe the interaction of pump, probe and acoustic waves inside the optical fibre. Since there is no analytic solution to the coupled equation, numerical method or some approximation, e.g. small gain, can be used to make Eq. 2-40 solvable.

Stimulated Brillouin scattering can be applied directly to distributed fibre sensing and different sensing schemes have been proposed to achieve long sensing distance or higher spatial resolution [57]. The above analysis shows that the optical power of intense pump light would transfer to the counter-propagating weak light through the SBS process if their frequency difference is close to the Brillouin frequency. Thus SBS can be employed as an amplifier and it has been applied to the COTDR system and Brillouin sensor to increase the sensing distance [58, 59].

2.4.5 Stimulated Raman scattering

If the incident light is over a certain threshold, it would periodically modulate the material susceptibility with the vibrational mode of the molecule for Raman scattering [31]. Thus the spontaneous process becomes stimulated and a lot of optical power is transferred from the incident light to the Stokes component. And this process is governed by the following coupled wave equation [51]:

$$\begin{aligned}
\frac{dI_s}{dz}&=g_R I_p I_s-\alpha_s I_s\\
\frac{dI_p}{dz}&=-\frac{\omega_p}{\omega_s}g_R I_p I_s-\alpha_p I_p
\end{aligned}, \tag{2-44}$$

where I, ω and α represent optical intensity, angular frequency and fibre loss for pump p and Stokes components s, respectively, and g_R is the Raman gain coefficient.

Stimulated Raman scattering has been applied to in-line amplification in fibre communication [60]. In addition, different schemes of Raman amplifier have been proposed to improve the sensing distance of DFS based on Rayleigh and Brillouin scattering [61, 62].

Chapter 3

Properties of Coherent Optical Time Domain Reflectometry

In a traditional OTDR system, an incoherent light source is used and the obtained signal is a smooth trace as presented in the previous chapter. When lasers with narrower linewidth are employed, whose coherent length is longer than the pulse width, the detected trace gets more "noisy" [42] because some backscattered light will sum up coherently. In a COTDR system, the coherent length of the light source is longer than the optical pulse width, so that there is only interference among the light backscattered from different inhomogeneities inside the optical pulse. The obtained trace demonstrates a stochastically varying amplitude, as shown in Fig. 3-1, due to the random variation of refractive index along the fibre.

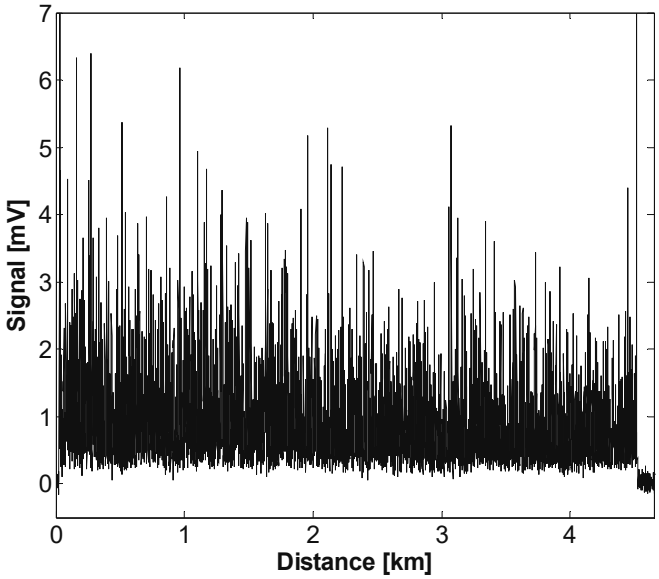

Figure 3-1. Typical coherent Rayleigh trace.

The jagged shape shown in Fig. 3-1 carries meaningful information about the local refractive index, which is dependent on the environmental conditions. Hence coherent Rayleigh scattering becomes a powerful technique in the fields of fibre sensing due to this interference process [43]. It is important to understand this process and the characteristics of the obtained Rayleigh signal to make use of it.

In this chapter, the temporal and spectral characteristics of coherent Rayleigh trace are investigated. Firstly, the coherent Rayleigh trace is found to be essentially a random walk process and is simulated by a 1-D model in

section 3.2. The theoretical analysis and simulation result show that the shape of the COTDR trace is dependent on the refractive index and the optical frequency.

Based on the mature theory of random walk, the statistical property of Rayleigh backscattered light is analysed, revealing that its amplitude and intensity obey Rayleigh and exponential decay distributions, respectively. The simulation result turns out to be the same as the theoretical analysis and is confirmed by the experiment in section 3.3.

Then the spectral features of the coherent Rayleigh trace are investigated in section 3.4 and its power spectrum density (PSD) shows a dependence on the incident optical pulse shape. The theoretical result is experimentally validated for rectangular and sinc incident optical pulses. And the optimal bandwidth of the photodetector in a COTDR system is determined according to the frequency spectrum of the coherent Rayleigh trace and its temporal features, i.e. statistic distribution and visibility of the traces obtained at different bandwidth.

In the last section of this chapter, the sensing range of a COTDR system is improved by pre-amplification and Brillouin amplification, and their performances are compared.

3.1 Theoretical model for coherent Rayleigh scattering

A COTDR system is almost the same as a standard OTDR, such as the one shown in Fig. 2-7, with the difference that the coherent length of the light source must be longer than the pulse width. In this case, the electric fields of the backscattered light inside the optical pulse will superpose together. As a result, the detected signal demonstrates stochastic varying amplitude due to the random distribution of refractive index along the fibre, as shown in Fig. 3-1.

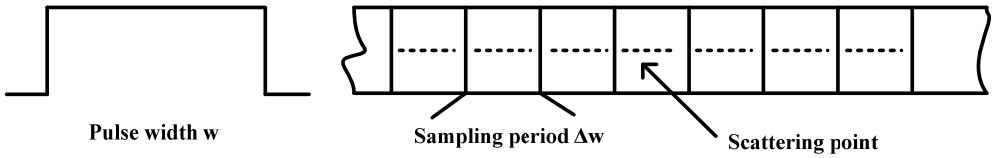

Figure 3-2. Discrete 1D model for coherent Rayleigh scattering.

The inhomogeneities in the fibre core can actually take any shape, but the optical fibre is modelled as a unidimensional medium consisting of scattering points with uniform size Δz for simplicity, as shown in Fig. 3-2. It is assumed that the input light is linearly polarised and always normally incident on the interface of two scattering points. The refractive index of each point is expressed as $n(z) = n_{ave} + \Delta n(z)$, where n_{ave} is the average index along the fibre and $\Delta n(z)$ is the local index variation due to the fibre density fluctuation. This statistical property of the index variation is governed by the correlation $\langle \Delta n(z)\Delta n(z')\rangle = \sigma_{\Delta n}^2 \exp(-|z-z'|/z_R)$ with the variance $\sigma_{\Delta n}^2 \ll 1$ and the index correlation length $z_R \sim 10$ nm [63]. The index variance is dependent on the optical wavelength, fibre attenuation coefficient and the correlation length [64]:

$$\sigma_{\Delta n}^2 = \frac{3\lambda^4}{2(2\pi)^3 n_{ave}^2 z_R^3}. \tag{3-1}$$

Because the scattering size is considered in the order of the optical wavelength [65], so $|z-z'| \gg z_R$. As a result, the correlation can be approximated as $\langle \Delta n(z)\Delta n(z')\rangle = \sigma_{\Delta n}^2 \delta(z-z')$.

The inhomogeneities will scatter the incident light and induce a phase change. The complex amplitude vector of the light reflected from the scattering point at z is expressed

$$\boldsymbol{E}_s(z) = \boldsymbol{E}_0 \boldsymbol{r}_e(z) e^{-\alpha z + j2\phi(z)}, \tag{3-2}$$

where $\boldsymbol{E}_0$ is the input optical field, α is the fibre loss coefficient, $\boldsymbol{r}_e(z)$ is the complex reflection coefficient and the optical phase ϕ is expressed as:

$$\phi = \int_0^z \beta dx = 2\pi \frac{\nu}{c} \int_0^z n_{eff}(x) dx, \tag{3-3}$$

where β is propagation constant, c is the light speed in vacuum, ν is the optical frequency. It is obvious that the scattered light at z is dependent on the optical frequency ν and the effective refractive index distribution n_{eff} in the range [0, z]. In the 1D model, the refractive index along the fibre has to be replaced by the effective refractive index to simulate the COTDR trace.

The reflection coefficient $\boldsymbol{r}_e(z)$ in Eq. 3-2 is usually modelled as a circular complex Gaussian (CCG) random variable with delta correlation [40]:

$$\left\langle \boldsymbol{r}_e(z) \boldsymbol{r}_e(z') \right\rangle = r_0^2 \delta(z - z'), \tag{3-4}$$

where r_0^2 is the ensemble average of $\boldsymbol{r}_e(z)$ and is dependent on the fibre loss and recapture angle. Thus, the amplitude $|\boldsymbol{E}_s(z)|$ of the backscattered light $\boldsymbol{E}_s(z)$ is statistically independent of $|\boldsymbol{E}_s(z')|$ unless $z = z'$.

The reflected light at each scattering point will interfere within the pulse width w, so that the backscattered signal $\boldsymbol{E}$ at location z is the summation of electrical field of the light backscattered in the range [z, z+w/2]:

$$\boldsymbol{E}(z) = R + j \cdot I = e^{-\alpha z} e^{j2\int_0^z \beta(x)dx} \sum_{m=1}^{M'} P_E(m) \cdot \boldsymbol{E_0} \boldsymbol{r}_e(z + m \cdot \Delta z) e^{j2\int_z^{z+m\cdot\Delta z} \beta(x)dx}, \tag{3-5}$$

where R and I are the real and imaginary part of $\boldsymbol{E}$ respectively, $M' = w/(2\Delta z)$ represents the number of scattering points inside the pulse, $\boldsymbol{E}_0$ is the peak of optical pulse field, P_E is the normalised pulse shape. The typical pulse duration of the COTDR system is in the meter scale so that the fibre loss within the pulse width is neglected.

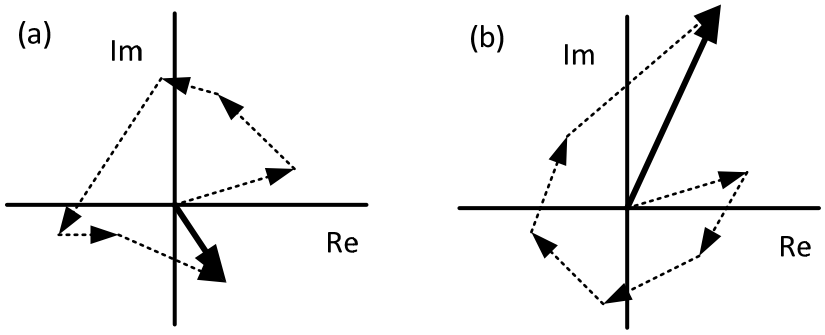

Figure 3-3. Scheme of random process in case of (a) destructive and (b) constructive resultant.

The amplitude of the backscattered light can be simulated by Eq. 3-4 using a randomly generated effective refractive index $\Delta n_{eff}(z)$, while the reflection coefficient can be calculated based on the Fresnel equation. Because the light is assumed to be normally incident on scattering points, the phase change induced by scattering

is either 0 or π, determined by the refractive indices of successive inhomogeneities. However this method is very inefficient and time-consuming because there exist millions of scattering points contributing to the Rayleigh scattering interfering inside the pulse width. In addition, an exhaustive simulation considering each scattering point is unnecessary since the time-domain Rayleigh trace is sampled by the acquisition system at discrete points with a sampling interval Δw, so that each data point contain the interference resulting from the Rayleigh light backscattered from thousands scattering points.

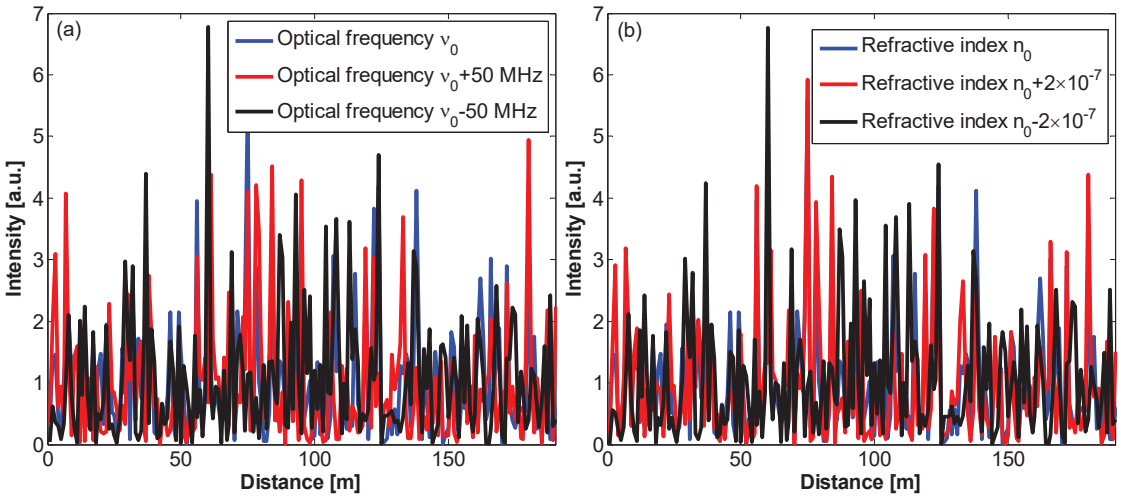

Figure 3-4. The simulated coherent Rayleigh trace shows dependence on (a) optical frequency and (b) refractive index.

As a result, the workload reduces greatly by substituting the index $\Delta n_{eff}(z)$ at each scattering points by an equivalent factor $\Delta n'_{eff}(z)$ at each sampled location z_k. Since the number of scattering points inside the sampling interval is still very large, the index variation is assumed to follow a Gaussian distribution as justified by the central limit theorem [65]. The refractive index variation could also be assumed to follow Gaussian distribution for the same reason. In this way, a coherent Rayleigh trace can be simulated through Eq. 3-4.

Since coherent Rayleigh scattering is essentially an interference process, it should be dependent on optical frequency and the refractive index of the fibre. The simulation takes both parameters into consideration by the optical phase as expressed by Eq. 3-2. And the simulated traces exhibit this dependence, a small change of the optical frequency or the refractive index would result in totally different traces, as shown in Fig. 3-4a and 3-4b, respectively.

3.2 Temporal properties of coherent Rayleigh traces

The spiky appearance of Rayleigh signal originates from the random fluctuation of refractive index along the fibre. The coherent Rayleigh scattering DFS is based on the fact that any environmental perturbation that modifies the index would change the temporal shape, as shown in Fig. 3-4b. On the other hand, the coherent Rayleigh scattering introduces noise to fibre communication [66] and sensors, e.g. gyroscope sensor [67]. In either case, it is very important to analyse the temporal characteristic of coherent Rayleigh trace.

3.2.1 Theory of the statistical properties of COTDR traces

The previous section reveals that coherent Rayleigh scattering is a random walk process, thus the characteristics of the coherent Rayleigh trace can be analysed based on this mature theory. Three assumptions are usually

adopted to investigate the summation of phasors in random walks [68]. And these assumptions are also valid for the coherent Rayleigh scattering:

1. The phase ϕ of reflected light $\boldsymbol{E}_s$ at each scattering point is considered to be uniformly distributed in the range [−π, π] after taken mod of 2π;

2. The amplitude $|\boldsymbol{E}_s(z)|$ and phase $\phi(z)$ of the backscattered light $\boldsymbol{E}_s(z)$ are statistically independent of the corresponding parameters at another position;

3. The amplitude $|\boldsymbol{E}_s(z)|$ and phase $\phi(z)$ are statistically independent of each other.

The statistical property of amplitude in COTDR traces is analysed here, then the intensity distribution can be derived accordingly. From Eq. 3-4, the real and imaginary part of $\boldsymbol{E}$ can be expressed as [69]

$$\begin{aligned} R &= \sum_{m=1}^{M'} \left|\boldsymbol{E}_s(m)\right| \cos(\phi_m) \\ I &= \sum_{m=1}^{M'} \left|\boldsymbol{E}_s(m)\right| \sin(\phi_m) \end{aligned} \tag{3-6}$$

where M' is the number of scattering points within the pulse width and ϕ_m is the phase of the scattered light $\boldsymbol{E}_s(m)$.

As stated above, the optical phase ϕ_m of the scattered light $\boldsymbol{E}_s$ is uniformly distributed in the range [-π, π], leading to the expected value of $\sin\phi_m$ and $\cos\phi_m$ equal to zero. In addition, the amplitude $|\boldsymbol{E}_s(z)|$ and phase $\phi_m(z)$ are assumed statistically independent. Thus the expected value EV of real and imaginary parts is expressed as:

$$\begin{aligned} E(R) &= EV\left(\sum_{m=1}^{M'} \left|\boldsymbol{E}_s(m)\right| \cos(\phi_m)\right) = \sum_{m=1}^{M'} EV\left[\left|\boldsymbol{E}_s(m)\right|\right] E\left[\cos(\phi_m)\right] = 0 \\ E(I) &= EV\left(\sum_{m=1}^{M'} \left|\boldsymbol{E}_s(m)\right| \sin(\phi_m)\right) = \sum_{m=1}^{M'} EV\left[\left|\boldsymbol{E}_s(m)\right|\right] E\left[\sin(\phi_m)\right] = 0 \end{aligned}, \tag{3-7}$$

respectively. The real and imaginary parts of the scattered light can also be proved uncorrelated in the same way:

$$E[RI] = \sum_{m=1}^{M'} EV\left[\left|\boldsymbol{E}_s(m)\right|^2\right] EV\left[\cos(\phi_m)\sin(\phi_m)\right] = \sum_{m=1}^{M'} EV\left[\left|\boldsymbol{E}_s(m)\right|^2\right] EV\left[\frac{1}{2}\sin(2\phi_m)\right] = 0 . \tag{3-8}$$

The statistical independence between amplitude and phase simplifies the expression of the variance of R:

$$\sigma_R^2 = EV\left[R^2\right] = \sum_{m=1}^{M'-1} \sum_{n=m+1}^{M'} EV\left[\left|\boldsymbol{E}_s(m)\right|\left|\boldsymbol{E}_s(n)\right|\right] EV\left[\cos(\phi_m)\cos(\phi_n)\right]. \tag{3-9}$$

According to the assumptions above, the phases of light scattered at different positions are uncorrelated, resulting in $EV[\cos(\phi_m)\cdot\cos(\phi_n)] = EV[\cos(\phi_m)]\cdot EV[\cos(\phi_n)] = 0$. Thus only the condition $m = n$ is considered in Eq. 3-9, leading to [70]:

$$\sigma_R^2 = \sum_{m=0}^{M'} EV\left[\left|\boldsymbol{E}_s(m)\right|^2\right] EV\left[\cos^2(\phi_m)\right] = \frac{1}{2}\sum_{m=1}^{M'} EV\left[\left|\boldsymbol{E}_s(m)\right|^2\right]. \tag{3-10}$$

Likewise, the variance of I is expressed as:

$$\sigma_I^2 = \sum_{m=0}^{M'} EV\left[\left|\boldsymbol{E}_s(m)\right|^2\right] EV\left[\sin^2(\phi_m)\right] = \frac{1}{2}\sum_{m=1}^{M'} EV\left[\left|\boldsymbol{E}_s(m)\right|^2\right] = \sigma_R^2 . \tag{3-11}$$

The backscattered light $\boldsymbol{E}_s$ is usually taken as a CCG variable so that the real and imaginary parts are Gaussian random variables [71]. As there is no correlation between the real and imaginary parts and their expected value equal to zero, the joint probability density function (PDF) for R and I can be expressed as:

$$PDF_{R,I}(R,I) = \frac{1}{2\pi\sigma_J^2}\exp\left(-\frac{R^2+I^2}{2\sigma_J^2}\right) \tag{3-12}$$

with $\sigma_J^2 = \sigma_R^2 = \sigma_I^2$. The joint probability density function for amplitude and phase of the Rayleigh signal can be obtained from Eq. 3-12 by the relation $R = |\boldsymbol{E}|\sin\theta$ and $I = |\boldsymbol{E}|\cos\theta$ [68]:

$$PDF_{|\boldsymbol{E}|,\theta}\left(|\boldsymbol{E}|,\theta\right) = PDF_{R,I}(R,I)\begin{vmatrix}\partial R/\partial|\boldsymbol{E}| & \partial R/\partial\theta \\ \partial I/\partial|\boldsymbol{E}| & \partial I/\partial\theta\end{vmatrix} = PDF_{R,I}(R,I)\cdot|\boldsymbol{E}| = \frac{|\boldsymbol{E}|}{2\pi\sigma_J^2}\exp\left(-\frac{|\boldsymbol{E}|^2}{2\sigma_J^2}\right) \tag{3-13}$$

for $|\boldsymbol{E}| \geq 0$ and $\theta \in [-\pi, \pi]$.

Then the density function for the amplitude is calculated based on Eq. 3-13:

$$PDF_{|\boldsymbol{E}|}\left(|\boldsymbol{E}|\right) = \int_{-\pi}^{\pi}\frac{|\boldsymbol{E}|}{2\pi\sigma_J^2}\exp\left(-\frac{|\boldsymbol{E}|^2}{2\sigma_J^2}\right)d\theta = \frac{|\boldsymbol{E}|}{\sigma_J^2}\exp\left(-\frac{|\boldsymbol{E}|^2}{2\sigma_J^2}\right) \tag{3-14}$$

which is a Rayleigh distribution with a scale parameter σ_J. The density function of the optical phase is obtained:

$$PDF_\theta(\theta) = \int_0^{\infty}\frac{|\boldsymbol{E}|}{2\pi\sigma_J^2}\exp\left(-\frac{|\boldsymbol{E}|^2}{2\sigma_J^2}\right)d|\boldsymbol{E}| = \frac{1}{2\pi} \tag{3-15}$$

in the range $[-\pi, \pi]$. It is obvious that the joint probability density function for amplitude and phase shown in Eq. 3-13 is the product of $p_{|\boldsymbol{E}|}(|\boldsymbol{E}|)$ and $p_\theta(\theta)$, so the resultant amplitude and the phase are statistically independent variables [68].

Then the Rayleigh intensity trace is analysed, which can be obtained by direct detection as the backscattered light beats with itself at the photodetector. Hence it is expressed as

$$I(z) = \left|\boldsymbol{E}(z)\right|^2 = \sum_{m=1}^{M'}\boldsymbol{E}_s^2(m) + 2\sum_{m=1}^{M'-1}\sum_{n=m+1}^{M'}\boldsymbol{E}_s(m)\boldsymbol{E}_s(n). \tag{3-16}$$

Since the intensity and amplitude $|\boldsymbol{E}|$ are positive values, Eq. 3-16 shows that the relation between intensity and amplitude is monotonic, so that the density function of the intensity trace can be obtained from the amplitude PDF [70]:

$$PDF_I(I) = PDF_{|\boldsymbol{E}|}\left(\sqrt{I}\right)\left|\frac{d|\boldsymbol{E}|}{dI}\right| = \frac{1}{2\sqrt{I}}PDF_{|\boldsymbol{E}|}\left(\sqrt{I}\right). \tag{3-17}$$

Inserting the expression of amplitude density function $p_{|\boldsymbol{E}|}(|\boldsymbol{E}|)$ into Eq. 3-17, the intensity PDF is finally expressed as:

$$PDF_I(I) = \frac{\sqrt{I}}{\sigma_J^2}\exp\left(-\frac{I}{2\sigma_J^2}\right)\frac{1}{2\sqrt{I}} = \frac{1}{2\sigma_J^2}\exp\left(-\frac{I}{2\sigma_J^2}\right) \tag{3-18}$$

which obeys an exponential distribution with a scaling parameter:

$$2\sigma_J^2 = \sum_{m=1}^{M'} EV\left[\left|\boldsymbol{E}_s(m)\right|^2\right] = \sum_{m=1}^{M'} EV\left[I(m)\right] = M\cdot\bar{I}_s, \tag{3-19}$$

where $\bar{I}_s$ is the average intensity of the scattered light within the pulse width. Hence the PDF for the intensity trace can be rewritten as

$$PDF_I(I) = \frac{1}{M'\cdot\bar{I}_s}\exp\left(-\frac{I}{M'\cdot\bar{I}_s}\right). \tag{3-20}$$

The analysis above shows that the amplitude and intensity of COTDR traces obey Rayleigh and exponential distributions, respectively, based on the random walk theory. And it agrees well with the reported analysis by different methods [40, 41, 72].

3.2.2 Simulation and experiment for the temporal property of coherent Rayleigh trace

The statistical property of coherent Rayleigh traces obtained in the previous section is investigated by the experiment shown in Fig. 3-5. A distributed-feedback laser (DFB) working at 1550 nm with ~ 1 MHz linewidth is chosen as the light source. The continuous wave (CW) is converted into 10 ns wide rectangular pulses, corresponding to 1 m spatial resolution, by an electro-optic modulator (EOM) driven by a 2.3 GS/s arbitrary waveform generator (AWG). Another EOM is employed as an optical gate to enhance the extinction ratio of the optical pulse [73]. In order to optimise the modulation performance, two polarisation controllers (PC) are employed before the EOMs to adjust the SOP of the light. The optical pulse is boosted by an Erbium-doped fibre amplifier (EDFA) and the amplified spontaneous emission (ASE) noise is suppressed by a band pass filter (BPF) with 100 GHz width. The optical power of the pulse is adjusted (< 400 mW) by a tunable attenuator to avoid modulation instability [55]. Finally, the pulse is launched into a 1-km SMF through a circulator. The weak backscattered light is amplified by another EDFA and a narrow-band (5 GHz) FBG is employed to suppress the ASE. The intensity of the Rayleigh backscattered light is acquired by a photodetector with 1 GHz bandwidth and the temporal trace is displayed on a 4 GHz oscilloscope.

The statistical property of the simulated traces is also analysed here to compare theory with experiment. While the average effective refractive index is considered equal to 1.46, the equivalent effective refractive index variation $\Delta n'_{eff}(z)$ and the scattering coefficient is randomly generated at each sampling point based on a zero Gaussian probability distribution. The standard deviation of the reflection coefficient is believed to be the reciprocal of the scattering points inside the optical pulse [74]:

$$\sigma_r^2 = \frac{1}{M'} = \frac{2\Delta z}{w} \approx \frac{2\lambda}{w} \approx 1.55\times10^{-6}, \tag{3-21}$$

when the optical wavelength is 1550 nm and the spatial resolution is 1 m (w = 2 m). And the effective index variation is about 7.5×10^{-7} at 1550 nm for a standard fibre, according to Eq. 3-1. Other parameters are taken identical to the experiment; however, the fibre loss is neglected due to the short distance. The integral step for Eq. 3-3 is 0.1 m corresponding to 1 GS/s sampling rate.

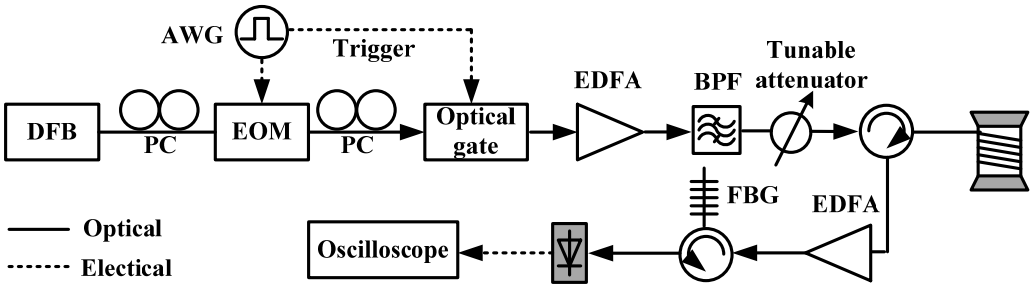

Figure 3-5. Experimental setup to validate the temporal property of the coherent Rayleigh trace. DFB: distributed feedback laser, EOM: electro-optic modulator, EDFA: erbium-doped fibre amplifier, AWG: arbitrary waveform generator, PC: polarisation controller, BPF: band pass filter, FBG: fibre Bragg grating.

According to random walk theory, the amplitude and intensity of a coherent Rayleigh trace obey to Rayleigh and exponential decaying distributions, respectively, regardless of the pulse shape. The probability density of the simulated amplitude normalised to its average value is shown in Fig. 3-6a. The solid line represents the Rayleigh distribution with a scale parameter of 0.79. This value is close to the theoretical result $\sqrt{1/2} \approx 0.7$ based on Eq. 3-22. It is obvious that the simulation result is clearly Rayleigh distributed. The modulus of the light amplitude is equal to the square root of the obtained signal. And Fig. 3-6a shows that the experimental results can be considered as Rayleigh-distributed. Actually, several similar experiments with coherent detection have confirmed the Rayleigh distribution of the amplitude of the COTDR trace [40, 65, 67].

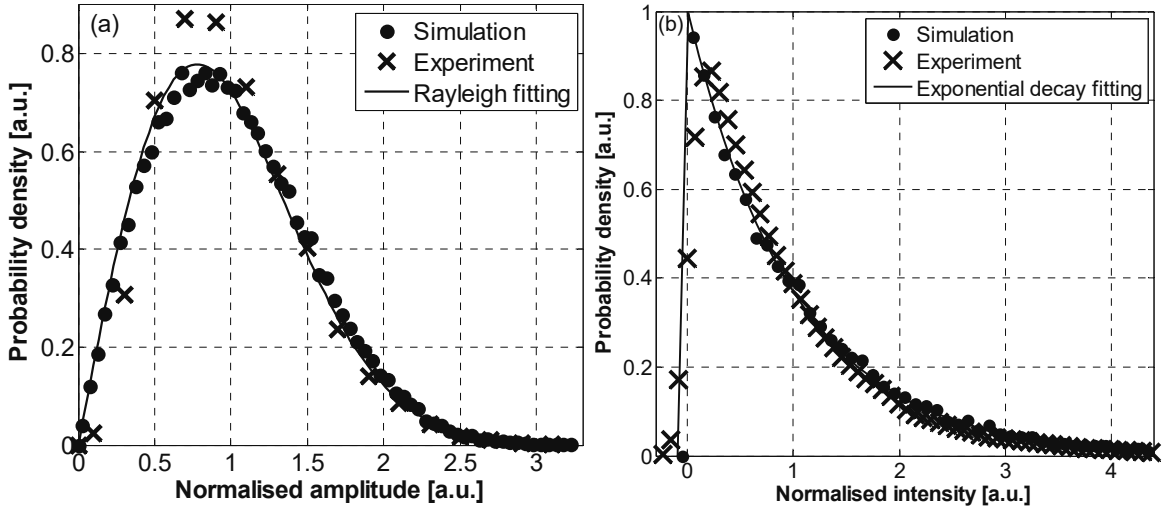

Figure 3-6. Probability density of coherent Rayleigh trace in (a) amplitude and (b) intensity.

Both experiment and simulation results demonstrate a clear exponential decaying trend of the normalised intensity of Rayleigh signal as shown in Fig. 3-6b, presenting a good agreement with the theory. There are some small deviations that can be explained by the limited number of simulation points and the noise in the experiment. The "negative" intensity of the experimental results is probably due to noise perturbation. On the other hand, the simulation result demonstrates a clear exponential distribution because it is noise free.

3.3 Spectral properties of coherent Rayleigh traces

Although the temporal Rayleigh trace carries the environmental information for distributed measurement, the spectral properties also play a very important role in the COTDR sensor. The coherent Rayleigh trace demonstrates a fast oscillation, so that a low speed receiver would smooth the stochastic varying trace and change the statistic feature of obtained signal, thus useful information may be lost. Actually, the COTDR signal is believed to oscillate vary fast, so that the photodetector bandwidth should be several times broader than the incident pulse spectrum [73]. But a large bandwidth usually introduces more noise and finally deteriorates the sensing performance. Hence, it is crucial to investigate the frequency spectrum of the COTDR trace to determine the optimal bandwidth.

3.3.1 Theory of the spectral feature of COTDR trace

The number of scattering points inside the pulse width is very large (over thousands) due to the small size of the fibre inhomogeneities. Thus the summation in Eq. 3-5 can be replaced by an integration [75], so the backscattered field is rewritten as:

$$\boldsymbol{E}(z)=\int_0^L P_E\left(\frac{x-z}{w}\right)\cdot \boldsymbol{E_0} e^{-\alpha z}\cdot r(x)\cdot e^{j2\phi}dx = H_E(z)\otimes P_E\left(\frac{z}{w}\right), \tag{3-22}$$

where $\otimes$ denotes convolution, L is the fibre length, $H_E(z) = \boldsymbol{E}_0 \cdot \boldsymbol{r}(z)e^{j2\phi}$ is the fibre response under a continuous incoming light $\boldsymbol{E}_0$, and z is the fibre position that obeys $0 < z \leq L$. The fibre loss is neglected here for simplicity. It is clear that the backscattered light in a COTDR system is the convolution of the input pulse and the fibre impulse response, the same as the standard OTDR system [76]. In addition, the fibre acts as a low-pass filter with a very small bandwidth for the incident pulse.

Since the reflection coefficient at different scattering points follows a delta correlation as shown by Eq. 3-3, the fibre response $H_E(z)$ also obeys a delta correlation: $\langle H_E(z)H_E^*(z')\rangle = I_0 r_0^2 \delta(z-z')$ with $I_0 = \langle E_0 E_0^*\rangle$. According to the expression of the impulse response $H_E(z)$, it is statistically independent of the pulse shape P_E. Thus the autocorrelation of the backscattered light field is expressed as:

$$\begin{aligned} R_E(z+\delta z, z) &= \int_0^L\int_0^L \left\langle H_E(z_1)H_E^*(z_2)\right\rangle \left\langle P_E(z+\delta z-z_1)P_E^*(z-z_2)\right\rangle dz_1 dz_2 \\ &= I_0 r_0^2 \cdot \int_0^L \left\langle P_E(z+\delta z-z_1)P_E^*(z-z_1)\right\rangle dz_1 \\ &= I_0 r_0^2 \cdot R_E^P(z+\delta z, z) \end{aligned}, \tag{3-23}$$

where R_E^P the autocorrelation of pulse shape and this value is dependent only on δz for a given pulse. Thus, Eq. 3-23 demonstrates that the autocorrelation of the backscattered light is a function only on the time interval which is determined by δz.

In addition, the coherent Rayleigh scattering is a cyclostationary process synchronised with the incident optical pulse. And the pulse spatial width is usually several metres, much smaller than the whole fibre length. Consequently, the expected value of the backscattered light amplitude can be approximated as time independent [77]. As a result, the coherent Rayleigh scattering can be seen a wide-sense stationary process [75, 77], so that Wiener-Khinchin theorem can be applied.

According to the Wiener-Khinchin theorem, the PSD of the coherent Rayleigh trace $E(z)$ is the Fourier transform of the autocorrelation of the backscattered light. Hence the spectrum of the Rayleigh trace $E(z)$ is expressed as

$$S_E(f) = I_0 r_0^2 \cdot S_E^P = I_0 r_0^2 \cdot \left|\mathrm{F}(P_E)\right|^2, \tag{3-24}$$

where f represents the frequency, S_E^P is the PSD of the pulse and F() denotes the Fourier transform. For a given COTDR system, I_0 and r_0^2 can be considered as constant. Consequently, the spectrum of the reflected light keeps the same spectral shape as the optical pulse.

There is another way to derive the PSD of the Rayleigh trace. As Eq. 3-22 indicates, the obtained trace can be seen as the optical pulse linearly filtered by the intrinsic impulse response. Thus the spectral property of the backscattered field is finally described as: $S_E(f) = |\mathrm{F}(P_E)|^2 \cdot S_E^H$ based on the PSD definition with the PSD of the fibre response $S_E^H = I_0 \cdot r_0^2$ [70].

The autocorrelation of the backscattered light intensity is expressed as:

$$R_I(z+\delta z, z) = \int_0^L \int_0^L \left\langle E(z_1) E^*(z_1) E(z_2) E^*(z_2) \right\rangle dz_1 dz_2 . \tag{3-25}$$

The ensemble average in Eq. 3-25 can be simplified by applying the Gaussian moment theorem $\langle E(z_1)E^*(z_1)E(z_2)E^*(z_2)\rangle = \langle E(z_1)E^*(z_1)\rangle\langle E(z_2)E^*(z_2)\rangle + \langle E(z_1)E^*(z_2)\rangle\langle E(z_2)E^*(z_1)\rangle$ [78], because the electric field is a CCG variable. So the autocorrelation of the intensity trace is calculated to be [75]:

$$R_I(z+\delta z, z) = I_0^2 r_0^4 + \left|R_E\right|^2 . \tag{3-26}$$

The Wiener-Khinchin theorem is also valid for the Rayleigh intensity trace [75]. Thus the PSD of the scattered light intensity is obtained [77]:

$$S_I(f) = I_0^2 r_0^4 \delta(f) + S_E(f) \otimes S_E(f) . \tag{3-27}$$

The spectrum shape of the intensity trace is dependent on the self-convolution of the amplitude spectrum and is finally determined by the pulse shape.

To demonstrate the dependence of the Rayleigh spectrum on the optical pulse shape, the PSD of the backscattered light is analysed in the case of a rectangular pulse

$$\mathrm{rect}\left(\frac{t}{\tau_{rect}}\right) = \begin{cases} 1 & |t| \le \tau_{rect}/2 \\ 0 & |t| > \tau_{rect}/2 \end{cases} \tag{3-28}$$

and a sinc pulse

$$\mathrm{sinc}(t) = \begin{cases} 1 & t = 0 \\ \dfrac{\sin(2\pi t/\tau_{\mathrm{sinc}})}{2\pi t/\tau_{\mathrm{sinc}}} & t \neq 0 \end{cases} \tag{3-29}$$

where τ_{rect} and τ_{sinc} are the full width of the rectangular and sinc pulses, respectively. But the spatial resolution of a distributed fibre sensing system is determined by the full width at half maximum (FWHM). There is no

difference between the full-width and FWHM for a rectangular pulse. However, the FWHM of a sinc pulse is just ~ 60 % of the full width. As a result, the full width of a sinc pulse must be 66.6 % larger than a rectangular pulse τ_{rect} to achieve the same spatial resolution.

With the Fourier transform of the pulse shape, the amplitude PSD of the backscattered light is retrieved from Eq. 3-21:

$$S_E^{\text{rect}}(f) = I_0 r_0^2 \left| \tau_{rect} \cdot \frac{\sin(\pi \tau_{rect} f)}{\pi f} \right|^2 \tag{3-30}$$

for the rectangular pulse and

$$S_E^{\text{sinc}}(f) = I_0 r_0^2 \left| \frac{\tau_{\text{sinc}}}{2\pi} \cdot \text{rect}(\tau_{\text{sinc}} f) \right|^2 \tag{3-31}$$

for the sinc pulse. It is interesting to notice that the amplitude spectrum of the COTDR signal present a sinc-squared shape for the rectangular input pulse and a rectangular shape for the sinc input pulse.

The PSD of the Rayleigh intensity trace is obtained by applying Eqs. 3-28 and 3-29 to Eq. 3-25. For a rectangular pulse, the self-convolution of the sinc squared function is calculated according to Ref. [79]. And the corresponding PSD results in:

$$S_I^{\text{rect}}(f) = I_0^2 r_0^4 \left\{ \delta(f) + \frac{\tau_{rect}}{(\pi f)^2} \left[1 - \frac{\sin(2\pi \tau_{rect} f)}{2\pi \tau_{rect} f} \right] \right\}. \tag{3-32}$$

In the case of a sinc pulse, the self-convolution of the rectangular function results in a triangular function, leading to the expression:

$$S_I^{\text{sinc}}(f) = \begin{cases} I_0^2 r_0^4 \left[\delta(f) + \frac{\tau_{\text{sinc}}^2}{4\pi^2} \left(1 - \left| \frac{f \tau_{\text{sinc}}}{2} \right| \right) \right] & |f| \le 2/\tau_{\text{sinc}} \\ 0 & |f| > 2/\tau_{\text{sinc}} \end{cases}. \tag{3-33}$$

The FWHM of the Rayleigh intensity spectrum for a rectangular pulse is difficult to find because there is no analytic expression for Eq. 3-32. But it can be determined from the spectrum graph. Compared with a rectangular pulse, sinc pulses demonstrate high spectrum efficiency in COTDR systems, because all the Rayleigh signal is confined in the frequency range $\pm 2/\tau_{\text{sinc}}$ for a sinc pulse but it spreads over the full spectrum for a rectangular pulse.

3.3.2 Experiment and simulation of the spectral properties of COTDR trace

The experimental setup to acquire temporal Rayleigh traces can also be utilised to obtain the spectrum of coherent Rayleigh traces using different optical pulses that can be precisely shaped by a high speed AWG. Since the reflected optical pulse at fibre ends may contaminate the spectrum of Rayleigh light, the input of the SMF is spliced to a circulator and the other end is wrapped around an object with small diameter to avoid Fresnel reflection. The Rayleigh backscattered light is split into two branches for different analyses, as shown in Fig. 3-7. In the upper branch, the oscilloscope in Fig. 3-5 is replaced by an electric spectrum analyser (ESA), so that

the spectrum of the COTDR intensity trace can be obtained. In the lower branch, the light enters an advanced optical spectrum analyser (OSA) with 5 MHz resolution. There is a built-in tunable laser inside the OSA acting as a local oscillator (LO) and its beating with the input light is shown. Consequently, the Rayleigh signal is obtained by coherent detection and the corresponding amplitude spectrum is directly displayed by the OSA, even though the setup shown in Fig. 3-5 cannot detect the amplitude of the backscattered light in time domain.

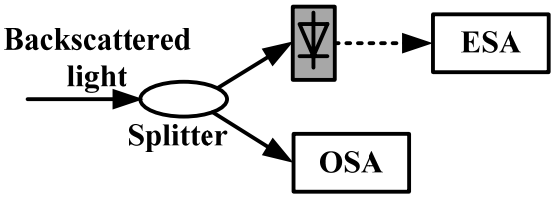

Figure 3-7. Detection scheme to obtain the spectrum of coherent Rayleigh trace. ESA: electric spectrum analyser, OSA: optical spectrum analyser.

The FWHM of the rectangular and sinc pulses is set at 10 ns, corresponding to full widths of 10 ns and ~ 16.6 ns, respectively. The generated optical pulses are visualised by a fast oscilloscope and shown in Fig. 3-8. It is obvious that the high speed AWG is able to generate rectangular and sinc pulses with a good quality. The overshoot of the rectangular pulse in Fig. 3-8a is due to the limited bandwidth of the photodetector. And the measured sinc pulse confirms the theoretical analysis that the FWHM is about 60 % of the full width, as shown in Fig. 3-8b.

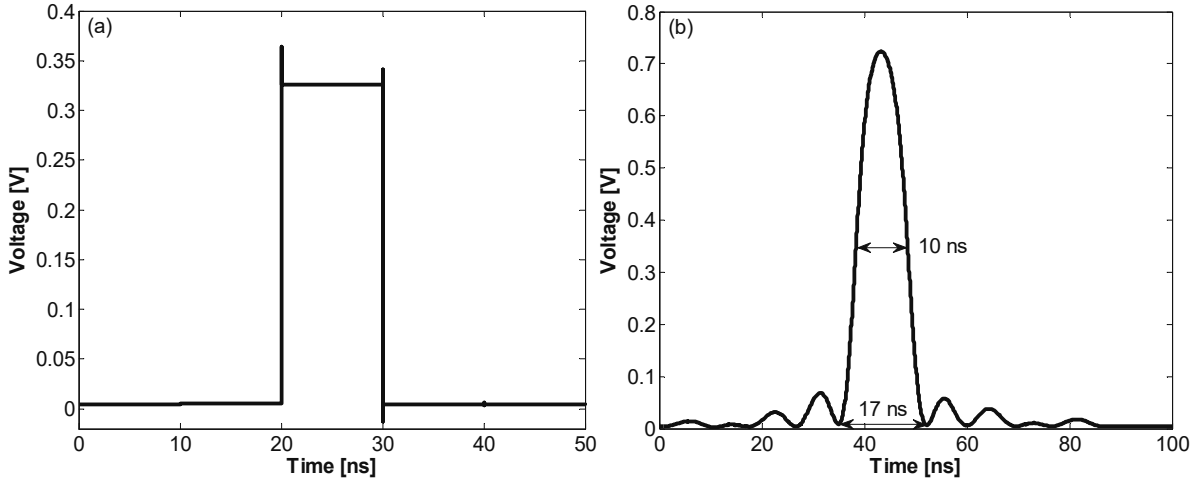

Figure 3-8. Generated (a) rectangular and (b) sinc optical pulse.

The simulation condition is the same as in the last section except that the optical phase of the resultant light ***E*** shown in Eq. 3-3 is simplified as:

$$2\int_{z}^{z+m\Delta z}\beta(x)dx = 2\int_{z}^{z+m\cdot\Delta z}\frac{2\pi n_{eff}(\xi)\nu}{c}d\xi = \frac{4\pi\nu}{c}\sum_{i=0}^{m} n_{eff}(z+i\cdot\Delta z)\cdot\Delta z \approx \frac{4\pi\nu\Delta z}{c}\left(m\cdot n_{ave}+\Delta n_{eff}\right), \quad (3\text{-}34)$$

because M is usually large enough to approximate the average refractive index by n_{ave} within the interval from z to $z+(m-1)\Delta z$. The rectangular and sinc pulses are simulated by 10 points and 16 points, respectively, for a 1 GS/s sampling rate.

With the optical pulse shown in Fig. 3-8, the spectra of coherent Rayleigh traces are obtained by the detection scheme presented in Fig. 3-7. The simulated spectrum can be also retrieved by Fourier transform of the

corresponding COTDR traces generated based on the model. Thus the theoretical, simulated and experimental results can be compared with each other.

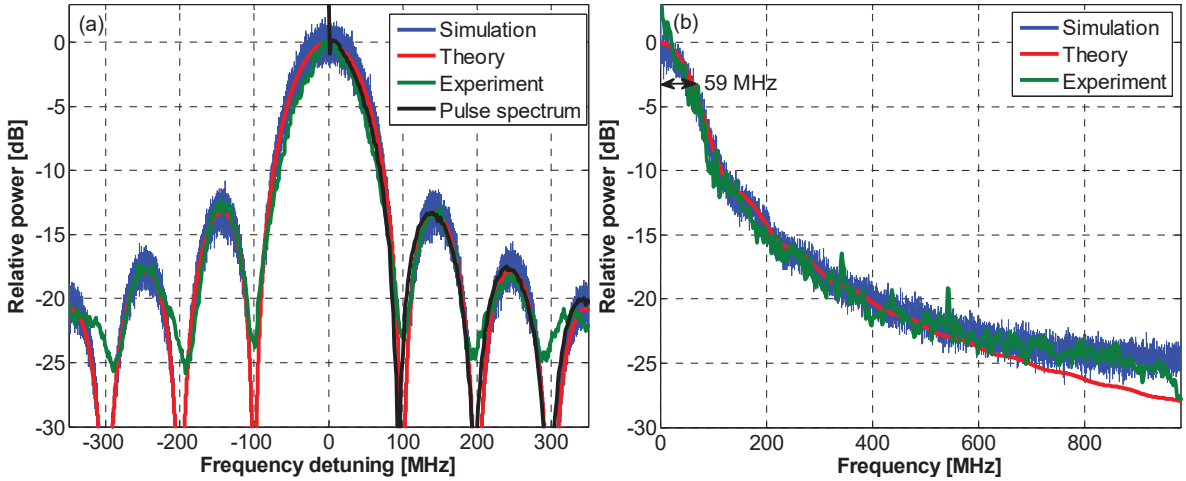

Figure 3-9. (a) Amplitude and (b) intensity spectra of a COTDR trace with a 10-ns rectangular input pulse.

The spectra of the COTDR trace with a 10 ns rectangular incident pulse are presented in Fig. 3-9. It shows the evidence that the simulation and experiment agree with the theory. The amplitude spectra of the COTDR trace obtained by simulation and experiment demonstrate a sinc-squared shape as predicted by the theoretical analysis, as presented in Fig. 3-9a. And the obtained trace spectra demonstrate the same shape as the rectangular pulse spectrum acquired by the ESA. Although there exists some information at higher frequency, most of the power is confined in the range from DC to 100 MHz. According to the rectangular pulse spectrum shown in Fig. 3-9a, the 3-dB bandwidth of a photodetector to acquire the 10 ns rectangular pulse is about 44 MHz. In addition, the 3-dB bandwidth of the intensity spectrum is ~ 60 MHz according to Fig. 3-9b, corresponding to a FWHM bandwidth of 120 MHz. Simulation results with different pulse width reveal that FWHM bandwidth of intensity trace equals to $1.2/\tau_{rect}$ for rectangular pulse, the same as the reported result in Ref. [75]. Figure 3-9 present that the bandwidth required to detect the coherent Rayleigh trace is broader than the bandwidth to obtain the incident optical pulse.

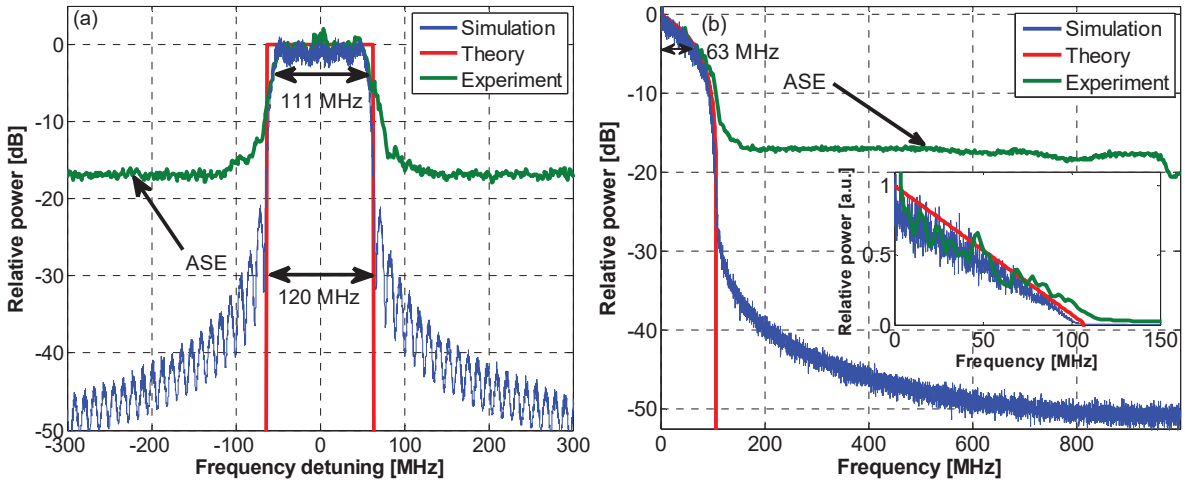

Figure 3-10. (a) Amplitude and (b) intensity spectra of a COTDR trace with a 10-ns sinc input pulse, inset is the intensity spectrum in linear scale.

The agreement between the theory, simulation and experiment is also validated in the case of sinc pulse with 10 ns FWHM ($\tau_{sinc} \approx 17$ ns). The spectra of the amplitude and intensity Rayleigh traces demonstrate rectangular and triangular shape, as shown respectively in Fig. 3-10a and the inset of Fig. 3-10b. The simulation result in Fig. 3-10 shows the gradual power decrease outside the pulse spectrum width, which may be explained by the limited simulation points. The experiment result shows the optical power at higher frequency which is the ASE from the pre-amplifier.

The amplitude spectrum obtained by the experiment demonstrates a quasi-trapezium shape and its FWHM of is about 111 MHz which is a bit smaller than the theoretical analysis above (~ 120 MHz), as shown in Fig. 3-10a. This might be explained by the suppression of the sidelobes due to the second EOM to enhance the extinction ratio of the pulse. As shown in Fig. 3-10b, the 3 dB width of the intensity spectrum is measured to be ~ 63 MHz and it is interesting to point out that this value is slight larger than the value presented in Fig. 3-9b. Consequently, a rectangular pulse is more spectrum efficient than a sinc pulse in a COTDR system.

3.3.3 Effects of photodetector bandwidth on the COTDR trace

The previous section reveals that the spectrum of a COTDR trace is dependent on the optical pulse shape and it is possible that spectrum of the Rayleigh trace is broader than the pulse spectrum. In other words, the temporal trace could oscillate much faster in some cases. As a result, the photodetector bandwidth should be wide enough to acquire all the information from the COTDR trace, but should not be too broad considering the introduced noise and the cost. Hence the effect of the receiver bandwidth needs to be investigated to find the optimal value.

In practice, the amplitude is usually obtained from the beating between the COTDR trace and a LO at a different frequency by coherent detection. Thus the bandwidth of the photodetector is always sufficiently large. For example, some researcher claim that the electrical bandwidth required for coherent detection should be at least twice as large as the received signal [80]. Consequently, it is unnecessary to investigate the influence of receiver bandwidth on the Rayleigh amplitude trace. But it is still unclear what would be the receiver bandwidth to ensure a given spatial resolution in COTDR systems with direct detection.

Both experiment and theory show that the Rayleigh trace with rectangular input pulse is more vulnerable to the photodetector bandwidth because it covers a broader spectrum. Additionally, a rectangular pulse is the most employed pulse shape in distributed fibre sensing to avoid self-phase modulation [53]. Thus the influence of the receiver speed is analysed only for the rectangular incident pulse.

The last section reveals the relation between the pulse width and the FWHM of the Rayleigh trace, which is supposed to be the minimum acceptable bandwidth for the photodetector. Here the effect of the bandwidth on the temporal trace is investigated to validate that this relationship actually determines the optimal bandwidth.

A receiver with a limited bandwidth would smooth the Rayleigh trace, leading to a change of its statistic feature. This influence is studied by simulation and experiment in the case of a 10 ns rectangular incident pulse. To obtain the trace using different photodetector bandwidths, the simulated trace is filtered by averaging neighbouring points while the experiment trace is processed by the internal digital filter of the oscilloscope. The probability distributions of the Rayleigh trace normalised to its average for different bandwidths are shown in Fig. 3-11, and there is no obvious change of the statistic properties until the filter bandwidth reduces below 125 MHz, which is very close to the twice of the 3-dB bandwidth of the spectrum depicted in Fig. 3-9b. When the bandwidth is too narrow, the trace will be smoothened so much that the density peak shifts to the average intensity position, as shown in Fig. 3-11d, and the intensity trace no longer follows an exponential distribution.

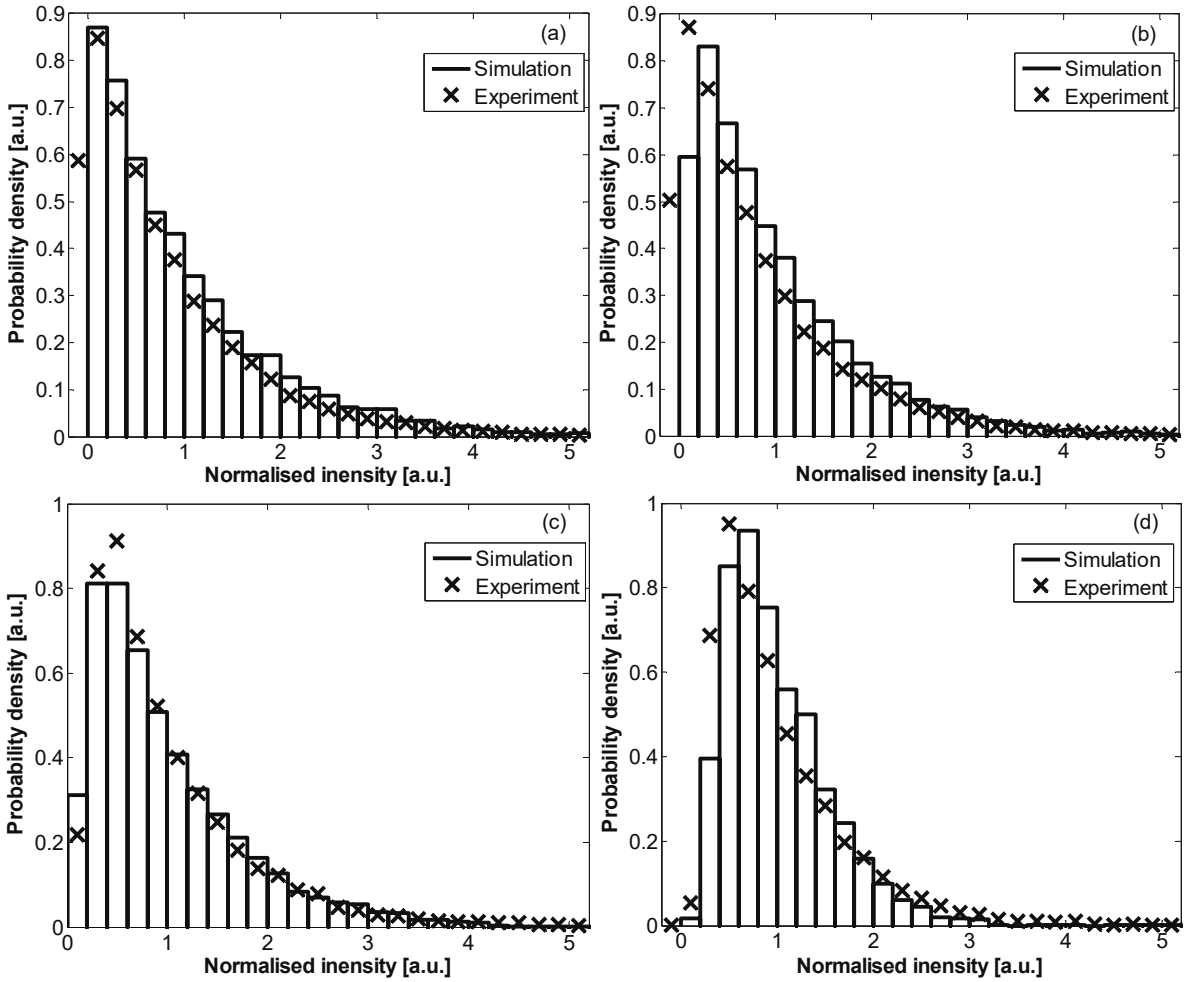

Figure 3-11. Probability distribution of COTDR intensity trace with 10-ns incident pulse obtained with a photodetector bandwidth of (a) 1GHz, (b) 250 MHz, (c) 125 MHz and (d) 50 MHz.

The smoothened trace becomes more uniform along the fibre so that the visibility $V = (I_{max}–I_{min})/(I_{max}+I_{min})$ of the trace, an important factor to evaluate the quality of the COTDR trace [73], will also be reduced. Figure 3-12 shows that the visibility obtained from experiment and simulation decreases when the bandwidth becomes smaller. Although the visibility changes little with a 125 MHz filter, it drops a lot when the 50 MHz filter applies, representing that the stochastic varying Rayleigh trace turns to be flattened because of the averaging of the limited bandwidth.

And it has to be pointed out the visibility never reaches 1 in the experiment, as shown in Fig. 3-12b, which is probably due to the noise in the experiment. However, the visibility of the simulated trace is almost 1 along the fibre when the bandwidth is 1 GHz because no noise is introduced to the trace in the simulation.

Figure 3-12 shows that the visibility becomes worse when a narrow bandwidth is applied; and this trend is presented more evidently in Fig. 3-13, in which the visibility averaged along the fibre is plotted as a function of the bandwidth. Obviously, the visibility remains comparatively high when the photodetector bandwidth is above 125 MHz, which is again close to three times of the 3 dB bandwidth of the intensity trace spectrum; but it starts to decrease rapidly when the bandwidth is under this value, meaning that the coherent Rayleigh trace losses contrast due to the low bandwidth.

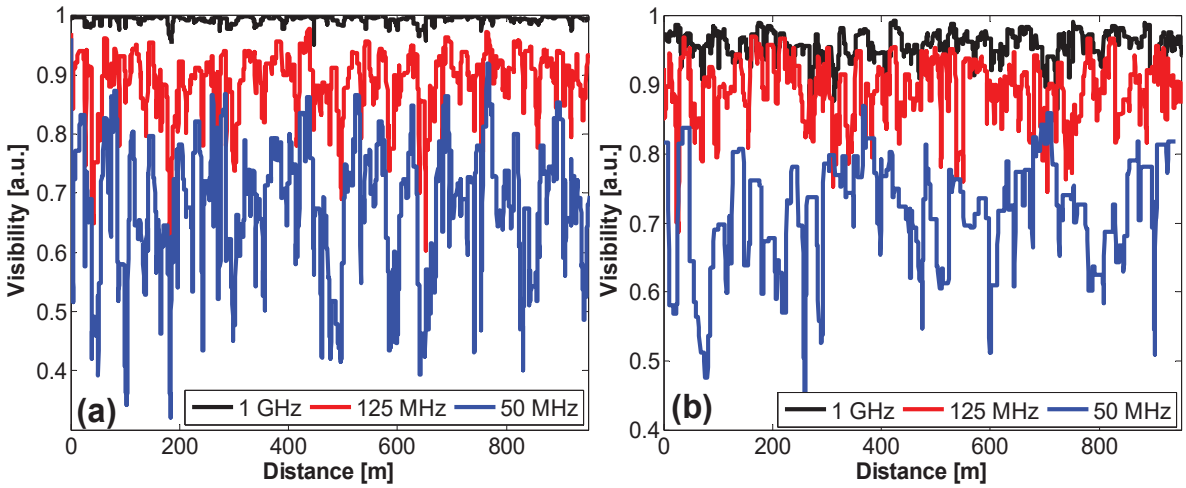

Figure 3-12. Influence of bandwidth on the visibility of the coherent Rayleigh trace obtained by (a) simulation and (b) experiment.

The distributed fibre sensor based on coherent Rayleigh scattering needs to detect the trace shape change induced by the environmental variations. Thus a fast photodetector is necessary to keep the sensing performance. The analysis above in time and frequency domain demonstrates that ~ 120 MHz is the minimum requirement for the 3-dB bandwidth of a detector to obtain a comparatively high quality COTDR signal with 10 ns rectangular pulse. And based on the simulation results with different pulse widths, this conclusion can be generalised: a 3 dB bandwidth needed to detect the COTDR intensity trace is at least equals to $1.2/\tau_{rect}$ in the case of an incident rectangular pulse with a τ_{rect} temporal width.

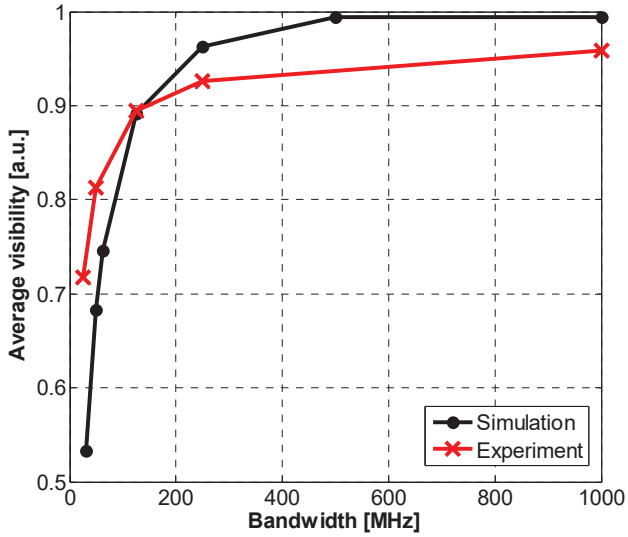

Figure 3-13. Averaged visibility of the simulated and experimental coherent Rayleigh trace under different bandwidth.

3.3.4 Conclusions

In this section, the spectral property of the coherent Rayleigh trace is investigated and the optimal detection bandwidth is determined. The power spectrum density of the COTDR trace turns to be dependent on the input pulse shape. The trace spectrum with rectangular and sinc incident pulse is calculated and validated by experiment and simulation. It shows that the 3-dB bandwidth of the intensity trace with a square incident pulse is $0.6/\tau_{rect}$. Then the effects of bandwidth on the statistic distribution and visibility of the intensity trace are

investigated by experiment and simulation. The result confirms that a bandwidth of $1.2/\tau_{rect}$ is needed to acquire a coherent Rayleigh trace with an acceptable quality, obtained by direct detection, which is around three times as the bandwidth to detect the incident rectangular pulse.

3.4 Sensing range increase for COTDR

Although the optical power of a coherent Rayleigh signal varies randomly, the tendency average of the backscattered optical power decreases exponentially like in a traditional OTDR system, described by Eq. 2-34. The reflected light becomes weaker as the sensing distance increases simply due to the fibre attenuation. As a result, a low SNR is expected at the far end of the fibre and the fibre loss finally limits the sensing distance. For example, Fig. 3-14 shows a coherent Rayleigh trace for a 50-km long fibre with 2 m spatial resolution. The received signal seems totally vanished after 20 km and the Fresnel reflection cannot be seen at the far end of fibre, as shown by the inset, proving the received trace at the very end is actually the noise floor.

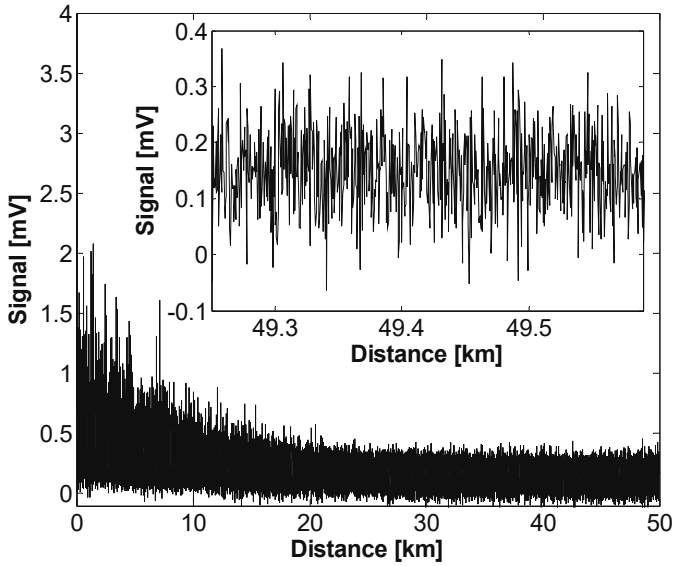

Figure 3-14. Coherent Rayleigh trace for 50 km fibre. Inset, zoom in of the end of the fibre.

A simple way to maintain a comparatively high SNR for a long sensing distance is to increase the peak power of the optical pulse. But the peak power is limited by the nonlinear effects inside the fibre. In a COTDR system, the optical power should stay below the threshold of modulation instability, otherwise signal fading will occur [55]. Employing longer pulse is also a feasible method but this will degrade the spatial resolution as analysed in the last chapter. In addition, averaging the obtained signal can enhance the SNR at the expense of measurement time, which would undermine vibration sensing performance of the COTDR system. Actually, for any distributed fibre sensing system, SNR, measurement time, spatial resolution and the sensing distance are interrelated parameters.

The trade-off amongst all the mentioned parameters is considered to be the fundamental rule limiting the DFS performance. Thus extra effects are needed to increase the sensing range and one of them is the optical amplification. As optical amplifier such as an EDFA is the most popular component to boost the optical signal. Besides, Raman amplification is widely used in fibre sensing and optical communication, but it introduces relative intensity noise and the pump requires high power. Recently, the Brillouin amplifier has also been proposed to elongate the sensing distance [59], which requires less optical power but show large excess noise.

3.4.1 Pre-amplification for a COTDR system

The pre-amplification, increasing the signal light before the receiver, has been applied to DFS based on Brillouin scattering and gains great successes [81]. Actually, the experiment shown in Fig. 3-5 utilizes this technique because the backscattered light power is too low for the 1 GHz photodetector. But compared to the pre-amplifier in a Brillouin sensor, the weak signal in a COTDR system requires the EDFA to work at very low input power and to introduce little ASE noise.

A coherent Rayleigh trace is obtained for a 50-km long SMF by the experimental setup shown in Fig. 3-5 and the pulse width is set to 20 ns. In the last section, it is proved that a photoreceiver with a bandwidth twice broader than the pulse spectrum is enough to detect the coherent Rayleigh scattering trace. Thus a 125 MHz photodetector is employed for this long distance measurement. This comparatively low speed receiver is good at detecting weak signal because it introduces less noise and has higher transimpedance gain. Two EDFAs with the same noise figure of 5 dB but different minimum input power (–10 dBm and 3 dBm) are used to amplify the backscattered light. The EDFA with low input power also introduces low noise. And two FBGs with different reflection spectrum width (5 GHz and 10 GHz) are employed to filter out the ASE from the pre-amplifier. The narrow FBG demonstrates a stronger reflection than the broad one does.

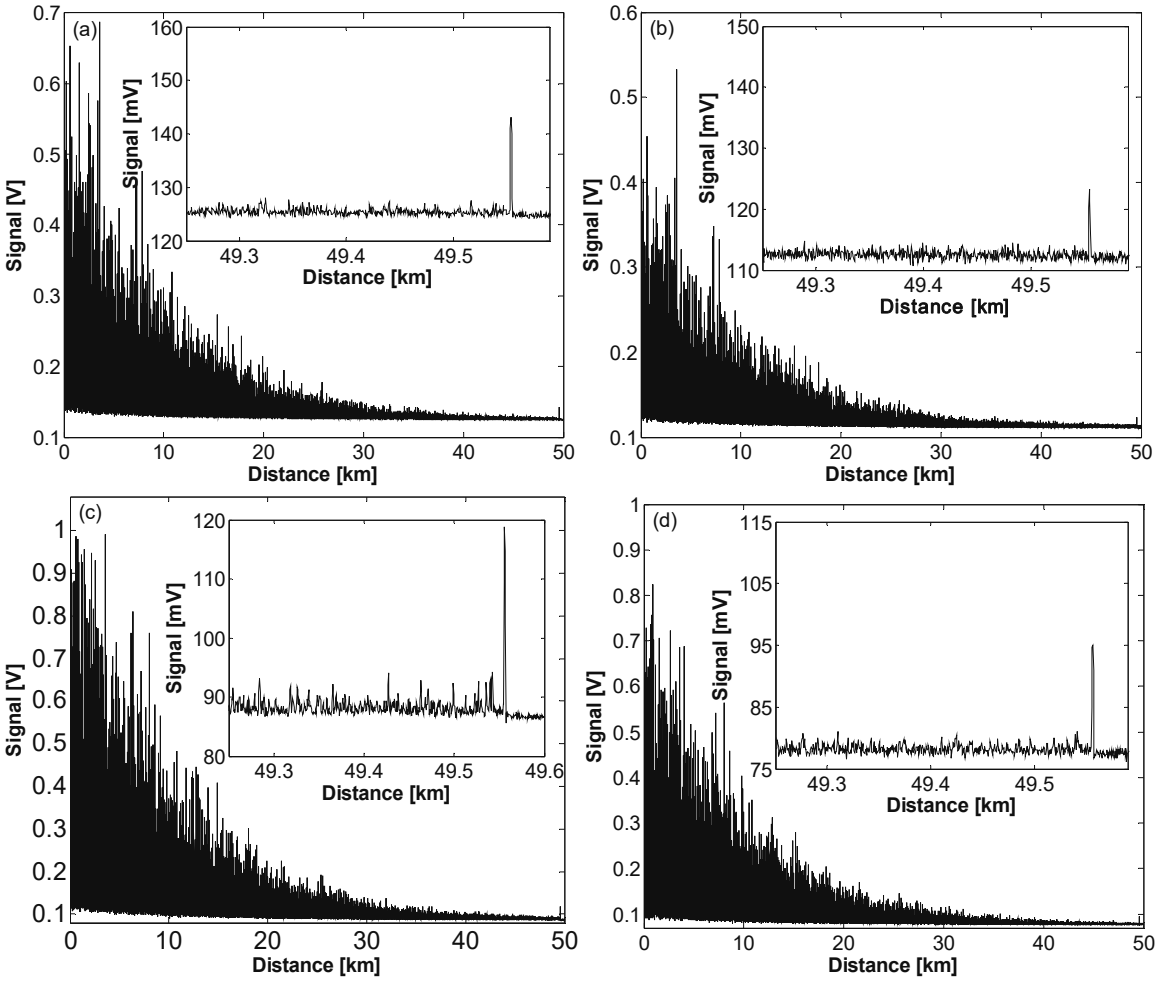

Figure 3-15. Pre-amplified 50 km coherent Rayleigh trace under different condition. Inset: end of the fibre. (a) high noise EDFA and broad FBG, (b) high noise EDFA and narrow FBG, (c) low noise EDFA and broad FBG, (d) low noise EDFA and narrow FBG.

Pre-amplified COTDR traces under different conditions are shown in Fig. 3-15, and it is clear that the signal gets significant enhancement, compared with the trace in Fig. 3-14. Thanks to this amplification, it is possible to reach 50 km sensing distance as all the insets present a distinguishable trace end. And the obtained traces exhibit an obvious exponential decaying trend due to the fibre loss. Since the backscattered light is too weak, an EDFA requiring high input power cannot work properly, thus Rayleigh signal shown in Fig. 3-15a and 3-15b is less enhanced than the traces in Fig. 3-15c and 3-15d, which are amplified by the low noise EDFA.

All the acquired coherent Rayleigh traces exhibit a constant voltage due to a direct current (DC) from the photodetector caused by the ASE from the pre-amplifier. More ASE is blocked by the narrow FBG so that the DC level in Fig. 3-15b and 3-15d is lower. However, the traces filtered by the narrow FBG seem noisier than the broad FBG filtered trace, as shown by the insets of Fig. 3-15. This is probably due to a misalignment of the amplified trace to the FBG reflection spectrum centre. If the incident light is well aligned to the centre, the acquired traces should demonstrate a higher voltage than the traces filtered by the broad FBG. But Fig. 3-15 show a totally opposite situation, lower signal amplitudes are observed in the case of using the narrow FBG, confirming this misalignment. Thus, the ASE from the EDFA, instead of the amplified trace, is more strongly reflected at the centre of the FBG spectrum, resulting in a noisier trace.

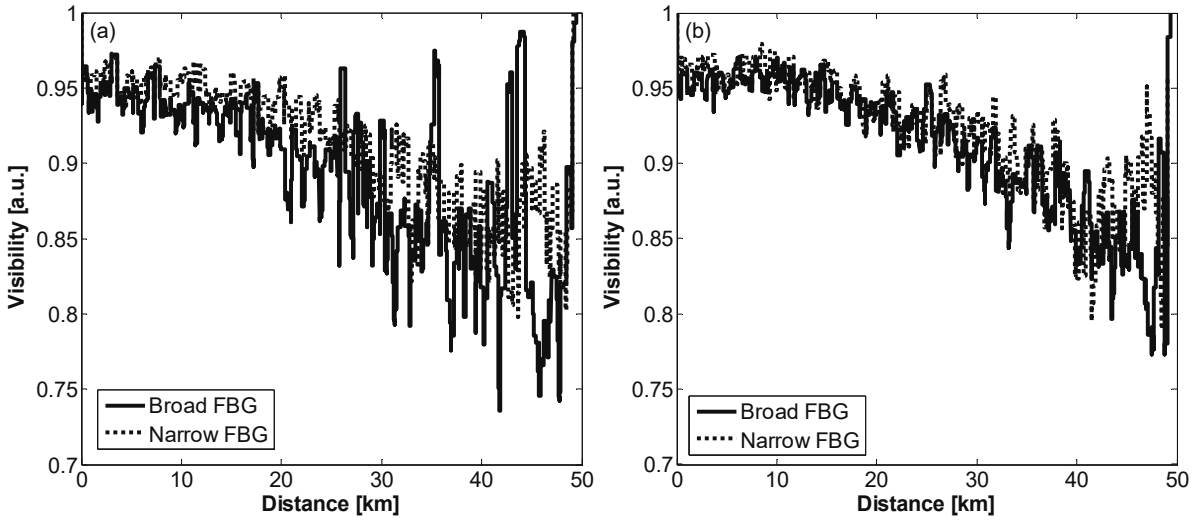

Figure 3-16. Visibility of the coherent Rayleigh trace pre-amplified by (a) high noise EDFA and (b) low noise EDFA.

To compare the performance of the pre-amplification under different conditions, the visibility of the amplified traces is plotted in Fig. 3-16. In this case, the DC voltage is removed from all traces. High visibility is achieved at the beginning of the fibre, but the signal contrast starts to degrade after 20 km because of the lower SNR. In general, the visibility shown in Fig. 3-16b is slight higher than that in Fig. 3-16a, especially at the far end of the fibre, demonstrating again that EDFA with lower input power is more suitable to amplify the backscattered light. But the traces filtered by the narrow FBG show no evident better visibility than the broad FBG filtered traces, which may also be explained by the misalignment. Consequently, it is important to use low noise amplifier and position the amplified trace to the reflection spectrum centre of a narrow FBG to obtain a COTDR trace with good quality.

3.4.2 In-line Brillouin amplification for a COTDR system

In the stimulated Brillouin scattering process, the optical power from a strong optical beam would transfer to the counter propagating light at the Stokes frequency. Thus the weak signal can be amplified via SBS as long as a

phase matching condition is fulfilled. As the SBS works more efficiently than the Raman amplification does, a moderate pump power is enough for the Brillouin amplifier instead of high optical power which is necessary in Raman amplification.

Brillouin amplification was first introduced to the COTDR system in 2014 [59]. The Brillouin pump is launched into the far end of the fibre and the counter-propagating optical pulse is amplified. This backward amplification method requires the access to both fibre ends. Later a forward amplification scheme is proposed where the optical pulse and pump are launched at the same end [82]. In this case, the Rayleigh backscattered light is amplified, and the frequency component of the Rayleigh signal can be selectively amplified by changing the frequency offset between the pump and the Rayleigh backscattered light. But the co-propagating pump and optical pulse may introduce MI or four-wave mixing, degrading the trace quality.

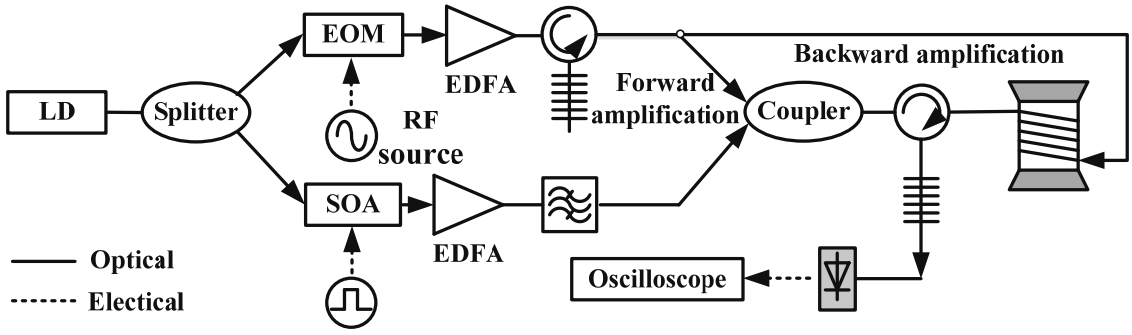

Figure 3-17. Experimental setup of the COTDR with Brillouin amplification. LD: laser diode, EOM: electro-optic modulator, EDFA: erbium-doped fibre amplifier, SOA: semiconductor optical amplifier.

Both Brillouin amplification schemes are realised using the experimental setup shown in Fig. 3-17. The CW light from a laser diode (LD) is split into two branches. In the upper arm, the light passes through an EOM driven by a radio frequency (RF) source. Two sidebands are generated and the carrier is suppressed by tuning the DC voltage applied to the EOM. The generated sidebands are amplified by an EDFA and the one at higher frequency is selected by a tunable FBG (10 GHz) to act as the Brillouin pump. The optical power of the pump is comparatively low, about 3 dBm, due to the high amplification efficiency of the SBS process. In the other branch, the CW light is converted into optical pulses of 20 ns width with high extinction ratio by a semiconductor optical amplifier (SOA). Then the pulse is boosted by another EDFA and the ASE noise is suppressed by a BPF. In the forward scheme, the optical pulse and the pump are coupled together and launched into the fibre under test (FUT) that is a 39-km long SMF. But in the backward amplification, the pump is launched at the far end of FUT. For the in-line amplification, the interaction length is actually the whole sensing fibre or roughly the effective length of the fibre. The light polarisation will rotate randomly within this distance, so the polarisation dependence of the SBS can be averaged out. Hence a special polarisation adjustment is unnecessary in this Brillouin amplification scheme, unlike in a standard Brillouin sensor. Another FBG (5 GHz width) is employed before the photodetector to block the pump or backscattered light of pump. Hence only the COTDR signal enters the photodetector and is acquired by an oscilloscope.

The forward amplification scheme is implemented, giving the result shown in Fig. 3-18. Even though COTDR trace gets amplified compared with the original trace, Fig. 3-18a exhibits that the obtained signal demonstrates fading at some position just like in the case of modulation instability [55]. But the optical spectrum at the far end of FUT, as shown in Fig. 3-18b, reveals that the interference fading of COTDR trace is due to FWM. According to Fig. 3-18b, the pump spectrum is not clean because other generated sidebands, even at higher order, are observed. As a result, the FWM is easily generated while the pump and optical pulse

co-propagate along the fibre, and these sidebands are amplified. The power exchange amongst the light beams leads to a fading at certain positions. To suppress the FWM, the generated sidebands should be totally blocked except the one acting as the pump, the pump power must be low enough and the polarisations of the pump and optical pulse can be manipulated to be orthogonal. But the last two methods would undermine the amplification performance. A possible way is to use a long optical pulse as the pump and offset it with the incident pulse in the COTDR system in time domain.

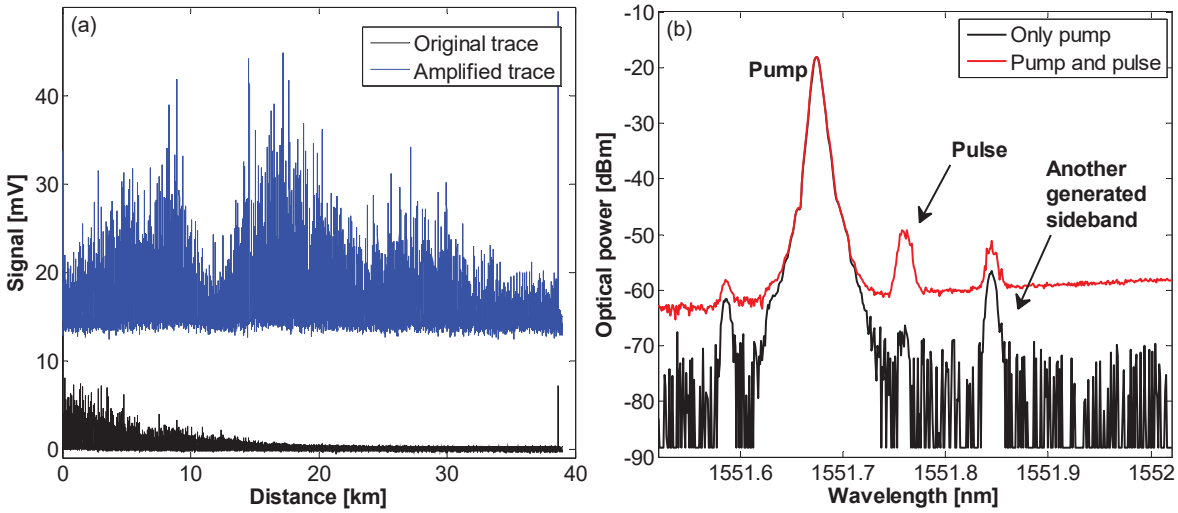

Figure 3-18. (a) Amplified trace and (b) optical spectrum at the far end of fibre in the case of forward Brillouin amplification.

Then tests are carried out with the COTDR trace amplified by the backward scheme and the trace demonstrates no fading along the fibre, as shown in Fig. 3-19, because the counter propagating configuration minimises the FWM. As a result, the pump power can be a bit higher than in the forward pumping case, so a better amplification performance is obtained. For example, the amplitude of the received signal shown in Fig. 3-19 is a little higher than the trace amplified by the forward pumping.

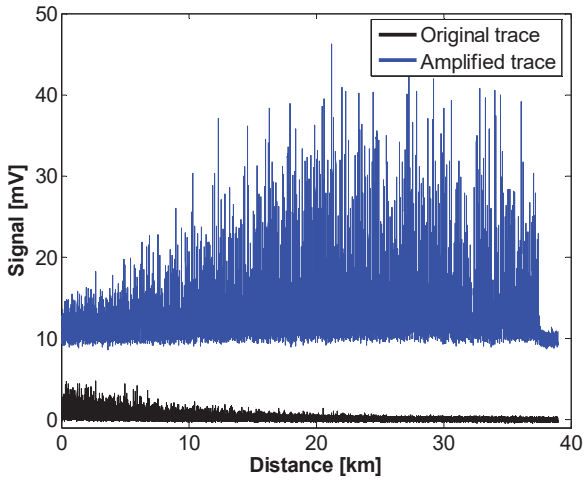

Figure 3-19. Amplified trace by backward Brillouin amplification.

3.4.3 Conclusions

In this section, two amplifying methods, pre-amplification and Brillouin amplification, have been used to enhance COTDR traces in order to achieve longer sensing distance. Generally speaking, the pre-amplification

enhances the signal much more than the Brillouin method. But for in-line amplification, the backscattered light or pulse is enhanced along the fibre, resulting at a more uniform signal.

In the case of pre-amplification, a narrow filter and an EDFA with low input power and low noise are crucial for the quality of the amplified trace. For the Brillouin amplification, the forward method requires single access but introduces FWM unless a time offset is introduced between the pump light and optical pulse for COTDR measurement to avoid any temporal overlap; the backward scheme needs both ends while it avoids FWM thus exhibits better amplification performance.

Chapter 4

Coherent Optical Time Domain Reflectometry for Distributed Sensing

Fibre sensors based on the traditional OTDR technique demonstrate a poor performance when compared to the DFS based on Raman and Brillouin scatterings, as stated in Chapter 2. But Raman and Brillouin sensors show their limit to meet the requirement for high accuracy applications because of their low sensitivities, which are determined by the scattering processes that are essentially difficult to improve. In addition, their sensing performance is degraded in a cryogenic environment. On one hand, the spontaneous Raman scattering is a thermally-activated process and the anti-Stokes Raman intensity quickly vanishes at low temperature. Hence, this technique is poorly suitable for cryogenic measurements. On the other hand, the relationship between the Brillouin frequency and temperature becomes non-monotonic under cryogenic conditions. And the Brillouin based DFS has null temperature sensitivity around 80 K in a standard SMF. However, many fibre point sensors based on the interference process, such as fibre Bragg grating, exhibit comparatively higher sensitivities at even lower temperatures. Therefore it is reasonable to expect that a DFS based on interference will demonstrate higher temperature sensitivities. As analysed in the previous chapter, the coherent Rayleigh scattering is based on the random interference of the backscattered light within the pulse width and the obtained trace shape is dependent on temperature and strain. Consequently, the COTDR could realise distributed measurements with high sensitivities.

The temperature sensitivity of a COTDR sensor is theoretically analysed and experimentally characterised. The temperature sensing performance is examined over a wide range from 77 K to 300 K for different types of optical fibres. And different fibre heating methods are investigated to enhance the sensitivity of the sensor under cryogenic condition.

In section 4.1, the restorability of the coherent Rayleigh trace is demonstrated as the working principle of a COTDR sensor; the temperature sensitivity is investigated based on the mature theory of FBG sensing. And the 1D model from Chapter 3 is employed to simulate temperature sensing.

Then (in section 4.2), a COTDR sensor with the help of a laser frequency stabilisation system is applied to distributed measurements over a wide temperature range. A long distance measurement up to several tens of kilometres is realised using pre-amplification.

In the last section of this chapter, optical heating and electrical heating methods are investigated to increase the fibre temperature in order to enhance the thermal sensitivity under cryogenic conditions. The theoretical

model of the electrical heating is experimentally validated by a double-pulse Brillouin optical time-domain analyser (BOTDA) at room temperature.

4.1 Working principle of a COTDR sensor

The amplitude of a coherent Rayleigh trace varies stochastically as a result of the random interference among the Rayleigh backscattered light from different scattering points along the fibre. As the size and the refractive index of scattering points are both strain and temperature dependent, environmental perturbations will change the interference conditions, resulting in a different trace shape. Based on this phenomenon, the COTDR system has been applied to distributed vibration measurement and perimeter monitoring [83, 84]. In addition, the temporal trace also depends on the optical frequency for the same reason. Since the environmental variations and the optical frequency have the same impact on the interference in the coherent Rayleigh scattering, the trace shape change induced by one factor can be compensated by the change on the other factor. Consequently, a COTDR system can act as a temperature/strain sensor. Its sensitivity is supposed to be similar to that of other sensors based on interferences, like FBG and Fabry-Pérot cavity [85, 86], which are more sensitive than fibre sensors based on Brillouin and Raman scatterings.

4.1.1 Working theory of a FBG sensor

Fibre Bragg grating is a component widely used in the fields of optical communication and fibre sensing. A FBG is essentially a short piece of fibre with a periodically modulated refractive index in the core and a small amount of the incident light is reflected at each index change section. In a uniform FBG, all the reflected light will interfere constructively at the Bragg wavelength λ_B:

$$\lambda_B = 2n_{eff}\Lambda \tag{4-1}$$

where n_{eff} represents the effective refractive index of the fibre and Λ is the period of the refractive index modulation. In other words, the grating couples the light at the Bragg wavelength from the forward-propagating mode into the backward-propagating mode, while light at other wavelength will pass through the grating, the whole process being shown in Fig. 4-1. Consequently, FBGs have been widely employed as optical filters.

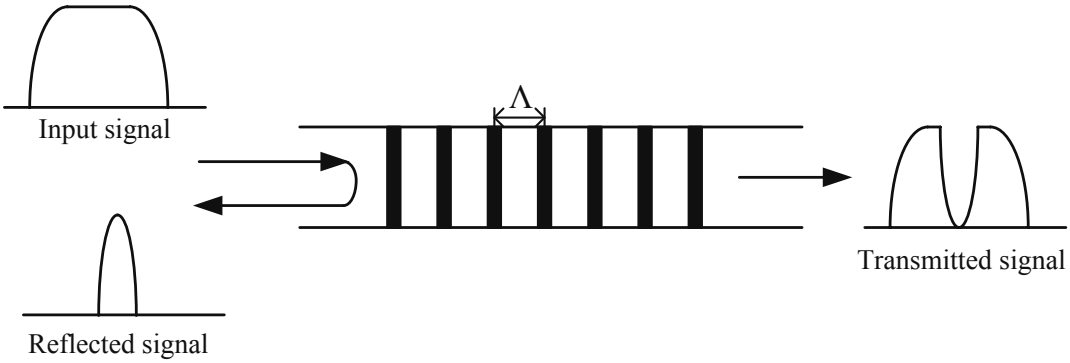

Figure 4-1. Typical structure of a fibre Bragg grating and its spectral response.

According to Eq. 4-1, the reflected spectrum of a FBG is sensitive to mechanical and thermal perturbations because the refractive index and the grating period are both temperature and strain dependent. On one hand,

temperature variations will induce a refractive index change through the thermo-optic effect and a change of the grating period by thermal expansion. On the other hand, an applied strain stretches or compresses the grating, thus changes the period, and causes index variations due to the elasto-optic effect [3]. Therefore, the spectral response of a FBG will change due to temperature and/or strain variations. In Fig. 4-2, theoretical analysis based on transfer matrix method shows that the reflection spectrum will shift for different temperatures [87]. A linear relationship can be built between the Bragg wavelength and the environmental stimuli at room condition, so that the FBG can be utilised for fibre sensing.

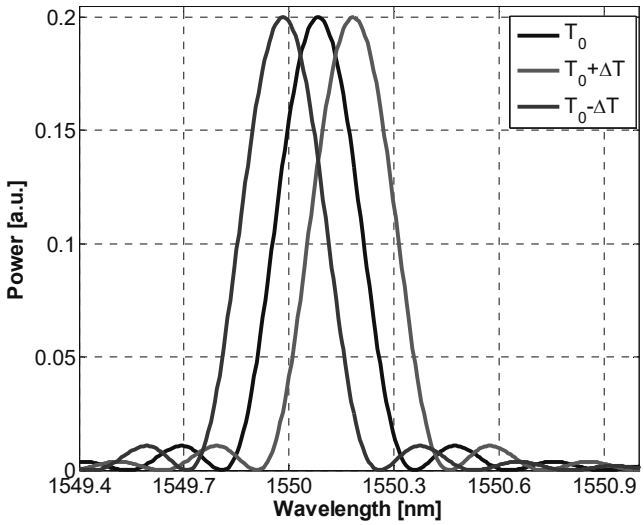

Figure 4-2. Reflection spectra of a fibre Bragg grating under different temperature conditions.

The thermal response of a FBG sensor has been characterised at different temperatures and is widely reported in different literature. The temperature sensitivity reaches ~ 10 pm/K ≈ 1.25 GHz/K in ambient conditions and at 1300 nm [3], which is two orders of magnitude higher than the sensitivity of a standard fibre sensor based on Brillouin scattering. However, the intrinsic sensitivity of the FBG drops significantly under cryogenic conditions due to the decreased thermo-optic coefficient at low temperature [88].

4.1.2 Sensing theory of a COTDR sensor

In a COTDR system, a highly-coherent optical pulse is deflected by stationary, but randomly positioned scattering centres while it propagates through the fibre; and the light backscattered from different scattering centers interferes within the pulse width on the photodetector, resulting in a randomly varying signal in the time domain. Since the measured temporal traces originate from the interference process, the obtained signal is highly dependent on the optical frequency and the frozen longitudinal profile of the refractive index. Thus, random fluctuations of the refractive index along the fibre lead to a signal with a stochastic varying amplitude, which can be perfectly reproduced under identical experimental conditions (temperature, strain and optical frequency). An optical frequency change has the same impact on the obtained signal as a variation of the refractive index. This effect is called restorability, meaning that the changes of the trace shape induced by the refractive index variations, due to temperature/strain perturbations, can be fully compensated by an optical frequency detuning [89]. Hence the optical frequency change can be converted into information about temperature and strain.

The theoretical model from Chapter 3 can be applied to simulate the restorability of coherent Rayleigh traces. An original trace is simulated at a given optical frequency and with a random variation of refractive index along a 20-m optical fibre. Then a small refractive index change of 1×10^{-6} is applied over the whole fibre, resulting in a totally different trace shape, as presented in Fig. 4-3. But this modified trace can be restored to its

original status by tuning the optical frequency. A simulated COTDR trace with a 130 MHz frequency shift exhibits the same shape as the original one, demonstrating that the trace distorted by an index change can be fully recovered by tuning the optical frequency. Generally speaking, the refractive index change is much smaller than the averaged index n_{ave}, thus the relative frequency shift required to restore the original trace is exactly equivalent to the relative change of the refractive index.

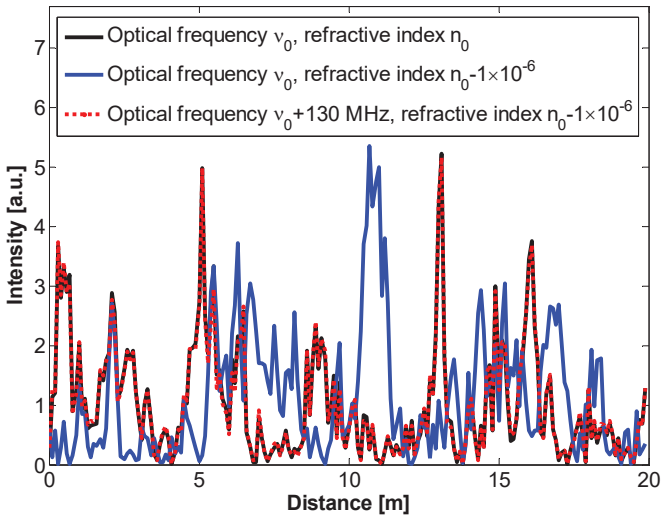

Figure 4-3. Simulation of the restorability of the coherent Rayleigh trace.

In the frequency domain, the restorability manifests itself as a spectral shift of the coherent Rayleigh trace. Because of the random nature of the interference, the amplitude of the backscattered light at a given position also varies randomly as a function of the optical frequency. The reflection spectrum at a sampling point is simulated by recording the intensity of the backscattered light over a 1 GHz frequency range. Speckle-like shapes are shown in Fig. 4-4a. The spectrum shifts due to the refractive index change, exactly like in a FBG sensor. However, because of its noise-like shape, quantifying the frequency shift of the COTDR spectrum is not simple. Usually, a special data process, i.e. cross-correlation, is required to solve this problem. Figure 4-4b shows the cross-correlation result of the spectra in Fig. 4-4a, the position of the correlation peak determines the frequency shift and its sign represents the shift direction.

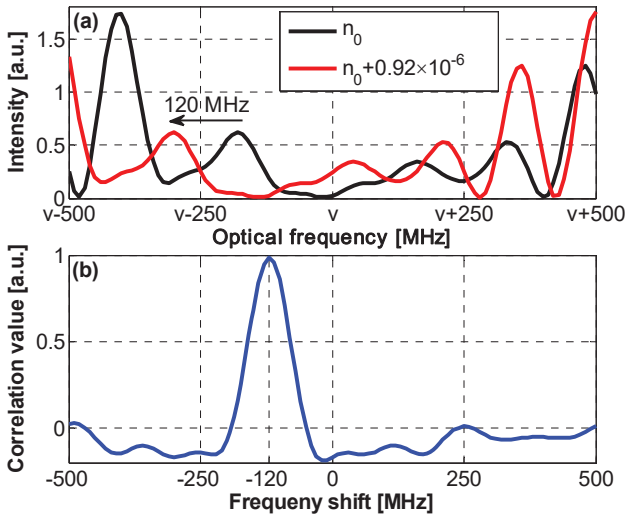

Figure 4-4. (a) Frequency spectrum of the coherent Rayleigh scattered light at a given position and (b) cross-correlation result of the simulated spectra.

According to the restorability, any shape change induced by environmental variations can be compensated by an optical frequency change. Based on this idea, a relationship can be built between the physical quantities that cause the trace change and the optical frequency detuning that fully restores the shape. Actually, the environmental perturbations have an impact on both the refractive index and the size of the scattering centres, but the simulation only considers the influence of the index change. However, it will be proved later that the influence of the scattering size variation can be neglected because its contribution is too small in temperature sensing.

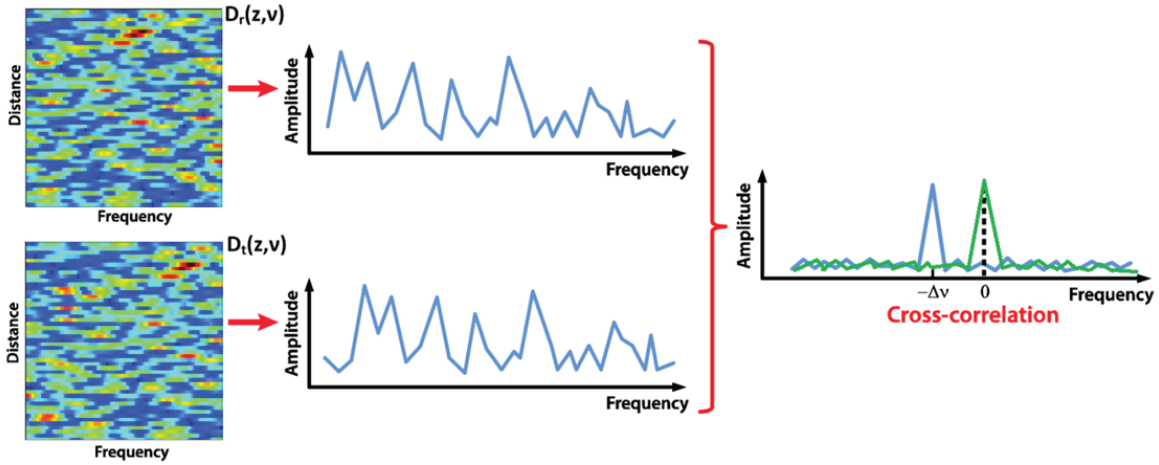

Figure 4-5. Principle of fibre sensing based on the coherent Rayleigh scattering.

Based on the analysis above, the working procedure of COTDR sensor is drawn in Fig. 4-5. At first, the Rayleigh traces $D_r(z,\nu)$ is obtained at different optical frequencies ν under a given condition as a reference. Then the traces $D_t(z,\nu)$ measured at time t are compared with the reference. The reflection spectra of both measurements at a given position show a random amplitude, as depicted in the middle of Fig. 4-5. The obtained Rayleigh spectrum should be identical to the reference if the measurement is taken under the exactly same condition. But it may shift due to the environmental perturbations and the shifted value is retrieved by cross-correlation. This process is shown on the right hand side of Fig. 4-5. The green line represents the result of the cross-correlation between two Rayleigh spectra under the exactly same condition, a correlated peak is observed at zero frequency. Two Rayleigh spectra obtained under different conditions lead to a frequency-shifted peak. Consequently, the environmental variations, such as temperature and strain, can be retrieved from this shift $\Delta\nu$ [43]. It has to be pointed out that this technique only provides a relative change of these quantities instead of an absolute value.

4.1.3 Sensitivity of a COTDR fibre sensor

In a COTDR system, the optical pulse is backscattered from the inhomogeneities and the reflected lights interfere with each other. And the analysis in section 4.1.1 demonstrates that the FBG works almost in the same way: light at the resonance wavelength is reflected due to the interference of the incident light reflected from the designed index variations in the fibre core. The reflection spectrum of a FBG can be well defined because the fibre index is intentionally modulated. However in the case of Rayleigh scattering, the refractive index fluctuation is introduced randomly during the fibre fabrication, so that the spectrum demonstrates random fluctuations. As a result, the interference process in a COTDR can be modelled as a weak FBG with random amplitude and pitch [90, 91], and a COTDR sensor is expected to be as sensitive as FBG sensors. Furthermore, the mature theory on the FBG sensing can be applied directly to the analysis of the DFS based on the coherent

Rayleigh scattering. In this section, the temperature sensitivity of a COTDR sensor is investigated under different thermal conditions based on the FBG sensing theory.

Equation 4-1 shows that the Bragg wavelength is determined by the effective index and the grating period, which are temperature dependent. Hence, the Bragg wavelength change due to temperature variations ΔT and applied strain ζ can be written as [85]:

$$\begin{aligned}\Delta\lambda_B &= \lambda_B\left\{\left(\gamma+\frac{1}{n_{eff}}\frac{dn_{eff}}{dT}\right)\Delta T+\left\{1-\frac{n^2}{2}\left[p_{12}-P_K\left(p_{11}+p_{12}\right)\right]\right\}\zeta\right\},\\ &= \lambda_B\cdot\left(Sen_{temp}\cdot\Delta T+Sen_{strain}\cdot\zeta\right)\end{aligned} \tag{4-2}$$

where P_K is the Poisson's coefficient, $p_{i,j}$ are Pockel's coefficients of the stress-optic tensor, γ is the thermal expansion coefficient of the fibre material, dn_{eff}/dT is the thermo-optic coefficient, $Sen_{temp} = \gamma+1/n_{eff}dn_{eff}/dT$ is the temperature sensitivity and Sen_{strain} is the strain sensitivity. The typical temperature and strain sensitivity of a FBG under ambient conditions are [85]:

$$\begin{aligned}\Delta\lambda_B/\lambda_B &= 6.67\times10^{-6}\ K^{-1}\\ \Delta\lambda_B/\lambda_B &= 0.78\times10^{-6}\ \mu\varepsilon^{-1}.\end{aligned} \tag{4-3}$$

The thermo-optic effect accounts for ~95% of the Bragg wavelength shift at room temperature, so that the contribution of the thermal expansion is minor [85].

	S_1	S_2	S_3	λ_1	λ_2	λ_3
T^0 term	1.10127	1.78752×10^{-5}	7.93552×10^{-1}	-8.90600×10^{-2}	2.97562×10^{-1}	9.34454
T^1 term	-4.94251×10^{-5}	4.76391×10^{-5}	-1.27815×10^{-3}	9.08730×10^{-6}	-8.59578×10^{-4}	-7.09788×10^{-3}
T^2 term	5.27414×10^{-7}	-4.49019×10^{-7}	1.84595×10^{-5}	-6.53638×10^{-8}	6.59069×10^{-6}	1.01968×10^{-4}
T^3 term	-1.59700×10^{-9}	1.44546×10^{-9}	-9.20275×10^{-8}	7.77072×10^{-11}	-1.09482×10^{-8}	5.07660×10^{-7}
T^4 term	1.75949×10^{-12}	-1.57223×10^{-12}	1.48829×10^{-10}	6.84605×10^{-14}	7.85145×10^{-13}	8.21348×10^{-10}

Table 4-1 Parameters in the Sellmeier model for Corning 7980 fused silica, valid in the temperature range from 30 K to 300 K and the wavelength range from 0.4 μm to 2.3 μm [92].

The thermo-optic coefficient is actually the derivative of the refractive index with respect to temperature, which is described by several empirical models. Among them, the Sellmeier model is a widely used method that expresses the refractive index of a common optical glass as [92]:

$$n^2\left(\lambda,T\right)-1=\sum_{i=1}^{3}\frac{S_i\left(T\right)\cdot\lambda^2}{\lambda^2-\lambda_i^2\left(T\right)}, \tag{4-4}$$

where T is the temperature, λ is the operating wavelength, S_i is the strength of the resonance features in the material, expressed as

$$S_i\left(T\right)=\sum_{j=0}^{4}S_{ij}\cdot T^j, \tag{4-5}$$

and λ_i is a factor related to S_i:

$$\lambda_i\left(T\right)=\sum_{j=0}^{4}\lambda_{ij}\cdot T^j. \tag{4-6}$$

The corresponding coefficients of the Sellmeier model for the optical fibre cannot be found, so the coefficients for Corning 7980 fused silica are used as listed in Table 4-1 [92], which is valid in the temperature range from 30 K to 300 K and the wavelength range from 0.4 μm to 2.3 μm.

Based on this data, the refractive index of fused silica at 1534 nm is plotted as a function of temperature in Fig. 4-6 and its slope represents the thermo-optic coefficient. The refractive index varies much less at low temperatures, so that a low thermo-optic coefficient is expected at cryogenic environment. This explains the reduced thermal sensitivity of a FBG sensor under cryogenic conditions.

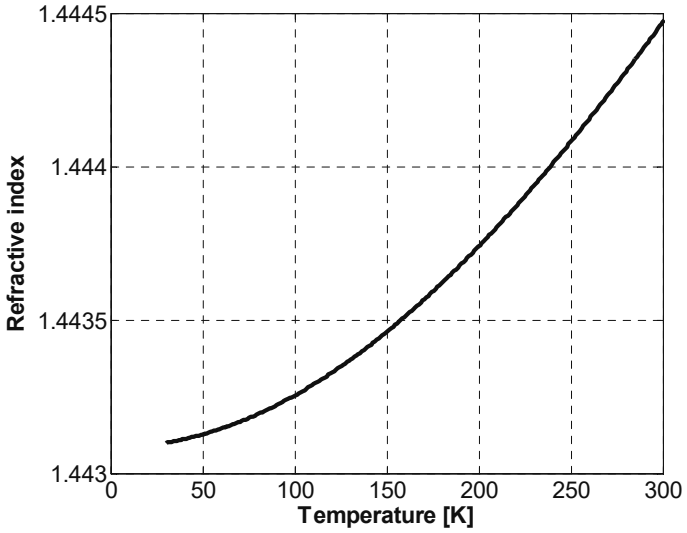

Figure 4-6. Refractive index of Corning 7980 fused silica at 1534 nm obtained by the Sellmeier model [92].

In another way, the thermo-optic coefficient of an optical fibre (SPECTRON photosil type C) is simply modelled as a quartic function of temperature at a Bragg wavelength of 1527 nm [93]:

$$dn_{eff}/dT = 6.82\times10^{-16}T^4 - 3.80\times10^{-13}T^3 + 4.83\times10^{-11}T^2 + 1.50\times10^{-8}T + 5.02\times10^{-6}. \quad (4\text{-}7)$$

This monotonic increasing function also shows that the coefficient becomes smaller under cryogenic conditions.

Although the thermal expansion contributes little to the Bragg wavelength shift at room temperature, it has more impact under cryogenic conditions because the thermo-optic coefficient decreases at low temperature, so it is taken into consideration in this theoretical analysis. The measurement result of the thermal expansion coefficient for fused silica SRM 739 is interpolated as [94]:

$$\gamma\times10^6 = a_\gamma\left(b_\gamma/T\right)^{c_\gamma}\cdot\exp\left(b_\gamma/T\right)\Big/\left[\exp\left(b_\gamma/T\right)+1\right]^2 + d_\gamma\left(e_\gamma/T\right)^2\cdot\exp\left(e_\gamma/T\right)\Big/\left[\exp\left(e_\gamma/T\right)-1\right]^2 \quad (4\text{-}8)$$

with the parameters a_γ = –4.22±0.07, b_γ = 35.5±0.8, c_γ = 0.335±0.015, d_γ = 1.253±0.022 and e_γ = 535±9.

The thermo-optic coefficient obtained by the two models and the thermal expansion coefficient retrieved by Eq. 4-8 are plotted in Fig. 4-7 as a function of temperature. And the Sellmeier model works only in the range down to 30 K so the coefficient below this temperature cannot be obtained. The results of both models on the thermo-optic coefficient show the same tendency that the coefficient decreases dramatically at cryogenic condition. But different values are observed between two models and this discrepancy becomes larger at low temperatures.

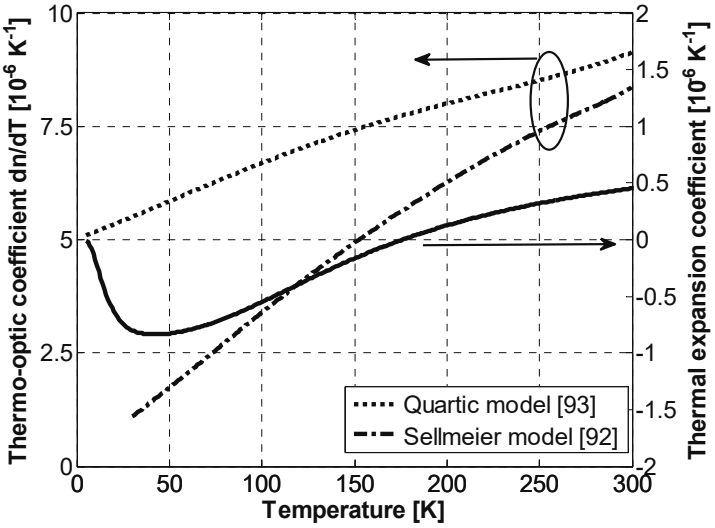

Figure 4-7. Thermo-optic coefficient and thermal expansion coefficient as function of temperature.

On the other hand, thermal expansion coefficient is about 20 times smaller than the thermo-optic coefficient obtained by the quartic model at room temperature, the same as stated in Ref. [85]. Thus it is reasonable to neglect the thermal expansion at room condition. This coefficient also decreases as the temperature reduces and it even becomes negative below ~ 175 K. But there exists a turning point at ~ 50 K, below which γ starts to increase. As the thermo-optic coefficient decreases at cryogenic temperature, the difference between it and the thermal expansion coefficient becomes smaller. For example, dn_{eff}/dT obtained by quartic model is just ~ 7 times as the expansion coefficient at 50 K. Consequently, the contribution of the thermal expansion can no longer be neglected at low temperature.

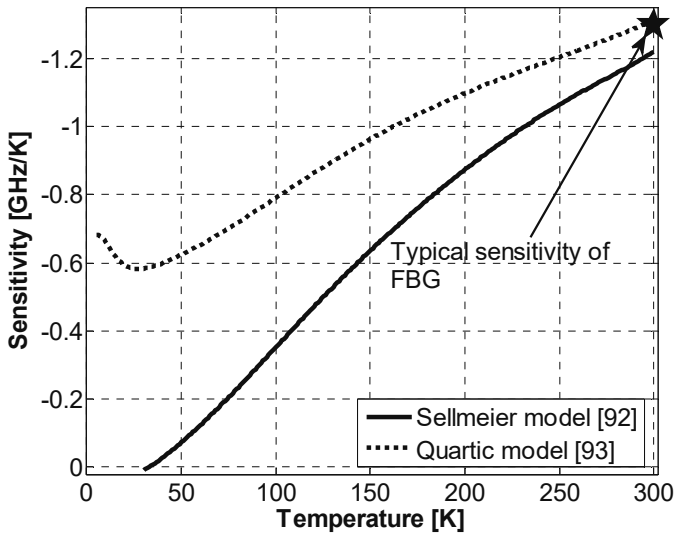

Figure 4-8. Calculated result of the thermal sensitivity at different temperature.

Inserting the thermo-optic coefficient and thermal expansion coefficient into Eq. 4-2, the temperature sensitivity can be calculated under different thermal conditions and the results are shown in Fig. 4-8. The obtained sensitivities become lower as the temperate decreases, following the same tendency of the thermo-optic coefficient that is the dominating factor. And the sensitivity based on the Sellmeier model decreases much more at low temperature; it becomes totally null at 30 K. But the sensitivity based on the quartic model starts to

increase below ~ 30 K due to the rise of the thermal expansion coefficient. At room temperature, the typical sensitivity of a FBG is 10.23 pm/K ≈ −1.28 GHz/K at 1534 nm based on Eq. 4-3, which is marked as a star in Fig. 4-8. And it is very close to the dotted line, validating the quartic model at room temperature. The temperature sensitivity obtained by the quartic model is higher because this model describes the thermal response of a highly GeO_2-doped fibre [95], and GeO_2 doping leads to a thermo-optic coefficient higher than fused silica, as presented by the experiment result in Ref. [88].

The sensitivity shows a dependence on the working temperature; as a result, the frequency shift over a large thermal range is expressed as

$$\Delta\nu = \int_{T_R}^{T_R+\Delta T} Sen_{temp}\left(\xi\right) d\xi\,, \tag{4-9}$$

where T_R is the reference temperature, and ΔT is the temperature change. The frequency shift of a COTDR sensor can be retrieved from Eq. 4-9 based on different models. The frequency shift from 300 K to cryogenic temperature is drawn in Fig. 4-9a. A quasi-parabolic curve is observed for the Sellmeier model, exhibiting a little frequency shift at low temperature because the optical fibre becomes inertial under this condition. But, the theoretical result obtained by the quartic model turns to be more linear over the whole temperature range, and the frequency shift is comparatively larger under the cryogenic condition. The discrepancy is explained by the different sensitivities obtained by different models, especially at low temperatures.

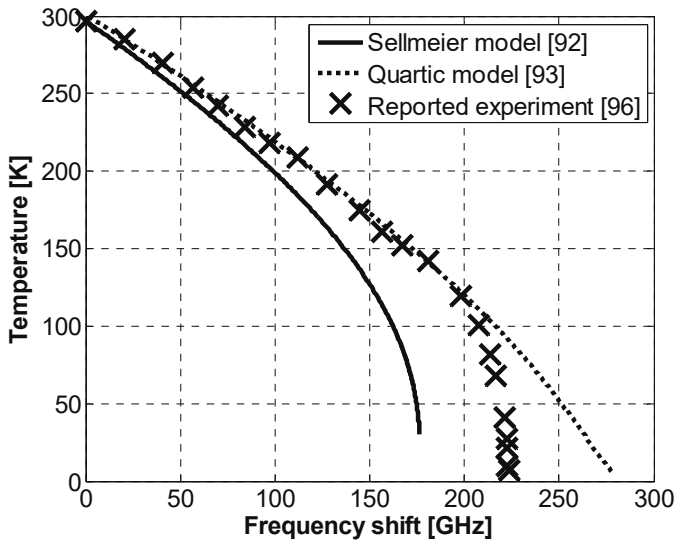

Figure 4-9. Comparison of the temperature induced frequency shift obtained by theory and reported result in the temperature range from 300 K to 4.2 K.

The theoretical analysis is compared with the experimental results obtained over the temperature range from 300 K to 4.2 K by the optical frequency domain reflectometry technique, which is based on the same working principle as a COTDR sensor [96]. In the reported experiment, a low bending-loss fibre with 16 μm thick polyamide coating is tested and the coating is so thin that it has little on the fibre sensing [96]. Experimental results show that the optical frequency linearly shifts with decreasing temperature until 100 K, then a quasi-parabolic relation is observed below 100 K and the frequency shift barely changes below 50 K. This is due to the changes of the thermo-optic coefficient and thermal expansion coefficients for fibre at the low temperatures as shown in Fig. 4-7; the same behaviour is observed in FBG sensors [88].

It is obvious that the theoretical result based on the quartic model matches well with the experiment from 300 K to 100 K. But this model seems to overestimate the sensitivity at low temperatures because the calculated frequency shift continues to grow as the temperature decreases. The discrepancy between the theory and experiment under 100 K is probably due to different dopants inside the fibres, and the inaccuracy of the thermo-optic coefficient at low temperatures.

On the other hand, the curve obtained by Sellmeier model is always below the experimental results, demonstrating this model underestimates the sensitivity. This is probably due to the parameters listed in Tab. 4-1 are used for fused silica instead of a doped fibre.

Theoretical analysis above shows that the COTDR possesses a high temperature sensitivity over a wide temperature range. For example, its temperature sensitivity under ambient conditions is over 1000 times higher than that of a Brillouin based sensor. Thus this technique can be applied to accurate measurements even under cryogenic conditions, such as liquid gas level monitoring and gas leakage detection.

4.1.4 Simulation of distributed temperature sensing based on COTDR

In Chapter 3 the 1D model is applied to simulate a coherent Rayleigh trace in the time and frequency domains with different optical pulse shapes. And it is able to demonstrate the restorability of the temporal Rayleigh trace as shown in Fig. 4-3. Thus this model has the potential to also simulate the COTDR sensing. Although the model considers only the refractive index change induced by the environmental perturbations, it is accurate enough to simulate the temperature sensing under ambient conditions, in which the thermo-optic effect plays the dominating role while the contribution of the thermal expansion is negligible.

A coherent Rayleigh scattering trace from a 1 km long optical fibre is simulated with a 10 ns incident rectangular pulse, corresponding to a 1 m spatial resolution, based on the theoretical model. Two sets of temporal traces are simulated within a 1 GHz optical frequency range with 10 MHz scanning step. Temperature variations of 0.3 K, –0.1 K and –0.2 K are introduced between the two measurements at the positions 910-912 m, 930-935 m and 964-965 m, respectively, based on a thermo-optic coefficient of 9.13×10^{-6} K^{-1} given by the quartic model in Fig. 4-7.

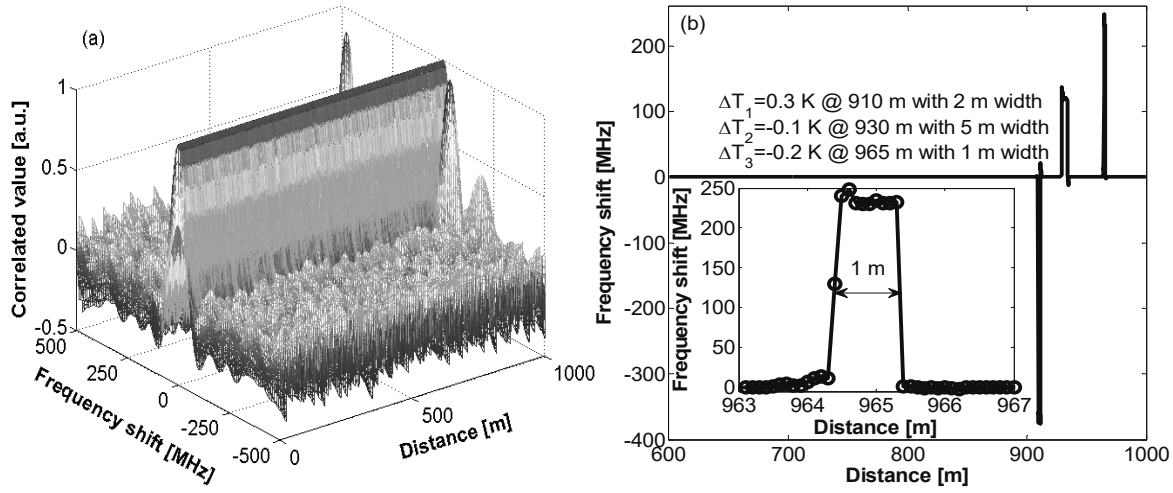

Figure 4-10. Simulation of temperature sensing. (a) Cross-correlation result, and (b) frequency shift as function of distance, inset: the temperature change at 964 m.

As drawn in Fig. 4-5, the two sets of Rayleigh traces are cross-correlated in the frequency domain at each fibre position, and the result is shown in Fig. 4-10a. Three shifted correlated peaks are observed at the hot spots due to the temperature variations and no frequency shift is observed for the peak in the rest of the fibre where no temperature change is introduced between the two measurements. The last peak is comparatively lower because the hot spot size is too small, the same as the spatial resolution. The frequency shift is plotted as a function of distance in Fig. 4-10b and the local temperature information can be retrieved from the frequency shift. Also the spatial resolution is confirmed to be 1 m in the inset of Fig. 4-10b.

The sensitivity of this simulation is intrinsically equal to the theoretical result and the sensitivity of a FBG sensor, as shown in Fig. 4-8. The standard deviation σ_v of the frequency shift at the hot spots is measured to be ~ 2.5 MHz. Thus the temperature resolution of the simulated COTDR sensor can be calculated:

$$\sigma_T = \sigma_v \Big/ \left| Sen_{temp} \right| = 2.5/1310 \approx 0.002 \ \ K \ . \tag{4-10}$$

using the temperature sensitivity $Sen_{\text{temp}} = -1.31$ GHz/K shown in Fig. 4-8.The obtained resolution reaches 2 mK, which is two orders of magnitude better than the DFS based on Raman and Brillouin scatterings, demonstrating again that the COTDR sensing is applicable for highly precise measurements.

4.1.5 Conclusion

In section 4.1, the working principle of a COTDR sensor is shown to be identical to a FBG sensor. Its temperature sensitivity is calculated under different thermal conditions based on two models. A high sensitivity is expected in the temperature range from ambient to cryogenic conditions, and this result is confirmed by the reported experiment using OFDR sensing.

The theoretical model on the COTDR trace demonstrates its ability to simulate the restorability and temperature sensing. Consequently, this model has the potential to evaluate the influence of different parameters, such as spatial resolution and averaging time, on the sensing performance of a COTDR system.

4.2 Experimental validation

The analysis in the previous section shows a high sensitivity and a small measurand resolution of the DFS based on the coherent Rayleigh scattering. The performance of this sensor is experimentally validated and characterised under different thermal conditions in this section.

4.2.1 Laser frequency stabilisation

Due to the high sensitivity of the COTDR sensor, about −1.3 GHz/K at ambient temperature, the optical frequency of its light source must be very stable when an accurate measurement is required. According to the analysis above, a laser frequency drift of 13 MHz will degrade the temperature resolution from 2 mK to 10 mK. Unfortunately, the optical frequency stability of standard commercially-available semiconductor lasers is usually insufficient to meet this requirement. Thus, an extra system using a frequency standard is needed to lock the laser frequency.

The gas absorption spectrum is widely used as a frequency standard due to its inherit stability and immunity to environmental perturbations. In a stabilisation system based on gas spectroscopy, the laser frequency drift is

converted into an optical power change after the incident light passes through an absorption line. Then the laser driving current is adjusted based on the optical power change to lock the frequency on an absorption line [97]. A photonic crystal fibre filled with such a gas is a good candidate in a fibre sensing system as it is compatible with the all-fibre optical structure and avoids alignment [98].

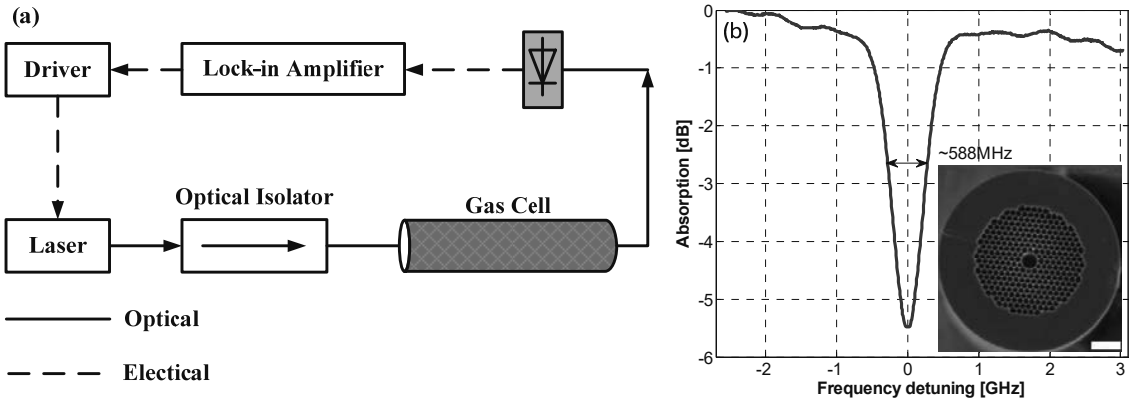

Figure 4-11. Laser frequency stabilisation. (a) Implemented scheme and (b) absorption spectrum of acetylene gas used for the locking system, inset: cross-section of the used hollow-core photonic crystal fibre.

The frequency stabilisation system is shown in Fig. 4-11a [98]. The objective here is to lock the laser frequency on an absorption line of acetylene in a gas cell with a filling pressure of 77 mbar [98], so that whenever the laser frequency drifts, power variations are monitored in order to adjust the laser driving current to compensate the frequency shift. In this case, the gas cell is a hollow-core photonic crystal fibre filled with acetylene gas whose cross-section is shown in the inset of Fig. 4-11b [98]. The driving current is tuned to position the laser wavelength within the absorption line P15 [99], which is shown in Figure 4-11b. Additionally, a sin wave from the lock-in amplifier is applied to the driving current of the laser, so that the continuous wave coming out of the laser is slightly modulated at a given frequency. An optical isolator is placed at the output of the laser to avoid any laser coherence degradation due to the back-reflections. The CW light passes through the gas cell, gets attenuated because of the gas absorption and finally enters a photodetector. The laser frequency drift will change the optical power at the output of the gas cell. The lock-in amplifier detects this power change by demodulating the signal from the photodetector at the sin wave oscillating frequency, and provides injection current corrections to the laser driver to compensate the frequency drift from the centre of the absorption line.

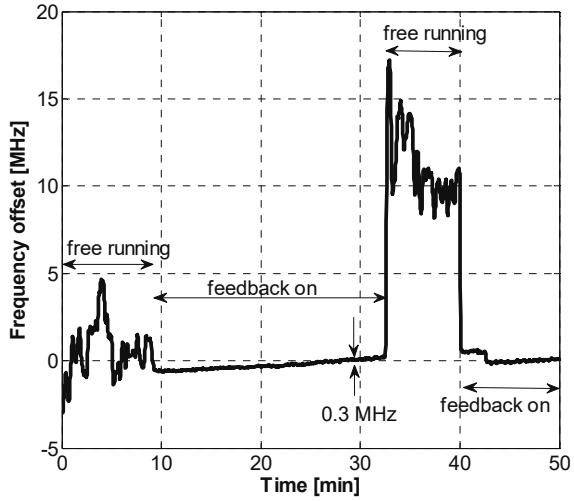

Figure 4-12. Experimental demonstration of the laser frequency stabilisation scheme.

The effect of this stabilisation system is shown in Fig. 4-12. The laser frequency is immediately locked to the centre of the absorption line once the feedback loop is on. And the frequency fluctuations are reduced by a factor 30 with the implemented locking system. Using this servo control, a COTDR sensor could provide milli-Kelvin resolution even after a long working time.

4.2.2 Experimental setup

For a very accurate sensing, the frequency of the optical pulse in a COTDR system should not only be very stable but also be precisely controlled. And the precise control is usually realised by employing the sideband generated through a RF modulation [100]. The experimental setup is shown in Fig. 4-13. The CW light from a laser passes through an optical splitter and is divided into two paths. The upper path is connected to the servo loop to stabilise the laser frequency at 195.41922 THz. In the lower path, a SOA driven by an electrical pulse generator is employed to convert the CW light into optical pulses with high extinction ratio. The optical frequency sweeping is realised using an EOM driven by a microwave source. A tunable FBG (~10 GHz bandwidth) is employed to choose one of the two sidebands generated by the EOM. Then, the optical pulses are boosted by an EDFA and a band pass filter (~100 GHz bandwidth) is used to suppress the ASE noise from the EDFA. The optical pulses enter the FUT through an optical circulator and the Rayleigh backscattered light is guided to a 125 MHz photodetector. The COTDR traces are acquired and later processed by a computer.

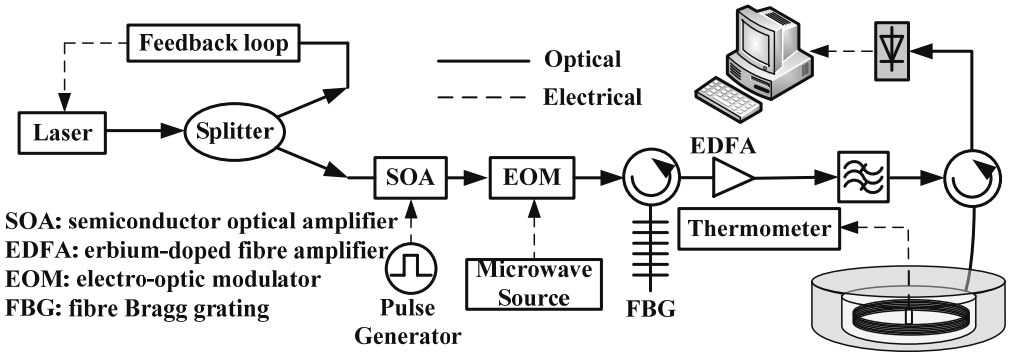

Figure 4-13. Implemented COTDR system for distributed temperature sensing.

For each temperature measurement, the Rayleigh backscattered light is obtained within an optical frequency range of 400 MHz with 10 MHz scanning step. Smaller steps could actually result in a better measurand resolution. However, an ultimate limit is determined by the frequency stability of the light source. The pulse width is set as 15 ns, corresponding to 1.5 m spatial resolution. A 125 MHz receiver is used to collect the backscattered light since such a bandwidth has been proven large enough in Chapter 3. To enhance the SNR, the COTDR traces at each frequency are averaged 1000 times, leading to a total measurement time of 40 seconds.

The sensing fibre is totally 23 m long, composed of a 14-metre standard SMF coated with acrylate and a 9-metre special fibre with ORMOCER® coating [101] which can stabilise the mechanical and thermal properties of the fibre [102]. Two different fibres can be tested simultaneously and details about the two fibres can be found in the appendix. They are loosely coiled inside a copper box with a diameter of 9 cm in order to avoid temperate gradients along the FUT, as shown in Fig. 4-14. A Pt-1000 thermal probe is placed in the middle of the metallic box to monitor and calibrate the temperature. According to the data sheet, the tolerance value of this Pt-1000 is ± 0.15 K [103] and it is assumed to be much more accurate to measure the temperature change. For long distance measurements, the FUT is attached to a fibre spool of several kilometres long SMF.

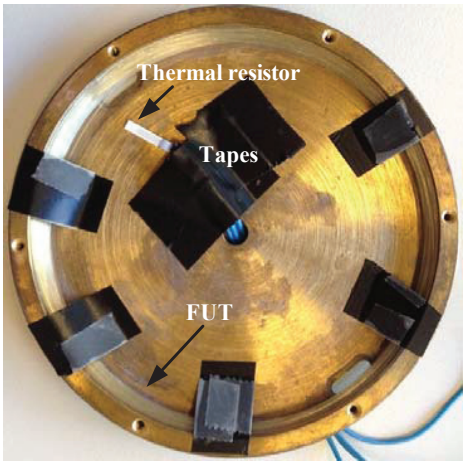

Figure 4-14. Copper box used to provide a stable and uniform temperature distribution along the sensing fibre. A thermal resistor is placed inside to monitor the fibre temperature required in the characterisation.

The copper box is placed in a thermal bath filled with water for measurements at room temperature (~ 300 K). Due to its large specific heat capacity, the water acts as a thermal buffer and provides a uniform temperature distribution along the entire sensing fibre. In this case, the impacts of temperature gradients and potential thermal perturbations can be highly suppressed. A variation below 0.1 K is observed at ambient conditions by the thermal probe within a monitoring period of over 2 hours, demonstrating a high thermal stability of this system. The water temperature could be controlled with an accuracy of ~ 0.1 K by the thermal bath. Even smaller temperature change could be achieved using the slow thermal exchange between water and ambient environment.

Figure 4-15. Container for cryogenic measurement when the copper box is (a) immersed in and (b) hung above the liquid Nitrogen.

For cryogenic temperature measurements, the copper box is placed in a container filled with liquid Nitrogen, as shown in Fig. 4-15. A direct contact of the box with the liquid allows a precise and stable temperature measurement at ~ 77 K, as shown in Fig. 4-15a. Large temperature change is realised by adjusting the level of the box above the Nitrogen, presented by Fig. 4-15b. A second container can be used as a complementary thermal buffer to partially mitigate the cooling effect of the liquid. Thus the FUT could be stably exposed to

temperatures up to 270 K. A 10 MΩ resistor is dipped in the Nitrogen and connected to an electrical power supply. Therefore, small temperature changes are possible by tuning the voltage of the supply, which governs the evaporation rate of the liquid [104].

4.2.3 Experiment result at room temperature

As presented in the above analysis, the restorability of the coherent Rayleigh trace is the working principle of a COTDR sensor. An experiment is carried out to demonstrate this phenomenon in a short piece of standard SMF and the result is shown in Fig. 4-16. It is obvious that the original backscattered Rayleigh trace obtained at a given condition is changed due to a small temperature variation of 26 mK. And the changed shape is almost fully recovered by slight detuning the laser frequency by 30 MHz. There exists a small difference between the restored trace and the original trace, which is due to the large frequency scanning step. The distorted trace can be fully recovered by a finer control of the optical frequency. And this experiment also validates the high temperature sensitivity of a COTDR sensor.

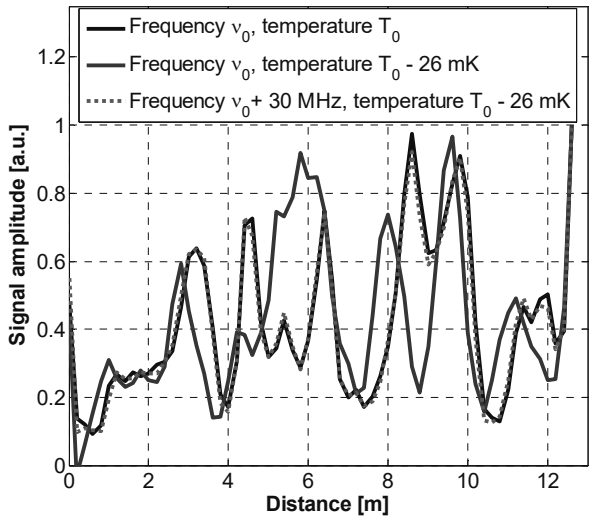

Figure 4-16. Restorability of the coherent Rayleigh trace obtained experimentally.

To realise temperature sensing, both types of fibres experience temperature changes in the thermal bath. The spectra of two successive measurement results are cross-correlated along the sensing fibre in order to obtain the frequency shift. And the correlation result is presented in Fig. 4-17, a peak exists at the frequency where the trace shape of both measurements is most similar to each other. The inset shows the cross-correlation spectrum at a given position with no frequency shift, and the real location of the peak is determined by a quadratic fitting [105]. Thus the problem about the large scanning step in the restorability experiment can be partially solved and the peak position is plotted as a solid line along the fibre in Fig. 4-17. Actually, the width of the correlation peak is related to the measurand resolution [105] and is dependent on the incident pulse width [106].

Figure 4-17 again proves the high sensitivity of a COTDR sensor at room temperature, as a small temperature change of ~ 26 mK induces an average frequency shift of 32 MHz in the standard fibre and 42 MHz in the special fibre. The standard deviation obtained along the fibres is between 2 and 3 MHz, which corresponds to a temperature precision around 2 mK under ambient conditions and is very close to the simulated value. It must be pointed out that the special fibre is more sensitive at room temperature due to the extra thermally induced strain by the ORMOCER® coating [102].

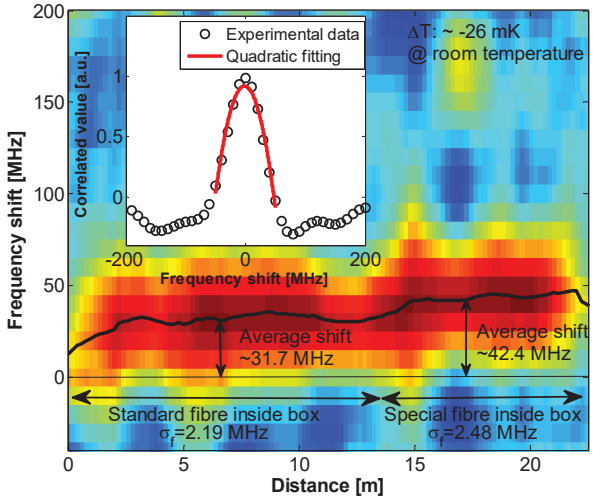

Figure 4-17. Cross-correlation between two successive measurements with a small temperature change, inset: quadratic fitting of the correlated peak.

Furthermore, it is important to mention that the standard deviation of the measurement shown in Fig. 4-17 is mainly given by the noise characteristics of the system and the frequency step used during the scanning. As a result, it is independent on the working temperature, as also confirmed by the measurements that will be shown later at cryogenic conditions.

As shown in Figs. 4-16 and Fig. 4-17, the sensitivity of a coherent Rayleigh sensing system is over 1000 times higher than the Brillouin based DSF. This is good for a highly precise measurement but the measurand range is considerably restricted due to the limited frequency sweeping range, because the frequency shift $\Delta\nu$ induced by a large temperature change ΔT might be beyond the scanning range of the sensor. Expanding the frequency scanning range is a feasible method to solve this problem. But it leads to substantial increases of the measurement time and the cost. A simple solution is to repeat the measurement continuously and obtain the frequency shift $\Delta\nu_i$ of two successive measurements $R_{t_{i-1}}(z,\nu)$ and $R_{t_i}(z,\nu)$ in a comparatively smaller scanning range. So every obtained trace acts as the reference for the following trace. In this way, the equivalent frequency shift of X measurements can be expressed as $\Delta\nu = \sum_{i=1}^{X} \Delta\nu_i$. Hence, a large measurand change can be retrieved using only incremental measurements with a small sweeping range. However, this method will accumulate errors from each measurement.

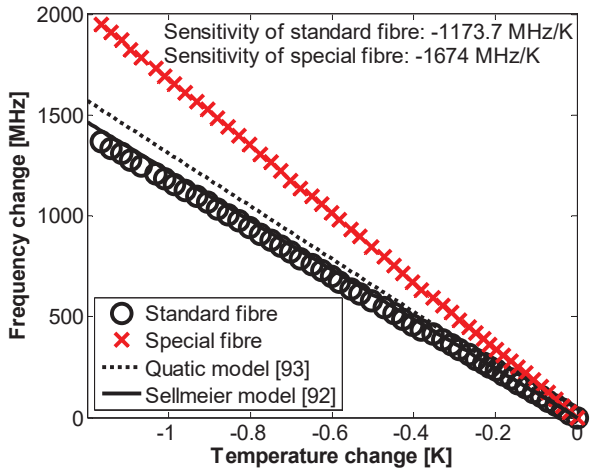

Figure 4-18. Frequency shift versus temperature change for different fibres at room temperature.

The obtained frequency shift is plotted as a function of temperature changes in Fig. 4-18 for both kinds of fibres and the slopes represent the corresponding sensitivities. The measurand range is greatly expanded by cross-correlating successively obtained Rayleigh traces, because a frequency shift up to 2000 MHz is evaluated while the scanning range is only 400 MHz. The sensitivity measured in the standard fibre is ~ –1.17 GHz/K that is very close to the value given by the Sellmeier model. However, the ORMOCER® coated fibre demonstrates a higher sensitivity than the calculated value. And this difference is caused by the extra strain induced by the thermal expansion of the coating.

It needs to be pointed out that the sensitivity expressed by Eqs. 4-2 and 4-3 are valid only for bare fibres. In practice, the optical fibre is usually coated for protection. A simple longitudinal section of a coated fibre is shown in Fig. 4-19, d representing the thickness of the coating, Y and γ representing Young's modulus and thermal expansion coefficient for fibre and coating c, respectively. The thermal expansion of the coating induced by temperature change will cause a strain ζ' in the fibre core, which can be expressed as [107]:

$$\zeta'(\Delta T) = \left(\gamma_c - \gamma_{fibre}\right)\frac{C \cdot Y_c}{C \cdot Y_c + Y_{fibre}}\Delta T \,, \tag{4-11}$$

where C is the ratio between the cross-sectional area of the coating and the fibre:

$$C = \left[\left(d+b\right)^2 - b^2\right] \Big/ b^2 \,. \tag{4-12}$$

As a result, the temperature sensitivity of a coated fibre is expressed as

$$\Delta\lambda_B / \lambda_B = Sen_{temp} \cdot \Delta T + Sen_{strain} \cdot \zeta'(\Delta T) \,. \tag{4-13}$$

Thus the thermal response of a coated fibre is related to the coating properties, i.e. its thickness, its Young's modulus and its thermal expansion coefficient.

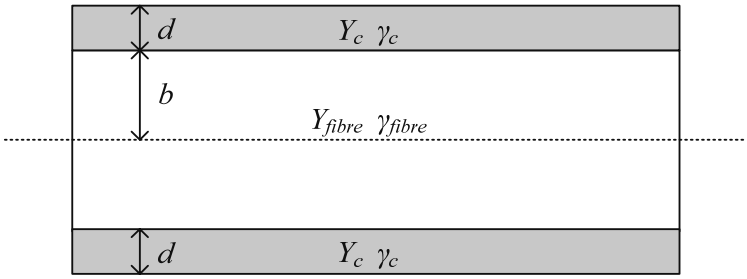

Figure 4-19. Longitudinal section of a coated fibre.

For a standard SMF, the Young's modulus of the primary coating is 10 MPa at room temperature [108], much smaller than the value of silica (70 GPa [109]), which cannot be compensated by the large cross-section area of the coating. Hence, the thermally induced strain ζ' is very small, so that its influence on the frequency shift can be neglected. Therefore, the measured sensitivity of the standard fibre is very close to the calculated value for the bare fibre.

On the other hand, the ORMOCER® coating of the special fibre is 35 μm thick with a Young's modulus of ~ 1.5 GPa at room temperature [110]. In this case, the thermally induced strain can no longer be neglected, and it

has been reported that the ORMOCER® coating increases the temperature sensitivity of a FBG by 2.4 pm/K at λ_B = 852 nm [102]. According to this sensitivity increase, the thermal expansion coefficient of the ORMOCER® coating is obtained as ~ 1.23×10^{-4} K^{-1} based on Eqs. 4-4, 4-5 and 4-6. Finally, the temperature sensitivity is calculated to be increased by ~ 0.54 GHz/K due to the ORMOCER® coating. And the measured sensitivity enhancement (0.5 GHz/K) is very close to the predicted result.

The measured frequency shift is converted into a temperature change using the obtained sensitivity. The result measured by the COTDR sensor is compared with the temperature acquired by the Pt-1000 probe in Fig. 4-20. The robustness of the coherent Rayleigh based DFS is confirmed in 110 min long thermal cycles. Figure 4-20 shows a good agreement in the first hour between the results obtained by the fibre sensor and by the thermal probe, and then small discrepancies are observed. Probably, the thermometer is moved by the water in the thermal bath, so that the thermal gradient between the sensing fibre and the Pt-1000 has been changed, resulting in the small differences of the measured temperature.

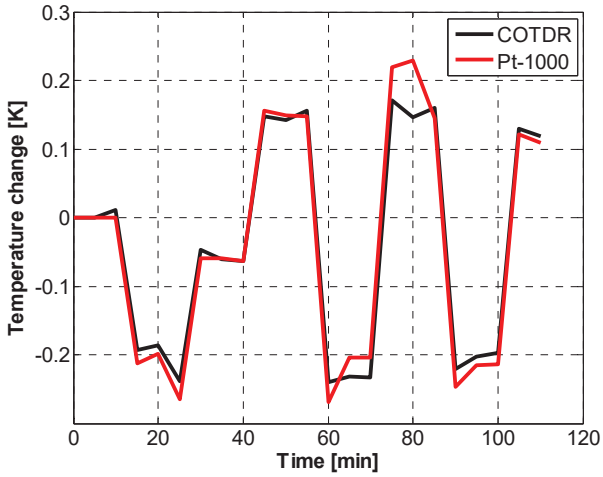

Figure 4-20. Comparison of the temperature change measured by COTDR and Pt-1000 in thermal cycles.

The good resolution obtained within a short sensing distance is just indicative because this value is highly dependent on the signal-to-noise ratio, which becomes worse in the case of a longer sensing distance. To validate the performance in a comparatively longer range, the measurement is repeated. In this case, the FUT is connected to the end of a 2 km standard SMF spool that is placed in the open air.

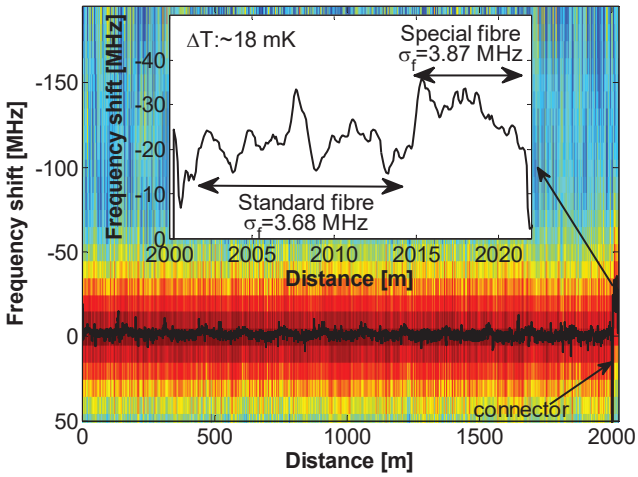

Figure 4-21. Cross-correlation result for 2 km standard SMF, inset: enlarged view of the hot spot.

The obtained frequency shift along the fibre is presented in Fig. 4-21. For most part of the fibre, the correlated peak demonstrates no frequency shift but some small deviations are observed due to the thermal perturbations. Actually, the peak frequency varies periodically along the fibre and it is may be induced by a thermal gradient in the surrounding air. This periodicity demonstrates again the high sensitivity of the COTDR sensor. In addition, a clear frequency shift is observed at the sensing part due to a temperature change inside the thermal bath. The standard deviation is below 4 MHz for both fibres, corresponding to a resolution of ~ 2.7 mK. So a precise measurement can be realised by a COTDR sensor over a 2 km sensing distance.

The sensing distance can be improved with the help of a pre-amplifier to level up the backscattered light. The same amplifying scheme like in Chapter 3 is used here for long distance sensing. The pulse width is set at 20 ns, equivalent to a 2 m spatial resolution. Two sets of successively measured Rayleigh traces from a 50 km standard SMF are cross-correlated and the result is shown in Fig. 4-21. At the end of the fibre, the COTDR traces become less correlated and the obtained frequency shift oscillates faster, which can be explained by the weak Rayleigh signal at the far end. Figure 4-21 also exhibits a quasi-periodic fluctuation of the peak frequency, and it may be induced by the same reason: temperature fluctuations along the fibre spool.

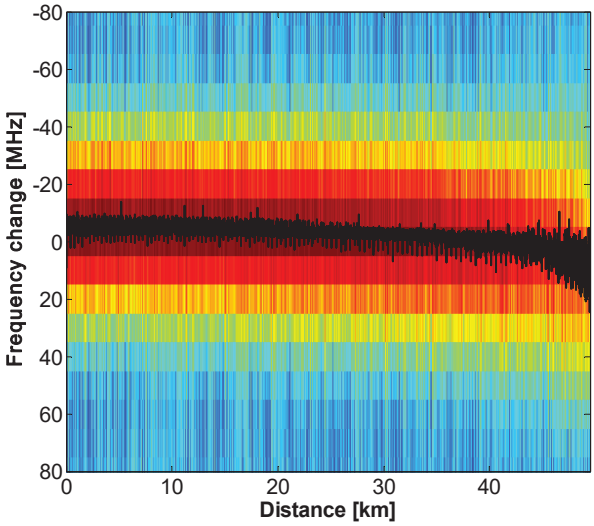

Figure 4-22. Cross-correlation result for 50 km standard SMF with pre-amplification.

It takes more time to accomplish a longer distance sensing, so the environmental perturbations between the successive measurements should be taken into consideration. As a result, most of the obtained correlated peaks demonstrate a small frequency shift even though no environmental variations are introduced deliberately between the two measurements. As shown in Fig. 4-22, the peaks tend to shift towards the negative direction at the beginning of the fibre and it turns to the positive side at the far end. This shift needs further study, and it may be caused by the small difference of temperature changes experienced by the inner and outer coiling layers of the spool.

4.2.4 Experimental results at cryogenic temperatures

With the help of liquid Nitrogen, the thermal response of a COTDR sensor is tested under cryogenic conditions. By placing the copper box just above the level of the liquid, the fibre temperature is decreased down to about 80 K. Small variations in the fibre temperature are realised by the thermal exchange between the liquid and the ambient air. Figures 4-23a and 4-23b show the measurement results obtained during cooling and warming up

processes, respectively. Comparatively lower sensitivity is observed for both types of fibres in both processes. However, the reduced sensitivity is still hundreds times higher than that of a Brillouin sensor. And the sensitivity obtained by the experiment is lower than the theoretical prediction shown in Fig. 4-8. It needs to be pointed out that the results shown in Fig. 4-23b is not as reliable as Fig. 4-23a because of the small temperature change (< 0.06 K).

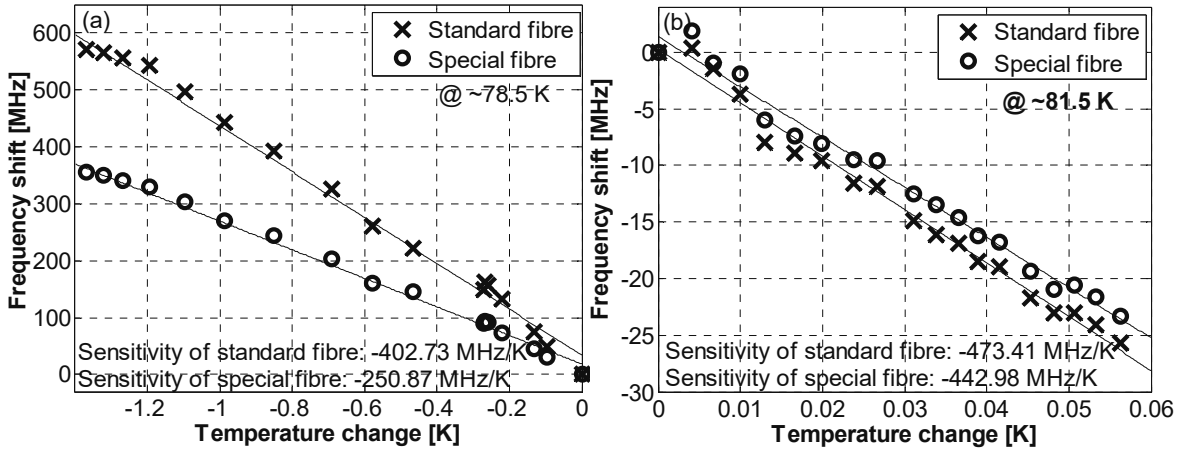

Figure 4-23. Measured frequency variation when temperature changes around 80 K with (a) negative and (b) positive steps.

The temperature sensitivity of the coherent Rayleigh-based sensor is also measured in the temperate range from 77 K and 300 K. In this case, the copper box needs to be placed inside another container, which acts as a complementary thermal buffer. This container partially mitigates the cooling effect of liquid Nitrogen, so that the fibres could be stably exposed to temperatures up to 300 K. It takes a long time for the fibre to reach the targeted temperature. Actually, changing the temperature with stable and controllable steps is the most challenging process in the entire experiment. Since the measurement requires about 40 seconds to be completed, the temperature should vary sufficiently slowly for the sensor to accomplish the measurement. Due to the slow temperature change, delays of several tens of seconds have been inserted between two successive scanning processes to achieve a large temperature difference between the measurements. Since the sensitivity becomes lower in a cryogenic environment, the same laser frequency drifting will cause a larger measurement error.

Figure 4-24 shows the measured frequency shifts of both fibres around four different temperature conditions, ranging from 100 K to 250 K. All the frequency shift changes linearly with the temperature and high sensitivities are obtained in the different cases.

The relation between sensitivity and temperature for both FUTs during cooling and heating processes is summarised in Fig. 4-25. The shaded region is depicted to represent the area that covers most of the measured points just for visibility. Generally speaking, the experimental results confirm the high temperature sensitivity of the COTDR sensor even at cryogenic environment. However, the behaviour of the temperature sensitivity for the standard fibre is different from the theoretical analysis. As shown in Fig. 4-8, the thermal response becomes weaker when the working temperature decreases. On the contrary, the temperature sensitivity of the standard acrylate-coated fibre keeps rising and reaches the highest value at around 220 K.

The non-conventional behaviour of the standard fibre can be explained by the thermally induced strain in the coating, as discussed in the previous section. Although the thermal expansion of the coating has little influence on the temperature sensitivity of the standard fibre at room temperature, it has to be taken under

consideration because the polymer coating exhibits glassy behaviour at low temperature [24]. The Young's modulus of the primary coating grows up to ~ 1 GPa as the temperature decreases from room temperature to the glass transition temperature (~ 220 K) and becomes less temperature dependent below 220 K [24]. During this process, the thermally induced strain becomes larger which not only compensates the influence of the thermo-optic coefficient reduction but also contributes more to the frequency shift, so the temperature sensitivity is enhanced from 300 K to 220 K. However, the sensitivity decreases gradually below 220 K because the extra strain turns to be stable in this temperature range while the thermo-optic coefficient continues to decline.

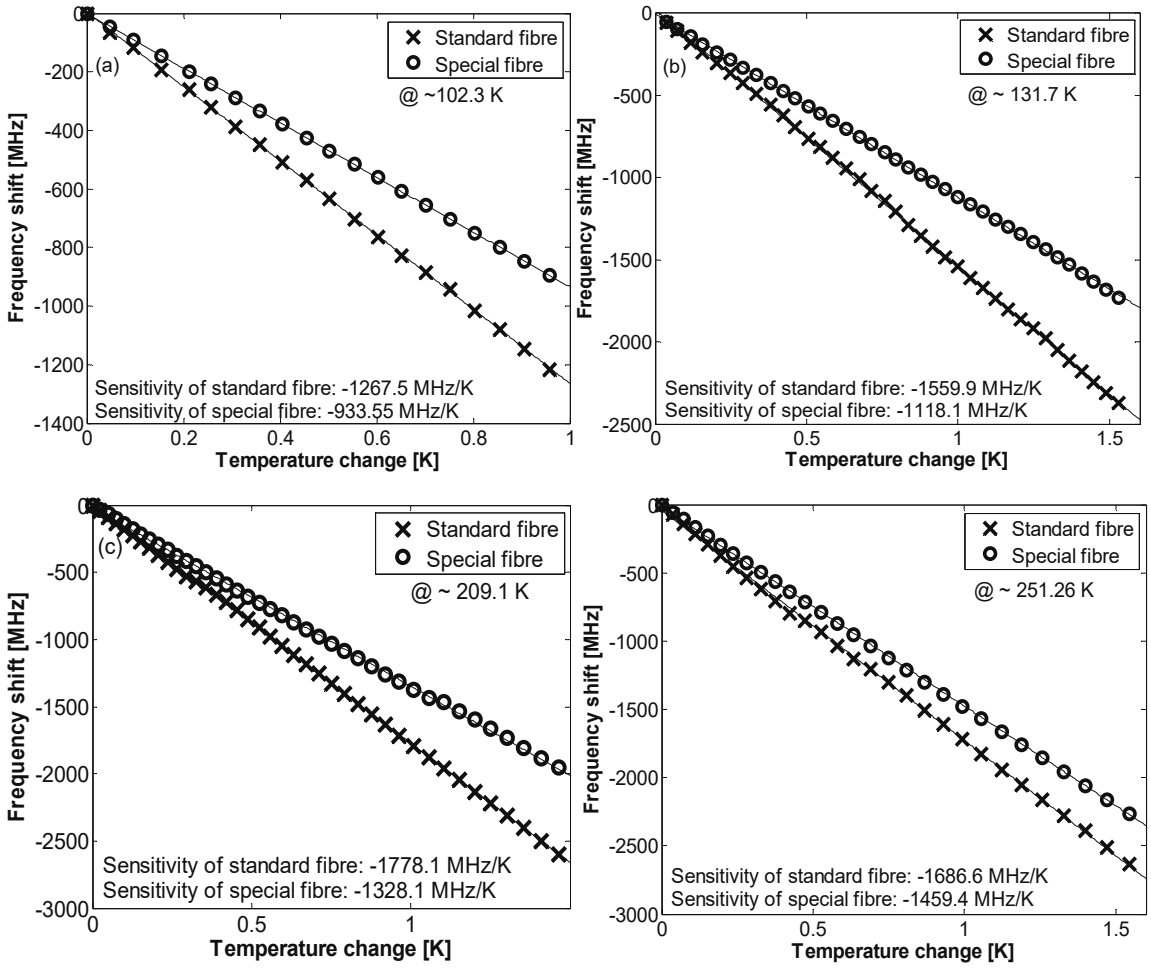

Figure 4-24. Frequency shift measured for both kinds of fibres when the fibre temperature is increased at around (a) 102 K, (b) 133 K, (c) 210 K and (d) 250 K.

Comparatively, the sensitivity of the specially coated fibre reduces almost monotonically as the temperature decreases, in agreement with the theory in Section 4.1. This is probably due to the less temperature dependence of Young's modulus of the ORMOCER® coating [111]. The small deviations can be explained by the thermal gradient between the PT-1000 probe and the fibre and measurement errors of the thermal probe.

In addition, Fig. 4-25 demonstrates clear discrepancies between positive and negative thermal gradients, especially in the standard fibre. This kind of thermal hysteresis has been observed at ambient condition [112] and is explained by the thermal-mechanical feature changes of the optical fibre during the thermal cycling. But currently there is no investigation about this phenomenon in COTDR sensing, so further research on the thermal and mechanical change is needed.

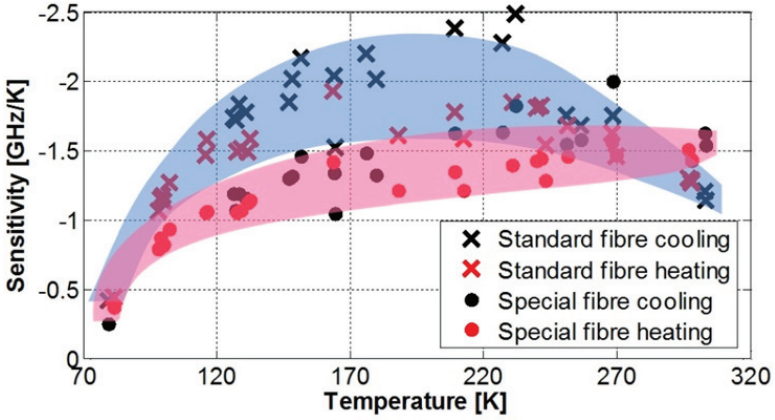

Figure 4-25. Temperature sensitivity of both fibres obtained by the implemented COTDR sensor at different temperatures.

The stable sensing performance of the special fibre provides the opportunity to compare the experimental results with the theoretical analysis on the sensitivity shown in Fig. 4-8. Since the ORMOCER® coating introduces extra strain that contributes to the frequency shift, the sensitivity of the special fibre is enhanced by ~ 0.54 GHz/K at room temperature, according to the analysis above. It is assumed the thermal and mechanic behaviour of the ORMOCER® coating is temperature independent, so that sensitivity increase is a constant over the testing temperature range. Thus the sum of the theoretical results in Fig. 4-8 and this enhancement increase represents the temperature sensitivity of this special fibre, and they are compared with the experimental results in Fig. 4-26. The calculated results based on quartic and Sellmeier models are very close to the measured results, but a large discrepancy is observed at 77 K, which can be explained by the change of the thermally induced strain. However, it must be pointed out that the theoretical curves here only provide the tendency; a precise investigation can only be made by using the thermal and mechanical properties of the ORMOCER® coating at different temperature.

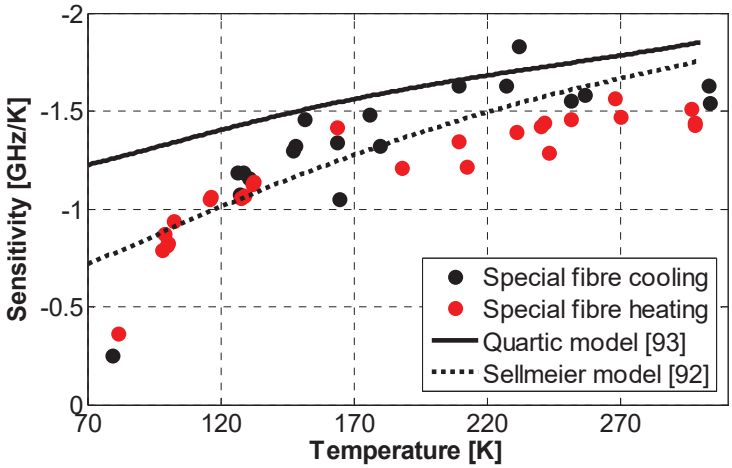

Figure 4-26. Comparison of the sensitivities obtained by the experiment and the theory for the ORMOCER® coated fibre.

The temperature resolution can be easily retrieved from the measured frequency accuracy σ_ν in Fig. 4-17 and the temperature sensitivity reported in Fig. 4-25. The calculated results are presented in Fig. 4-27, for both types of fibres in the heating and cooling processes over a temperature range from 77 K to 300 K. The temperature resolution is around 2 mK between 100 K and 300 K, the same as the simulation result, and even the worst resolution is still below 10 mK around liquid Nitrogen temperature. Hence, the sensor based on coherent Rayleigh scattering is able to provide precise temperature measurement under cryogenic conditions.

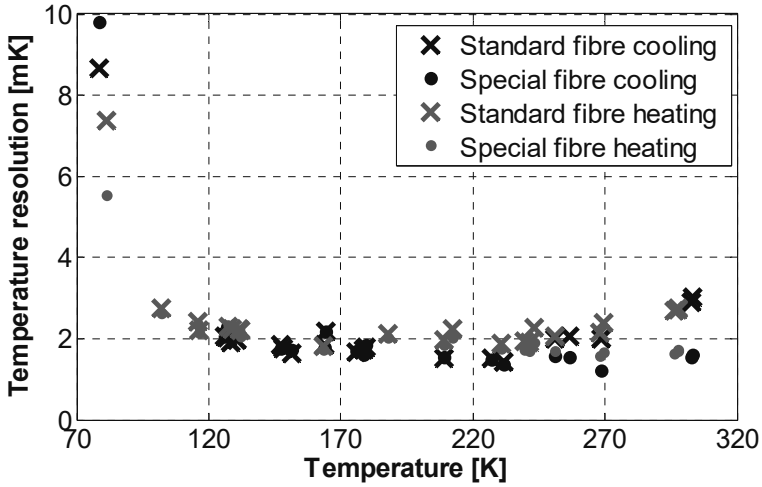

Figure 4-27. Temperature resolution obtained by the implemented COTDR sensor in the thermal cycle.

4.2.5 Conclusion

The thermal behaviour of a coherent Rayleigh scattering based DFS with an frequency stabilisation servo system is characterised in a temperature range from 77 K to 300 K. Experimental results validate the theoretical analysis in section 4.1 and confirm the high sensitivity even at cryogenic condition. A milli-Kelvin resolution is achieved in a COTDR sensing system over a few km sensing distance with a spatial resolution less than 2 m. Actually, fibre sensing based on coherent Rayleigh scattering can be realised by OTDR and OFDR, and there is a trade-off between the measurand resolution and spatial resolution [105]. For instance a temperature resolution of 0.34 K is reported using the OFDR technique with 48 cm spatial resolution at 77 K [90].

Furthermore, the thermal expansion of the coating is proved to have large influence on the thermal response of the COTDR sensor. It is observed that a thicker coating enhances the sensitivity at room temperature and a fibre with standard acrylate coating reaches highest sensitivity at 220 K due to the glassy behaviour of the primary coating. However, the measurement results of the standard fibre exhibit a clear thermal hysteresis during heating and cooling processes, which needs further analysis.

4.3 Fibre heating methods

The DFS based on the coherent Rayleigh scattering demonstrates a high sensitivity because of the interference process. But the sensitivity and the measurand resolution turn out to be significantly reduced at temperature below 100-120 K due to the low thermo-optic coefficient of silica. Raising the optical fibre temperature is a possible solution to enhance the sensitivity of the COTDR sensor at cryogenic working environment, because the thermo-optic coefficient increases due to the higher fibre temperature. The heated fibre may have impact on the surrounding temperature, however, the thermal exchange between the fibre and the environment could actually bring meaningful information, enabling fibre sensors to measure new physical quantities. For instance, self-heated fibres have been applied to measure hydrogen concentration [113], detect air flow as an anemometer [114], monitor the moisture of soil [115] and tunable filtering [116, 117]. Currently, two methods have been proposed to increase the fibre temperature: electrical heating and optical heating. In this section, the heating performance of the two methods is theoretically analysed at different temperatures and external pressures. In addition, the analysis on electrical heating is experimentally validated at room temperature.

4.3.1 Optical heating

A high power light beam (either continuous wave or pulsed) is necessary to realise optical heating. While a high power light passes through the optical fibre, a small portion of the light is absorbed and converted into thermal energy [118]. In practice, a highly attenuated fibre is used or the wavelength of the pump is chosen at the high absorption range of an optical fibre to enhance the heating efficiency. But both method introduce more propagation losses for the pump, hence reduces the maximum fibre length that can be heated. The efficiency can be further enhanced by collecting the light scattered out of the fibre using special coatings [119, 120].

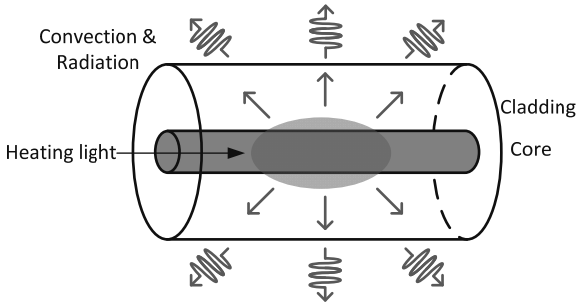

Figure 4-28. Thermal transfer in optical heating, the heat generated in fibre core transfers to cladding and finally dissipates into the air.

The thermal exchange for an optical heating process is schematically drawn in Fig. 4-28. A small part of the optical power inside the fibre core is absorbed and turns into heat to increase the fibre temperature. But some of the heat transfers to the cladding by thermal conduction and finally dissipates into the air through convection and radiation.

A thermal model is built up based on the thermal exchange illustrated in Fig. 4-27. The temperature distribution along the radial direction can be expressed in cylindrical coordinates [121]

$$\frac{\partial}{\partial r}\left[r\frac{\partial T_{core}(r)}{\partial r}\right]=-\frac{Q(z)}{\kappa},\qquad 0<r\le a\,, \tag{4-14}$$

$$\frac{\partial}{\partial r}\left[r\frac{\partial T_{core}(r)}{\partial r}\right]=0,\qquad a<r\le b\,, \tag{4-15}$$

where r represents the radial distance, a and b are the radii of core and cladding, respectively, and κ is the fibre thermal conductivity. The heat power density $Q(z)$ along the fibre is expressed as:

$$Q(z)=\eta\cdot\alpha\cdot P(z)\Big/\left(\pi a^2\right), \tag{4-16}$$

where η is the conversion ratio and $P(z)$ is the local optical power. In a standard fibre, the attenuation coefficient α is very small, so that the light absorption is uniform along a short piece of fibre. As a result, the thermal conduction along the fibre can be neglected, thus Eq. 4-14 can also be applied to retrieve the longitudinal thermal distribution by considering the light attenuation along the fibre.

The boundary conditions in the core and cladding are:

$$\left.\frac{\partial T_{core}}{\partial r}\right|_{r=0}=0,\quad \left.\frac{\partial T_{core}}{\partial r}\right|_{r=a}=\left.\frac{\partial T_{cladding}}{\partial r}\right|_{r=a},\quad T_{core}(r=a)=T_{cladding}(r=a) \tag{4-17}$$

In a stationary state and the boundary condition in the longitudinal direction is

$$\left.\frac{\partial T}{\partial z}\right|_{z=0} = \left.\frac{\partial T}{\partial z}\right|_{z=L} = 0\,, \tag{4-18}$$

where L is the length of the fibre.

Since the temperature exchange between fibre and air is dominated by convection and radiation as shown in Fig. 4-27, the boundary condition at the interface of fibre and air is determined according to Newton's and Stefan-Boltzmann's laws [122]:

$$\left.\frac{\partial T_{cladding}}{\partial r}\right|_{r=b} = \frac{H}{\kappa}\left(T_\infty - T_{cladding}\right) + \frac{\delta_{SB}}{\kappa}\varepsilon_e\left(T_\infty^4 - T_{cladding}^4\right), \tag{4-19}$$

where H is the convective coefficient, T_∞ is the ambient temperature, δ_{SB} is the Stefan-Boltzmann constant and ε_e is the emissivity. The convective coefficient H is normally chosen to be 10 W/(m^2 K) for silica fibre coated by polymers under free convection [122].

When the fibre temperature is not very high, the heat loss is dominated by convection at the pressure of one atmosphere. Then it becomes negligible when the external pressure is reduced such that the ratio between the mean free path of molecules and a representative physical length becomes larger than 1, leading to a heat transfer coefficient below 0.01 W/(m^2 K) at very low pressures [123]. In this case, radiation dominates the thermal dissipation, so that the heating becomes more efficient in vacuum.

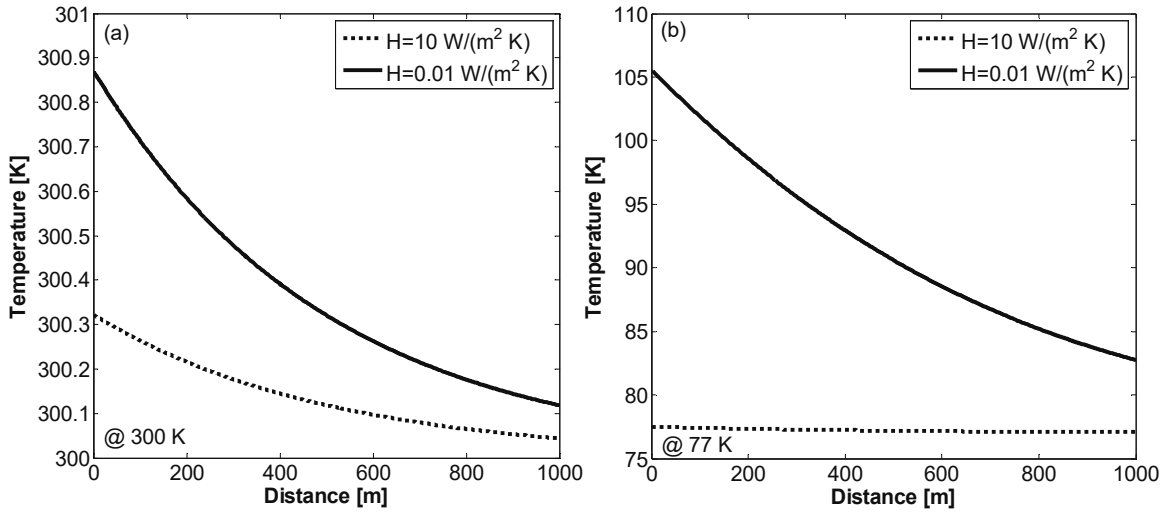

Figure 4-29. Thermal distribution of optical heating under different convection along the fibre at (a) 300 K and (b) 77 K. the heating is more efficient at cryogenic condition or in vacuum.

The optical heating is simulated for a 1 km long fibre with 2 dB/km attenuation coefficient, which is pumped by a continuous incident light with optical power of 1 W. The value of the loss coefficient is reasonable for long wavelengths (> 1650 nm) where the light attenuation is mostly dominated by absorption, or for shorter wavelength around 1380 nm, which is the absorption spectrum of the OH- impurities in the fibre. Fibres with higher attenuation can also be used, and higher temperature can be achieved with a limited heating distance due to the optical loss. In this case, Eq. 4-14 is assumed still valid to describe the thermal longitudinal distribution for

simplicity. However, the Rayleigh scattering also accounts for the optical power loss, so not all the attenuated optical light is converted into thermal energy in the fibre core. A special coating can be used to absorb the scattered light and turn it into heat. As a result, it is assumed that all the attenuated optical light is converted into heat so the conversion ratio is 1. The fibre thermal conductivity is set as 1.38 W/(m K), and the radii of fibre core and cladding are considered to be 4 μm and 62.5 μm, respectively.

The simulation results under different temperatures and pressures are shown in Fig. 4-29. The obtained temperature decays exponentially along the fibre because of the pump attenuation. It has to be pointed out that the thermal analysis here neglects the heat conduction along the fibre. Actually, the temperature profile turns out to be more uniform in practice because of the longitudinal thermal conduction [124]. The temperature increase is much higher at 77 K than at room temperature, so that the optical heating is more efficient under cryogenic conditions. In addition, a higher temperature increase is observed in vacuum because of the weak convection, confirming that the convection (represented by the factor *H*) has an obvious impact on the temperature change at ambient (Fig. 4-29a) and cryogenic (Fig. 4-29b) conditions.

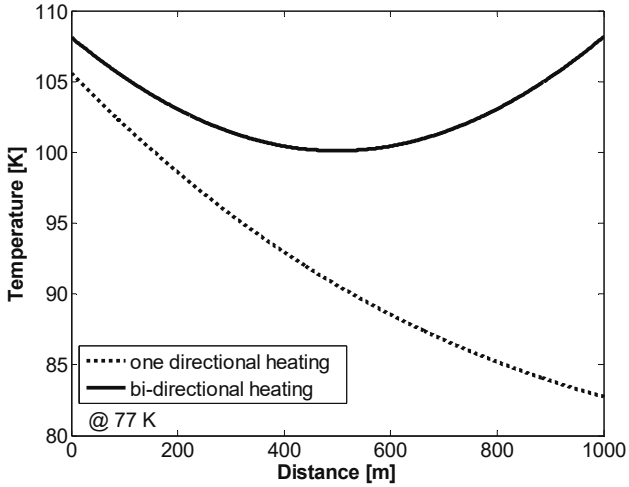

Figure 4-30. Theoretical comparison of thermal distribution along an optical fibre at 77 K using both single and dual pumping scheme.

As shown in Fig. 4-29, the increased temperature decays along the fibre due to the pump attenuation, resulting at a non-uniform temperature profile and a very weak heating effect at the far end for the fibre. A simple method to optimise the thermal distribution is to use a bi-directional pumping, launching the pump light from both sides of the fibre [125]. Figure 4-30 compares the temperature distribution under single (dotted line) and dual pumps (solid line) at 77 K. Obviously, a more uniform temperature profile is obtained by the bi-directional optical pumping. And the temperature of the whole fibre is raised from 77 K to 100 K or even higher, with 1 W optical power into each of the fibre ends.

4.3.2 Electrical heating

While an electrical current passes through a conductor, some kinetic energy is released due to the collision of charged particles and the atomic ions, which rises the temperature of the conductor. To realise electrical heating, a metal coating is usually utilised, where the electrical energy is converted to thermal energy that heats the fibre.

For electrical heating, a part of the generated heat transfers from the metal coating to the optical fibre by thermal conduction, and the other part is lost into the air by convection and radiation. The whole process is

schematically shown in Fig. 4-31 and it can be modelled as a silica cylinder with thin-film thermal source on its surface and surrounded by air [126]. Due to the small fibre radius compared with the fibre length, the heat flow in the radial direction can be safely neglected. Thus the thermal exchange for this metal coated fibre obeys the following equation [127]

$$\frac{\partial T(z,t)}{\partial t} = K_D \frac{\partial T^2(z,t)}{\partial z^2} + \frac{P_{in}(z,t) - P_{out}(z,t)}{\rho c_p \pi (b+d)^2}, \tag{4-20}$$

where z is the distance along the fibre, d is the thickness of the coating and K_D, ρ and c_p are the thermal diffusivity, density and constant pressure heat capacity of silica, respectively, P_{in} is the heating power density per unit length from the coating, and P_{out} is the dissipated thermal power density by convection and radiation.

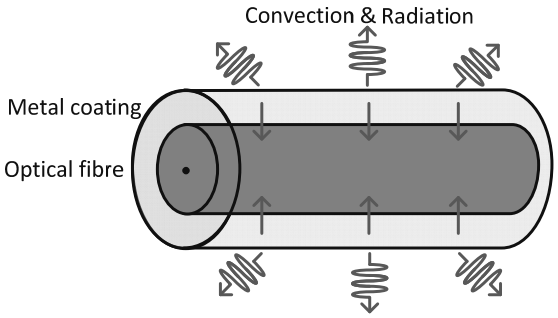

Figure 4-31. Thermal transfer in electrical heating: thermal energy generated in the metal coating transfers to the fibre and raises the temperature and the rest dissipates into the air.

Only the steady state of the thermal exchange is considered when the electrical heating is applied to distributed fibre sensing that is usually a pseudo-static measurement. Thus the left-hand side term of Eq. 4-20 becomes zero. Additionally, the optical fibre and the metal coating are longitudinally uniform under the ideal case, so that the generated heat is also uniform along the fibre. Therefore, the first term on the right-hand side of Eq. 4-20 becomes zero as there is no thermal conduction along the fibre. Eventually, the input electrical power is totally lost by radiation and convection, expressed as $P_{\text{in}} - P_{\text{out}} = 0$ that can be rewritten as:

$$I_c^2 \frac{\rho_r}{2\pi^2 d(2b+d)(b+d)} = \delta_{SB}\varepsilon_e \left(T^4 - T_\infty^4\right) + H(T - T_\infty), \tag{4-21}$$

where ρ_r is the resistivity of the metal coating, I_c is the current passing through the coating, H is the convective coefficient for the metal and ε_e is the emissivity of the metal coating. Equation 4-18 is very similar to the boundary function of optical heating expressed by Eq. 4-19, as both of them present that the generated heating is totally lost by radiation and convection.

When the radiation dominates the process, the second term on the right-hand side of Eq. 4-21 can be neglected, so that the increased temperature turns strongly dependent on T_∞, making the heating more efficient at low temperatures. However, when natural convection plays the main role in the thermal loss, the relation becomes much less dependent on the ambient temperature.

At ambient pressure, the convective coefficient H is typically above 100 W/(m^2 K) for different metal coatings according to the Ref. [128-130]; but it falls below 0.01 W/(m^2 K) at very low pressures. Actually, the convective coefficient is temperature dependent, so in the following analysis the coefficient is expressed as [128]:

$$H = H_0 + \Delta H / \Delta T \left(T - T_\infty \right), \tag{4-22}$$

where H_0=130 W/(m^2 K) and $\Delta H/\Delta T$=0.299 W/(m^2 K^2).

The electrical heating of a fibre with 25 μm thick Al coating is simulated at 300 K and 77 K. The Al resistivity is 2.733×10^{-8} Ω m at 300 K and 1.62×10^{-9} Ω m at 70 K [131] and it is assumed to be constant during the heating process for simplicity. The emissivity of the aluminium oxide 0.15 is used in the simulation [132], because aluminium gets oxidised easily in the open air.

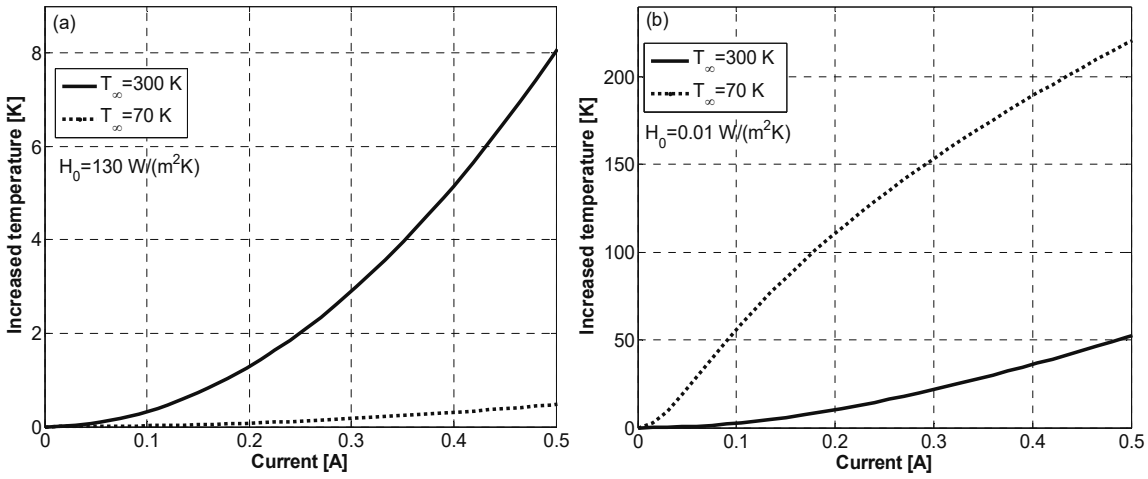

Figure 4-32. Increased temperature of Al coated fibre under different current and thermal conditions at (a) ambient pressure and (b) very low pressure.

The simulation results for the Al coated fibre is presented in Fig. 4-32, showing the increased temperature under different currents at ambient pressure and in vacuum. Under normal ambient pressure, the fibre temperature rises by < 0.5 K with an input current of 0.5 A, as shown in Fig. 4-31a, because most of the input electrical power is finally lost by convection. And electrical heating becomes less efficient under cryogenic conditions because the metal resistivity usually decreases at low temperature. However, very high heating efficiency is observed in vacuum (less than 10^{-2} Pa), as shown in Fig. 4-31b, because radiation becomes the dominating factor in thermal dissipation, so that less thermal energy is lost. In addition, the temperature increases more at 70 K despite of the low metal resistivity, demonstrating the key role played by ambient temperature when radiative dissipation dominates. But the input electrical power must be controlled, so that the fibre temperature is under the melting point of the Al-coating.

4.3.3 Experiment validation for electrical heating

A Brillouin distributed fibre sensor is employed to measure the temperature change induced by electrical heating along an Al coated optical fibre to confirm the theoretical model. And Fig. 4-33 illustrates the working principle of a standard BOTDA sensor: a probe (CW light) gains or loses optical power due to an interaction with a counter-propagating pump (optical pulse) through the SBS process. The Brillouin spectrum is plotted by recording the probe power at different optical frequencies in order to determine the Brillouin frequency along the fibre, which reveals the temperature and strain information.

The typical spatial resolution of a standard BOTDA system is at least 1 m because of the decaying time of the acoustic wave in silica. But a better spatial resolution must be achieved due to the short fibre length (1.3 m). In this case, a double-pulse scheme in a standard BOTDA is implemented [133]. Two short pulses are

sequentially launched into the optical fibre with a time difference that is smaller than the acoustic wave decaying time. Thus the acoustic waves generated by two pulses will interfere with each other, so that the resultant Brillouin spectrum is narrowed and the peak gain is increased. Optical pulses with 2 ns width are used in the experiment, corresponding to a 20 cm spatial resolution.

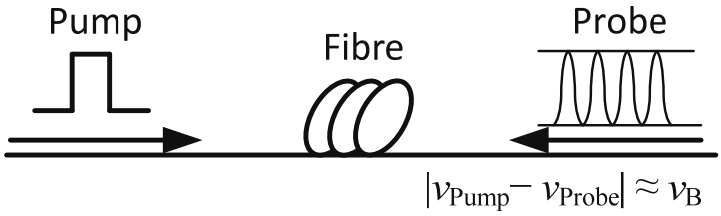

Figure 4-33. Frequency scanning of the probe to obtain Brillouin frequency in a Brillouin optical time domain analyser.

Figure 4-34 shows the experimental setup of the double-pulse BOTDA. The CW light from a LD is divided into two branches by a splitter. The upper branch is dedicated to the generation of pump pulses with high optical power. The CW light is converted into two successive narrow pulses with 2 ns interval by an EOM, then the pulses are amplified by an EDFA and their peak power is controlled by an attenuator. A polarisation switch is used to avoid the polarisation dependence of the Brillouin scattering, achieving polarisation-independent measurements. Finally, the pump pulses are launched into a short optical fibre coated with Al through a circulator. The metal coating is connected to a tunable power source to apply current. The coated fibre is isolated against environmental air flows to prevent any extra thermal exchange between coating and surrounding air. On the other hand, the lower part is dedicated to realise the frequency scanning of the probe. Two sidebands are generated by another EOM driven by a RF source, while the carrier is suppressed by controlling the DC voltage. Then the probes are launched into the fibre through an isolator, which is employed to block the pump pulses. At the receiver part, one of the two probes is selected by a FBG and is collected by a fast photodetector.

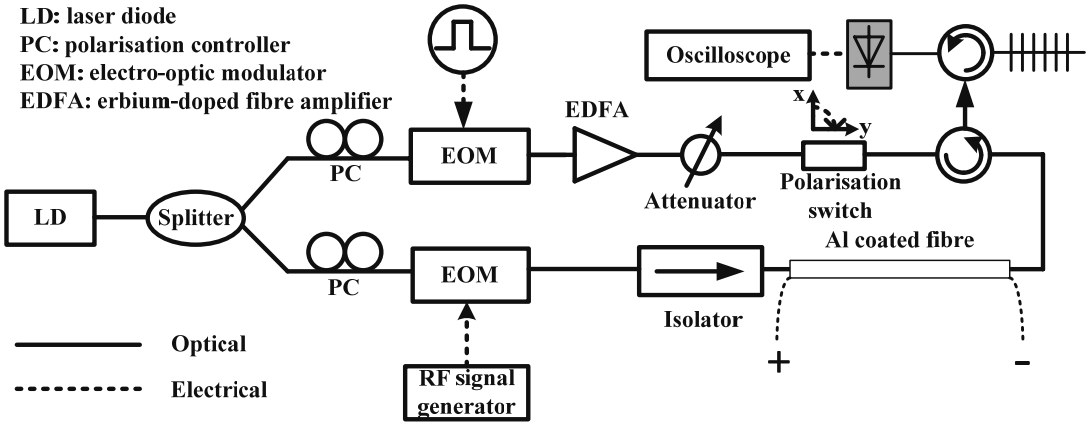

Figure 4-34. Experimental setup to validate the electrical heating by a double-pulse Brillouin optical time domain analyser.

4.3.3.1 Characterisation of the thermal response for an Al-coated fibre by Brillouin sensing

To measure the temperature of a heated fibre by Brillouin sensing, the thermal response of the metal-coated fibre must be characterised first. As stated in Chapter 1, the typical sensitivity of a Brillouin sensor is ~ 1 MHz/K for the standard SMF. But the study in section 4.2.3 shows that the thermal expansion in the coating will enhance the temperature sensitivity of the COTDR sensor. Thus, it is reasonable to expect a higher sensitivity for Brillouin sensors, which has never been investigated so far.

The ratio between the cross-sectional area of the coating and the fibre is calculated to be 0.96 as the radius of the optical fibre is 62.5 μm and the metal coating is 25 μm thick. The thermal expansion coefficient and Young's modulus of Al are ~ 0.41×10^{-6} K^{-1} [134] and 71 GPa [135], respectively. Thus the strain induced by 1 K temperature change is 11.25 με based on Eq. 4-11.

The typical temperature and strain sensitivities of a Brillouin sensor are 0.95 MHz/K and 0.05 MHz/με in a standard SMF [136]. Thus the resultant temperature sensitivity in the Al coated fibre is

$$Sen_{temp}^{'} = Sen_{temp} + \delta L/L \cdot Sen_{strain} \approx 1.512 \quad \text{MHz/K}, \tag{4-23}$$

demonstrating that a 25 μm thick Al coating enhances the temperature sensitivity by ~ 50 %.

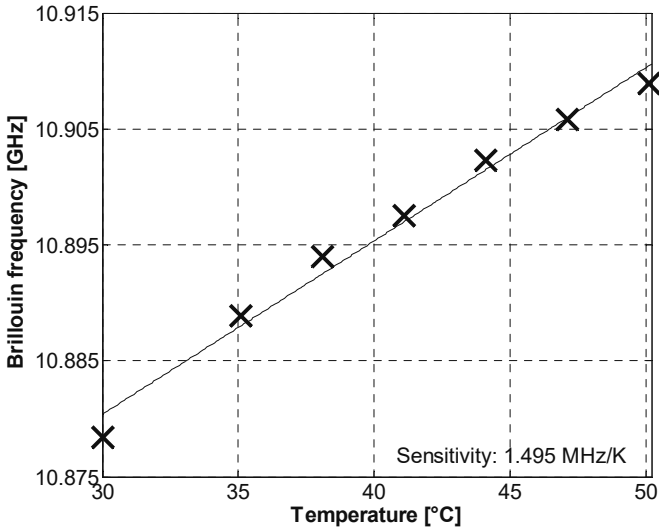

Figure 4-35. Brillouin frequency shift versus temperature change for Al-coated optical fibre.

Placing the coated fibre in a thermal bath, the Brillouin frequency is measured at different temperatures and is plotted in Fig. 4-35. The measured sensitivity is about 1.51 MHz/K, which is very close to the theoretical analysis and confirms the sensitivity improvement by the special 25 μm Al-coating.

4.3.3.2 Experimental results for electrical heating

With the temperature sensitivity of the metal-coated fibre, the increased temperature through the electrical heating is measured by the double-pulse BOTDA. Actually, the metal resistance is dependent on temperature, thus solving Eq. 4-18 becomes more complicated. To avoid this problem, the input power is expressed as the product of current and voltage to avoid the resistivity in Eq. 4-18. Hence the Brillouin frequency shift and gain spectrum of the coated fibre under different electrical powers are measured and shown in Fig. 4-36, regardless of any metal resistivity change.

The Brillouin frequency is upshifted because of the temperature increase by the electrical power. As shown in Fig. 4-36a, the Brillouin frequency barely varies along the fibre under low electrical powers, representing a more uniform temperature profile than the optical heating. However, longitudinal fluctuations are observed when high electrical powers are applied. Since the fibre is well thermally isolated, this could be explained by the non-uniform thickness and/or the resistivity of the coating. This also indicates that the uniformity of the metal coating can be measured by the distributed temperature sensing and electrical heating. Figure 4-36b presents the averaged Brillouin gain spectra under different electrical powers, showing that they are distorted when high

electrical powers are applied, which is also caused by the non-uniform temperature along the entire fibre. In addition, sidelobes are observed in Fig. 4-36b, as expected from the double-pulse BOTDA system due to the interference among the acoustic waves [133]. With the temperature sensitivity of 1.49 MHz/K measured above, the obtained Brillouin frequency can be converted into temperature.

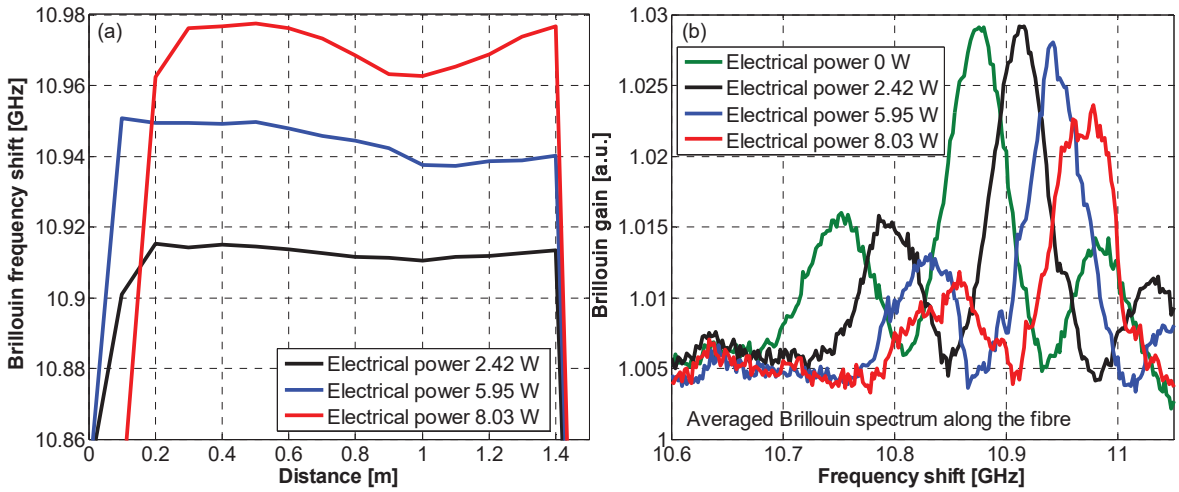

Figure 4-36. (a) Measured Brillouin frequency and (b) averaged Brillouin spectrum along the Al-coated fibre with different electrical power.

Then the theoretical analysis based on Eq. 4-21 and the experimental results are compared in Fig. 4-37 under different electrical powers. The experimental results agree with the simulation very well, thus validating the model. However, a small discrepancy appears when using an electrical power above 6 W, which could also be explained by the non-uniformity of the coating.

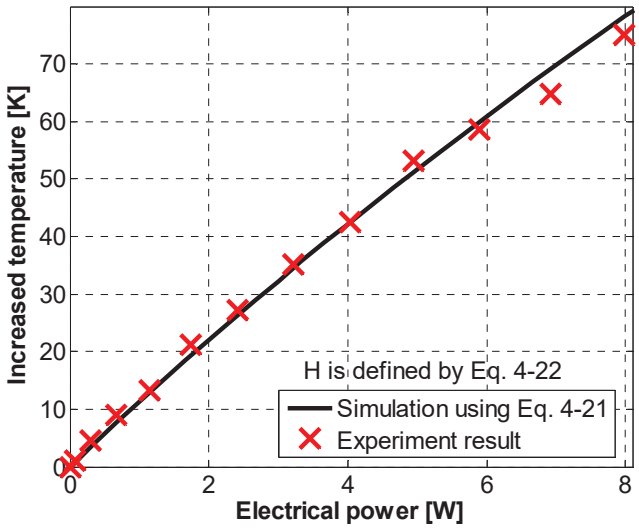

Figure 4-37. Comparison of experimental result and simulation for electrical heating.

4.3.4 Conclusion

Optical and electrical heating methods are investigated in this section to increase the fibre temperature. Electrical heating turns to be much more efficient than optical heating. For example, 1 W electrical power would increase

the fibre temperature by over 10 K at room temperature, as shown in Fig. 4-37, while the same amount of optical power just raises fibre temperature by 0.3 K for a fibre with 1 dB/km attenuation coefficient under the assumption that all the lost optical power is converted into heat, as shown in Fig. 4-28a. Of course, a higher attenuation coefficient will lead to a higher efficiency for the optical heating, but it limits the heated distance range using the same optical power. Besides, electrical heating leads to a more uniform thermal profile along optical fibre, as presented in Fig. 4-36a. On the other hand, the raised temperature demonstrates exponential decay for optical heating because of the light attenuation. However, the exposed current limits the applications of the electrical heating, e.g. it is inapplicable to flammable environments; and the heating efficiency becomes poor at low temperature because the resistivity of the metal drops dramatically. The optical heating keeps the EM immunity of the optical fibre and can be applied to a broad working field in contrary to the electrical heating method.

Then the thermal response of the metal coated fibre is theoretically analysed and experimentally characterised. The thermally induced strain in the coating is proved to enhance the thermal response measured by a Brillouin DFS: a 25 μm thick Al coating enhances the temperature sensitivity by ~ 50 %. With the measured sensitivity, the electrical heating model is validated by a double-pulse BOTDA.

Chapter 5
Distributed Fibre Sensing Based on Coherent Rayleigh Scattering Measurements of Birefringence

The COTDR technique demonstrates an excellent performance in the field of distributed fibre sensing because the random interference process is sensitive enough to measure precisely the refractive index and the scattering size changes induced by environmental variations, as described in the previous chapter. Based on the same working principle, the intrinsic index difference of the orthogonal eigen axes, named as phase birefringence, can also be measured. In section 5.1, the birefringence distribution along the fibre is measured by the COTDR method for PM fibres and different types of standard SMFs.

The birefringence is a result of the fibre core cross-section asymmetry, which is formed during an imperfect manufacturing process and is dependent on the environmental variables. Consequently, temperature and strain variations can change the local birefringence, which can be measured by the technique proposed in section 5.1. Hence, the distributed fibre sensing is realised by birefringence measurement based on coherent Rayleigh scattering in section 5.2. The temperature and strain sensitivities are characterised for a PANDA fibre and an elliptical-core PM fibres, respectively. In addition, the discrimination of temperature and strain is realised by combining the birefringence measurement with the COTDR technique.

5.1 COTDR for birefringence measurement

Birefringence is one of the most important factors that limit the data rate capability of optical fibre communications. Although current techniques are able to manufacture optical fibres with a birefringence down to 10^{-7}, a large birefringence can still be introduced by bends and twists during cabling and installation processes. In addition, the birefringence distribution along the fibre is crucial to compensate the polarisation mode dispersion.

On the other hand, a large birefringence ($\sim 10^{-4}$) is deliberately introduced to the PM fibres, so that the polarisation of the light aligned to the eigen axes is preserved. But the imperfect fabrication process may cause fluctuations of the birefringence along the fibre, undermining its performance. As a result, special technique is needed to characterise the birefringence distribution along the standard SMFs and PM fibres.

So far, several methods have been proposed to measure the phase birefringence distribution along the fibre. Special data processing is required to retrieve the local birefringence for POTDR [137] and BOTDR methods [138]. OFDR provides high spatial resolution but the sensing distance is limited by the coherent length of the light source [139]. Only OFDR with complex modifications is able to measure long fibres. Another technique to measure the birefringence profile is Brillouin dynamic grating (BDG), in which high power light, special polarisation control and precise frequency adjustment are needed [140].

In Chapter 4, the COTDR technique has been proven to be very sensitive to the refractive index change and the corresponding simulation reveals that it can detect an index change around 10^{-6}. Thus it is potentially possible to measure the birefringence in standard fibres and PM fibres. The experimental setup of a COTDR system is simpler than the OFDR and BDG methods and the data processing is more straightforward than POTDR and BOTDR techniques.

5.1.1 Working principle for birefringence measurement

The polarisation of the incident light is not considered in a COTDR system in Chapter 4. But to measure the birefringence profile, the coherent Rayleigh trace must be obtained at two orthogonal polarisation states, so the birefringence is given by the cross-correlation of their spectra. For the sake of simplicity, the measurement in a PM fibre is first explained and this theory is applied to a SMF later.

Birefringence measurement is also based on the restorability of the coherent Rayleigh trace. According to the analysis in Chapter 3, the shape of a Rayleigh trace is dependent on the reflection coefficient of the scattering point and the optical phase which is related to the propagation constant β. In addition, the light is assumed to be incident normally on the scattering points, so the reflection induced phase change is either 0 or π.

The reflection coefficient at the ith scattering section in both axes is determined by Fresnel equation:

$$r_{R,i}^{x}=\left|\frac{n_i-n_{i+1}}{n_i+n_{i+1}}\right| \qquad r_{R,i}^{y}=\left|\frac{(n_i-B)-(n_{i+1}-B)}{(n_i-B)+(n_{i+1}-B)}\right|, \tag{5-1}$$

where $B = n_x - n_y$ is the phase birefringence, n_i and n_{i+1} are the refractive indices in the slow axis at corresponding points, respectively. Since $B \ll n$, the reflection coefficient of the fast axis is approximated to be the same as that in slow axis:

$$r_{R,i}^{y}=\left|\frac{(n_i-B)-(n_{i+1}-B)}{(n_i-B)+(n_{i+1}-B)}\right|=\left|\frac{n_i-n_{i+1}}{n_i+n_{i+1}-2B}\right|\approx\left|\frac{n_i-n_{i+1}}{n_i+n_{i+1}}\right|=r_{R,i}^{x}. \tag{5-2}$$

As a result, the restorability for the birefringence measurement depends only on the phase of the reflected light in different axes.

The optical phase of the backscattered light is normally made of contributions from light reflection and propagation. The reflection induced phase change at ith scattering points is 0 if $n_{i-1} > n_i$ or π when $n_{i-1} < n_i$. Since the index difference between adjacent inhomogeneities in one axis equals to the difference in the other axis, the reflection caused phase change at a given position is the same for the slow and fast axes. Consequently, the restorability for the birefringence measurement eventually depends on the propagation constant.

To realise the same shape for difference coherent Rayleigh traces, the propagation constants in both axes should be the same: $\beta_x = \beta_y$. Considering the expression of β, the following phase relation is obtained:

$$2\pi \frac{n_x(\nu_x)\nu_x}{c} = 2\pi \frac{n_y(\nu_y)\nu_y}{c} \quad \rightarrow \quad n_x(\nu)\nu = n_y(\nu+\Delta\nu)\cdot(\nu+\Delta\nu), \tag{5-3}$$

where ν_x, ν_y and n_x, n_y are the optical frequencies and effective refractive indices along the two orthogonal polarisation axes (slow and fast axes) and $\Delta\nu = \nu_y - \nu_x$. Applying Taylor expansion to the refractive index of the fast axis, $n_y(\nu+\Delta\nu)$ can be expressed as $n_y(\nu) + \Delta\nu \cdot d\left[n_y(\nu)\right]/d\nu$ while the second- and higher-order terms are omitted [140]. Thus, Eq. 5-3 can be rewritten as

$$\left[n_x(\nu) - n_y(\nu)\right]\nu = \Delta\nu \cdot \left[n_y(\nu) + \nu\, dn_y(\nu)/d\nu\right] + \Delta\nu^2 \cdot dn_y(\nu)/d\nu\,. \tag{5-4}$$

The second term on the right hand side of Eq. 5-4 is much smaller than the first term, so that it can be neglected. Based on the definition of the group refractive index $n_y^g = d\left[n_y(\nu)\nu\right]/d\nu$, the relation between frequency shift and birefringence is obtained:

$$B = n_y^g \cdot \frac{\Delta\nu}{\nu}\,. \tag{5-5}$$

Equation 5-5 is exactly the same as the result for the BDG [140].

The birefringence B of a standard PM fibre is in the order of 10^{-4}, requiring a broad frequency scanning (typically several tens of GHz) according to Eq. 5-3. This will highly increase the cost of the whole system and the measurement time. But this problem can be partially avoided if the approximate birefringence value is known. Hence just two narrow spectral regions are needed to scan for the two sets of measurements with a frequency separation that roughly meets the relation shown as Eq. 5-3. The actual frequency shift $\Delta\nu$ is the sum of this frequency separation and the cross-correlation result of the two measurements.

For conventional PM fibres, the coherent Rayleigh traces can be alternately acquired by adjusting the polarisation of the interrogating pulse to match the two orthogonal birefringence axes. This can be implemented using a polarisation controller or a polarisation switch that changes between orthogonal SOPs. A good polarisation alignment can maximise the amplitude value of the correlation peak along the fibre. If there is a minor mismatch between the optical pulse polarisation and one of the eigen axes, the two measurements would contain slightly correlated information because the obtained signal carries the trace measured in the same axis within the same frequency range, resulting in an additional correlation peak at zero-frequency (assuming the environmental condition remains the same). Actually, the height of the correlation peak is determined by the ratio of light coupled in each of the axes. For example, when linearly polarised light is launched into the fibre with a 45° angle with respect to the fibre axis, the two sets of COTDR traces contain almost the same information of both axes in the same frequency range, giving rise to a high correlation peak at zero-frequency and a low peak at $\Delta\nu$. In the extreme case, no correlation peak can be found if the pulses at higher optical frequency enter the slow axis and the lower frequency pulses enter the fast axis [141].

5.1.2 Birefringence measurement for PM fibres

A COTDR system for distributed fibre sensing can be utilised directly for the birefringence measurement with some additional components to adjust the polarisation of the pulses launched into the fibre. The experimental setup for distributed birefringence measurement is shown in Fig. 5-1. Compared with the standard COTDR

sensor shown in Fig. 4-13, the polarisation of the incident pulse is adjusted and the state of the polarisation is monitored for the birefringence measurement.

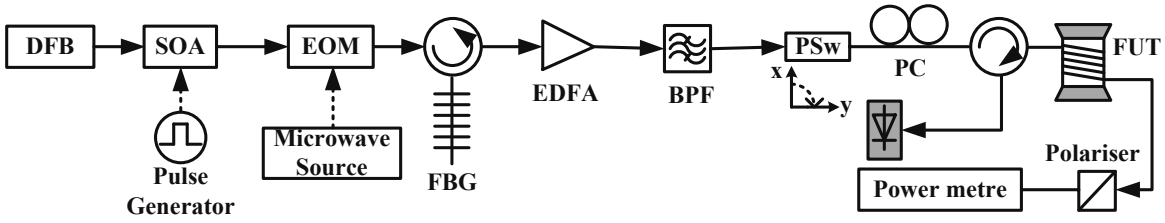

Figure 5-1. Experimental setup to measure the birefringence distribution along the PM fibre. DFB: distributed-feedback laser, SOA: semiconductor optical amplifier, EOM: electro-optic modulator, FBG: fibre Bragg grating, EDFA: erbium-doped fiber amplifier, BPF: band pass filter, PSw: polarisation switch, PC: polarisation controller, FUT: fibre under test.

A distributed-feedback (DFB) laser operating at 1534 nm is used as the light source. The CW light is converted into optical pulses by a SOA to reach high extinction ratio (more than 50 dB). Like in a standard COTDR, the fine frequency tuning is realised by an EOM driven by a microwave source at several GHz and one of the generated sidebands is selected by a tunable FBG, the same one used for temperature sensing. But large frequency shift (many tens of GHz) is needed to measure the PM fibre, which is realised by tuning the laser driving current. The optical pulses are boosted by an EDFA and the ASE is suppressed by a BPF with 100 GHz bandwidth. Then a polarisation switch (PSw) and a PC are used to launch the optical pulse with orthogonal polarisation states into the corresponding axes of the FUT through a circulator. The polarisation switch alternates the polarisation of the light between two orthogonal states while the PC is used to align the linearly polarised pulses to the right polarization axes of the fibre. A polariser and a power metre are connected to the far end of the FUT to ensure a good polarisation alignment to the PM fibres. The optical component aligned to the slow axis of the fibre will pass through the polariser while the orthogonal part is blocked, as a result, the power metre shows the highest power when the incident light is perfectly aligned to the slow axis but a power close to 0 during the measurement along the fast axis. The Rayleigh backscattered light is directed into a 125 MHz photodetector through the circulator, and the obtained signal is processed by a computer.

A 90 m PANDA and a 100 m elliptical core PM fibre are tested using the setup shown in Fig. 5-1. The optical pulse width is set as 20 ns, equivalent to 2 m spatial resolution. The frequency scanning step is 10 MHz but different fibres are measured within different frequency ranges.

The cross-correlation results of the coherent Rayleigh traces from the fast and slow axes of both PM fibres are presented in Fig. 5-2. The correlation frequency profile is obtained and plotted along the fibre by fitting the correlation peak spectrum with a quadratic curve [105], as shown in the inset of Fig. 4-17. Based on Eq. 5-3, the correlation frequency profile $\Delta\nu(z)$ is converted into the local phase birefringence $B(z)$, as shown by the right-hand side vertical axis of the figures. The depicted experimental results clearly show the non-uniform phase birefringence profiles along both optical fibres with 2 m spatial resolution.

The birefringence measurement is essentially based on the COTDR technique, so it suffers from the environmental perturbations between the two measurements for orthogonal polarisations. During the measurement time in the order of a few tens of seconds for such short fibres, the temperature drifts and laser frequency fluctuations could cause a frequency shift up to a few tens of MHz, which is considered as the measurement error for the birefringence. However, In the case of measuring fibres with high birefringence, this error is less than 1% of the absolute measured frequency (being of the order of tens of GHz), which is usually tolerable [141].

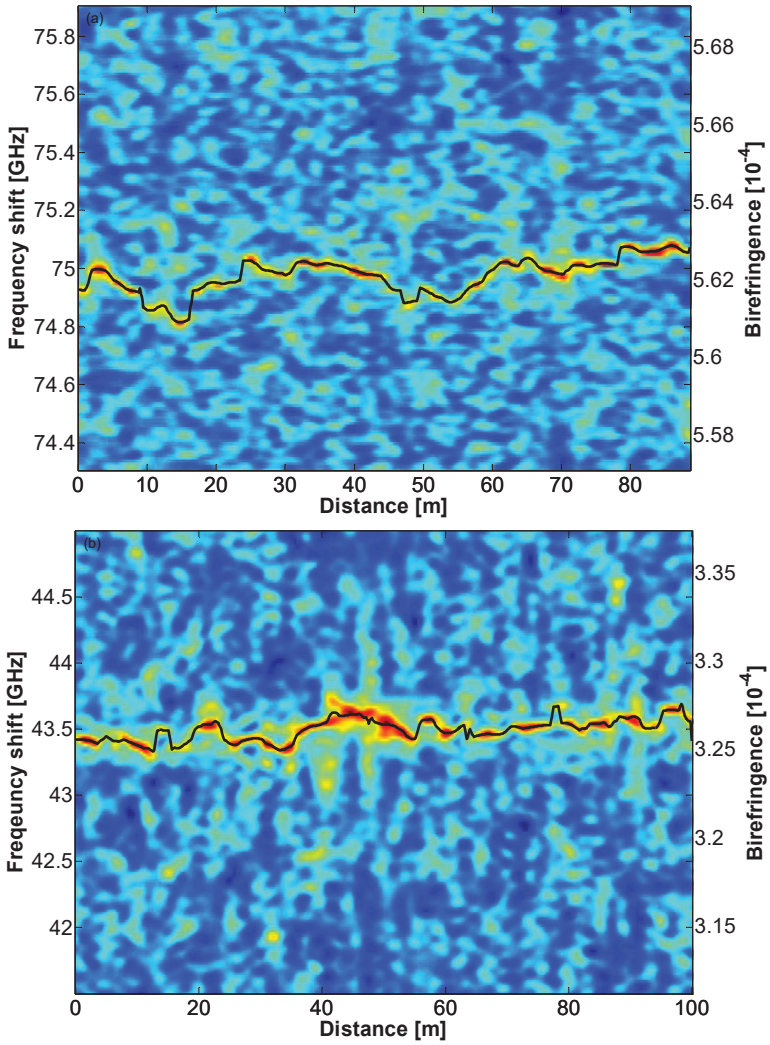

Figure 5-2. Measured phase birefringence distribution along (a) a 90 m PANDA and (b) a 100 m elliptical-core PM fibres. Left-hand side vertical axis: Measured frequency shift. Right-hand side vertical axis: Birefringence value calculated using Eq. 5-5.

In order to confirm the experimental result, a Sagnac loop is built to measure the group birefringence. Reported research has presented that the difference between phase and group birefringence of a PANDA PM fibre is very small (less than 10%) [142] but a large difference is observed for an elliptical core PM fibre [143]. Thus the Sagnac loop can validate only the PANDA fibre; however, this is enough to verify this method.

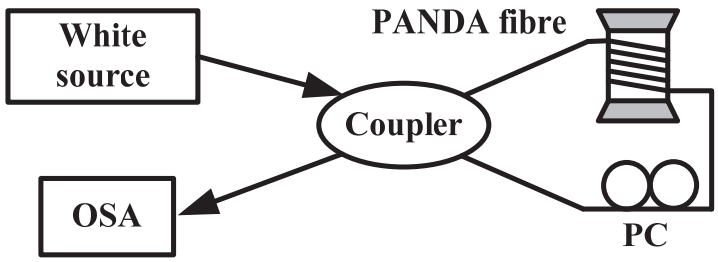

Figure 5-3. A Sagnac loop to validate the birefringence measurement based on coherent Rayleigh scattering. PC: polarisation controller, OSA: optical spectrum analyser.

Figure 5-3 shows a Sagnac loop for the group birefringence measurement in a PANDA PM fibre. The CW light from a white source is split by a 50:50 coupler and the two beams propagate opposite to each other along the PANDA fibre, they are then recombined at the same coupler and the output light is monitored by an OSA. The interference of the two beams is determined by the propagating time through the loop, which is dependent on the phase birefringence. A PC is inserted in the loop to adjust the light polarisation in order to optimise the interference result. And the optical intensity transmission is expressed as [144]:

$$Tran = \sin^2\left[\frac{\pi B(\lambda)L}{\lambda}\right], \tag{5-6}$$

where $B(\lambda)$ is the wavelength dependent phase birefringence, L is the length of the PM fibre and λ represents the incident wavelength. According to this equation, it is expected to observe a fringe pattern at the output of the coupler. Two adjacent dips at the transmission port obey the following relation,

$$\pi + \frac{\pi B(\lambda+\Delta\lambda)L}{\lambda+\Delta\lambda} = \frac{\pi B(\lambda)L}{\lambda} \rightarrow 1 + \frac{L}{\lambda+\Delta\lambda}\left[B(\lambda) + \Delta\lambda\frac{dB(\lambda)}{d\lambda}\right] = \frac{B(\lambda)L}{\lambda}, \tag{5-7}$$

where $\Delta\lambda$ is the wavelength spacing between the dips. Here the phase birefringence $B(\lambda+\Delta\lambda)$ has been rewritten as $B(\lambda) + \Delta\lambda \cdot d[B(\lambda)]/d\lambda$ using Taylor expansion and neglecting the second- and higher-order terms. As a result, the wavelength spacing $\Delta\lambda$ between two adjacent dips is expressed as

$$\Delta\lambda = \lambda^2 \Big/ \left[L\left(B - \lambda\frac{dB}{d\lambda}\right)\right] = \frac{\lambda^2}{B^g \cdot L}, \tag{5-8}$$

which is inversely proportional to the fibre length and the group birefringence $B^g = B + \Delta\lambda \cdot d[B(\lambda)]/d\lambda$ [144]. Thus the group birefringence can be obtained from $\Delta\lambda$ by Eq. 5-8.

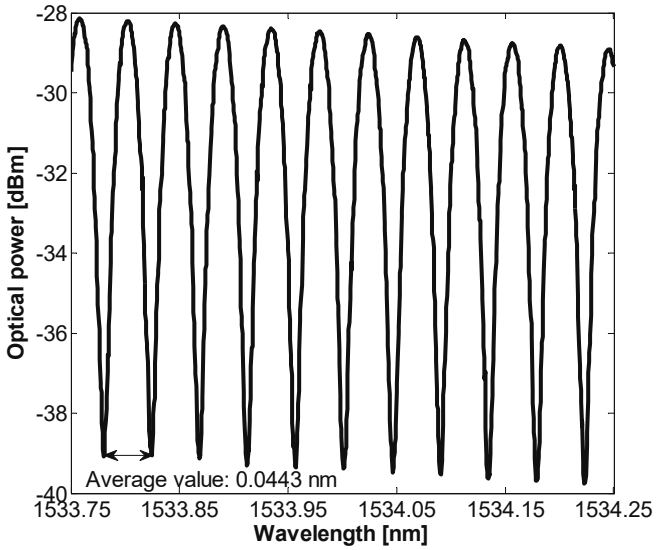

Figure 5-4. Output of the Sagnac loop with PANDA fibre at 1534 nm.

The obtained fringe pattern from the Sagnac loop around 1534 nm is shown in Fig. 5-4, the mean value of the free spectral range $\Delta\lambda$ is measured to be 0.0443 nm. Thus the group birefringence is calculated to be 5.90×10^{-4} using Eq. 5-8. Meanwhile, the average phase birefringence is measured as 5.62×10^{-4} by the proposed method. As a result, the ratio between the measured phase and group birefringence is 0.95, which is close to the reported

result 0.91 [142]. Consequently, the Sagnac loop validates the birefringence measurement by the proposed method.

5.1.3 Birefringence measurement for standard SMFs

As analysed above, the COTDR technique is also able to measure the phase birefringence in standard SMFs thanks to its high sensitivity. Old SMFs are employed to evaluate the performance of this technique in the application to a low birefringence measurement. These fibres were fabricated in the mid 1980's, and they show comparatively higher birefringence than present-day fibres.

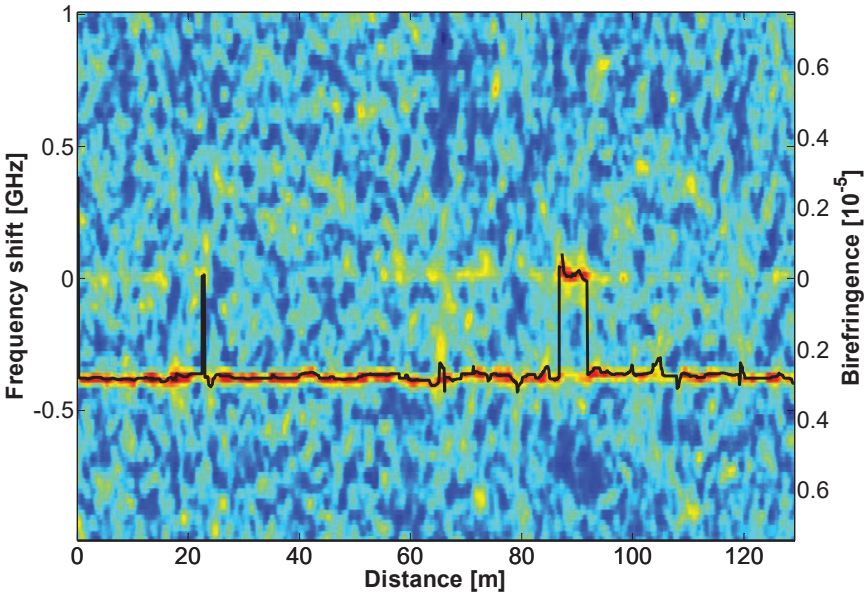

Figure 5-5. Cross-correlation result for a Philips fibre.

Some of the old fibres are measured by the same experimental scheme shown in Fig. 5-1 and the polarisation alignment becomes more critical in this case because there are no specified polarisation axes in SMFs. The correlation result is shown in Fig. 5-5 for a Philips fibre. Like the measurement result in PM fibres, a clear peak is observed along the fibre and the frequency shift is about −0.4 GHz for most part, corresponding to a birefringence of 3×10^{-6}. This result validates the COTDR technique is able to measure the birefringence down to the order of 10^{-6}.

The correlation peak shows no frequency shift at ~ 90 m, demonstrating two measurements carrying the same information. This might be due to the extremely low birefringence at that section. But a more likely explanation is that the birefringence changes abruptly at this position, so that the incident optical pulses couple almost equally into both axes, thus their backscattered light carries the same information about both fast and slow axes, giving rise to a correlation peak at zero frequency. In addition, a small correlation peak is observed at ~ −0.4 GHz at this region, representing the magnitude of birefringence, due to the fulfilment of the phase matching condition between the optical pulses that are still orthogonally polarised with each other.

In fact, the measurement result shown in Fig. 5-5 is obtained when the incident optical pulses happen to enter the fibre along its principal axes. In general, the optical pulse cannot be aligned to any particular axis in a SMF, so its polarisation will change randomly along the fibre. Consequently, the obtained signal in two COTDR measurements carries the information about both axes, which are certainly correlated, resulting in a peak at zero

frequency. Besides, another peak representing birefringence will appear randomly and alternatively between Δν and –Δν, depending on how the local phase match condition is fulfilled [141].

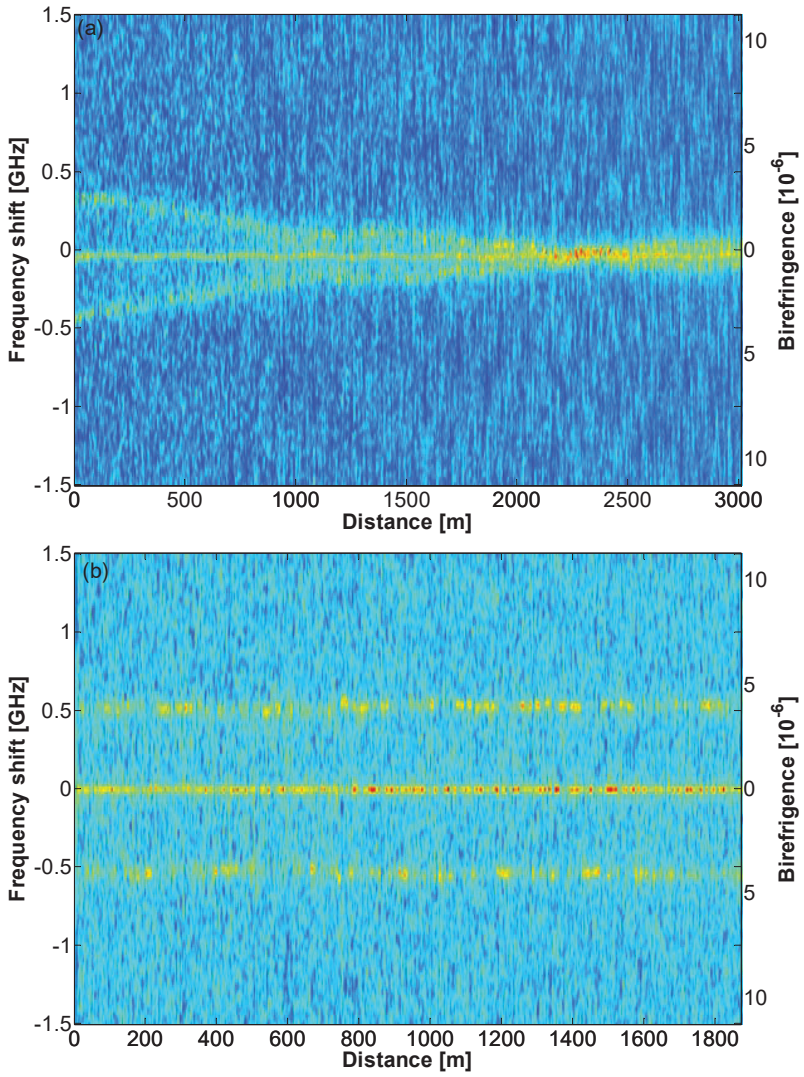

Figure 5-6. Distributed profile of phase birefringence versus distance along (a) a Cabloptic IV and (b) a Philips I SMFs.

Two SMFs, internal denominated Cabloptic IV and Philips I, are tested by the same experiment setup and the results are shown in Fig. 5-6. Three correlated peaks are observed in the correlation spectra for both fibres, one at zero frequency and two peaks at $\pm\Delta\nu$ representing the birefringence. Figure 5-6a shows clear variations of the local birefringence along the fibre, and demonstrates again that the proposed method is able to measure birefringence down to the order of 10^{-6} at ~ 2400 m. The measurement from the backside of the fibre confirms that the birefringence variation of the fibre Cabloptic IV is real and not an experimental artifact. But the birefringence is difficult to be determined because of the randomly alternative appearance of the correlated peaks at $\pm\Delta\nu$.

The central peak shown in Fig. 5-6 is equivalent to the one obtained in a standard COTDR system, which carries the information about laser drifting, temperature and strain variations between two orthogonal measurements. Any changes of these factors between two successive measurements will cause the correlated peaks to shift, resulting in a frequency offset. For example, Fig. 5-6a shows a small negative frequency offset for

the Cabloptic IV fibre. To retrieve the actual birefringence, the birefringence-induced frequency shift must be corrected by this offset. This process becomes more complicated if the influence of the environmental perturbations on birefringence is taken into consideration.

5.1.4 Alternative scheme for measuring standard SMFs

The previous section reveals that it is more difficult to retrieve the birefringence profile in standard or low birefringent fibres by the experimental setup used for PM fibres. A more robust and precise measurement can be obtained by some modification of the setup shown in Fig. 5-1: the polarisation switch and the PC in front of the testing fibre is replaced by a scrambling module in which two orthogonally polarised and phase-decorrelated lightwaves at the same optical frequency combine together to give randomly varying polarisation. In this way, the backscattered Rayleigh trace contains the information from both principal axes of the fibre. So a single measurement is needed in this case; and the birefringence information is retrieved by auto-correlation of the obtained traces. As a result, the impact of laser drifting and environmental perturbations can be greatly suppressed, and the auto-correlation result will present two identical peaks at frequencies $\pm\Delta\nu$.

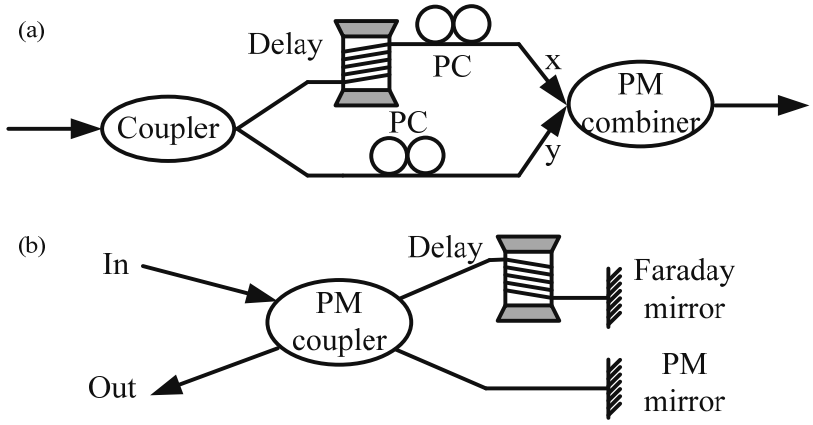

Figure 5-7. Proposed scrambling module to generate two incoherent lightwaves: (a) scheme using an unbalanced Mach-Zehnder interferometer, (b) scheme using a PM mirror and a Faraday mirror. PM: polarisation-maintaining, and PC: polarisation controller.

Two schemes that can realise the light scrambling are shown in Fig. 5-7. An unbalanced Mach-Zehnder interferometer is used in the first scheme, as presented in Fig. 5-7a. The incident light is split into two branches by a coupler and the polarisation in each branch is adjusted by a PC to align to the fast or slow axis of a PM combiner to realise depolarised light. A fibre with certain length needs to be placed in one branch to cause a time delay longer than the coherence time of the light source, so that the light in the two branches will superpose each other incoherently. In the second scheme, the incoming light is also divided into two beams by a PM coupler, as shown in Fig. 5-7b. One beam is reflected by a PM mirror while the other is reflected by a Faraday mirror, so that its polarisation is rotated by 90°. Then the reflected lightwaves are recombined by the PM coupler. Like the first scheme, a delay element is still necessary in one of the branches. In addition, the optical power in both branches must be the same to realise a perfect depolarisation for both schemes.

The coherent Rayleigh traces of the scrambled light are actually a linear incoherent superposition of the backscattered Rayleigh traces that are orthogonally polarised; in other words, this single trace is the combination of light reflected from both fast and slow axes of the fibre, which allows retrieving the birefringence by auto-correlation of the obtained signal.

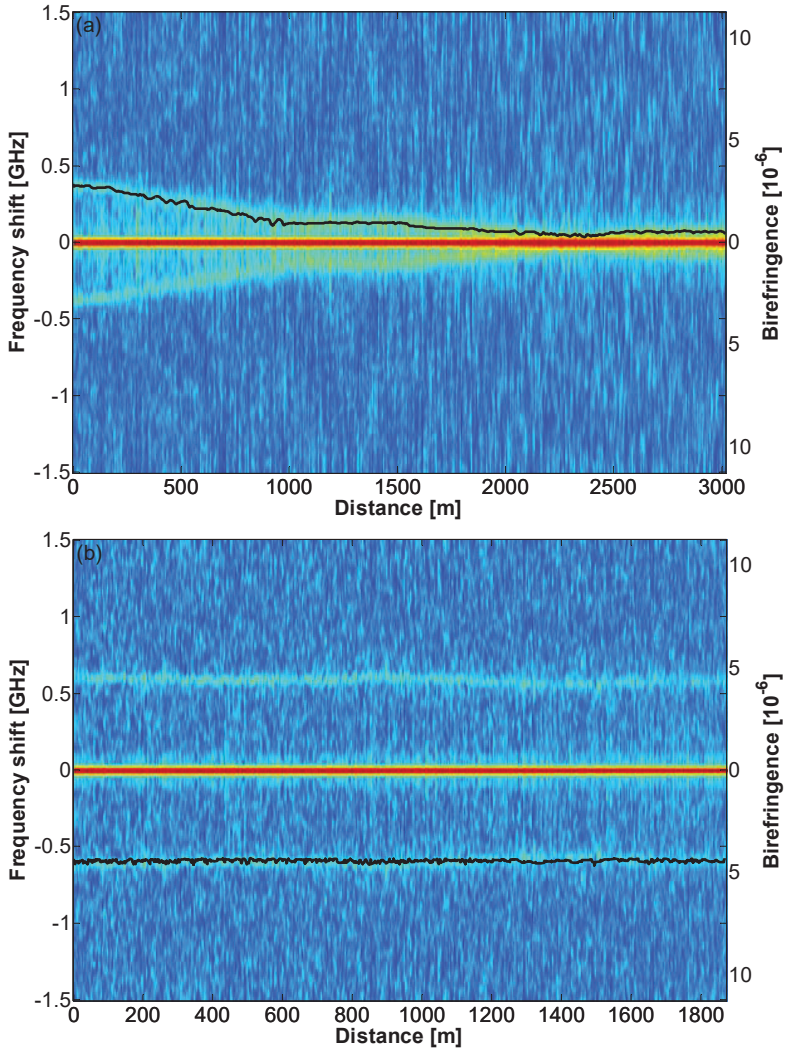

Figure 5-8. Distributed profile of phase birefringence versus distance along a (a) Cableoptic IV and a (b) Philips I SMFs, obtained from the auto-correlation of a single Rayleigh measurement.

Both schemes are used to re-measure the SMFs and the results are shown in Fig. 5-8. The correlation fading, the peak alternative change between frequency $\pm\Delta\nu$ shown in Fig. 5-6, is greatly suppressed by the polarisation scrambled pulses. No long sections with correlation fading are observed in Fig. 5-8 for both fibres. But a mild fading or peak broadening still exists within short fibre sections, which is probably due to the fast birefringence variations within the spatial resolution. As a result, the phase birefringence cannot be retrieved simply by the curve fitting method at specific fibre sections. Therefore, the black lines shown in Fig. 5-8 indicate just the evolution of the phase birefringence along the fibre instead of representing its actual value at every measurement point along the fibre. Experiments achieving cm-resolution are needed in order to realise a precise measurement along the whole fibre.

The fast birefringence variations can be measured by using narrow pulses; however, this method degrades the minimum measured birefringence that is determined by the width of the correlated peak. According to the reported result, the peak width is inversely proportional to the pulse width [106]. As shown in Fig. 5-9, the FWHM of the autocorrelation peak is measured to be ~ 44 MHz, corresponding to a minimum measurable birefringence of 3×10^{-7} for this system when the pulse width is 20 ns. Longer pulses are able to measure even smaller birefringence, but the system is more subjected to the fast birefringence variations in this case.

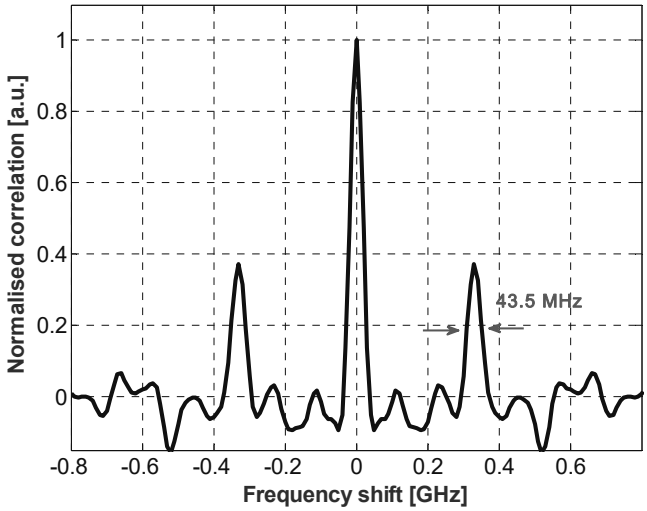

Figure 5-9. Correlation spectrum of Cableoptic IV at a position of 200 m.

5.1.5 Conclusion

A novel distributed birefringence measurement using the COTDR technique is proposed in this section based on the restorability of the coherent Rayleigh trace. It is experimentally validated in high-birefringence fibres and standard SMFs, demonstrating a high precision. In addition, this method becomes more robust by using scrambled light to minimise the impact of environmental perturbations and the laser drifting. Since the measurement is realised in time domain, this system has the potential to retrieve local birefringence over many tens of km of optical fibres with metre-scale spatial resolution.

5.2 Fibre sensing based on the birefringence measurement

Birefringence can be caused by the asymmetry of the fibre cross-section, the asymmetric frozen strains due to the thermal expansion mismatch and the fast quenching during the fibre drawing [145]; however, the impact of these frozen strains can also be modified by environmental quantities such as temperature and strain. For example, Eq. 2-9 shows that the characteristic constant of glass B_m is temperature-dependent, so that temperature variations lead to a birefringence change in PANDA and elliptical core PM fibres. In addition, the axial strain will change the birefringence of PANDA and Bow-Tie fibres due to the difference between compressibility coefficients of the stress-applying area and the surrounding fibre cladding [25]. Consequently, the birefringence change measured by the method proposed in the last section is able to reveal these environmental variations.

Fibre sensing based on the birefringence measurement has been realised using dynamic Brillouin grating [146], OFDR [147] and POTDR technique [148], in which an intermediate sensitivity between Brillouin and Rayleigh sensors is obtained [146]. Besides its comparatively higher sensitivity, this method provides absolute measurements of temperature and strain, which is an advantage over the DFS based on coherent Rayleigh scattering. However, as analysed in the previous section, the generation of BDG requires a precise frequency control of three high power light beams and access to both fibre-ends. And the sensing distance of the OFDR technique is usually limited. On the contrary, the birefringence measurement based on COTDR technique needs just moderate optical power, only one fibre-end and can achieve a much longer sensing distance. Therefore, it is interesting to investigate the sensing performance of the proposed method.

5.2.1 Experiment and results

The experimental setup for the birefringence measurement mentioned above is not the best implementation for sensing because the high sensitivity of the COTDR technique will introduce measurement errors due to the potential environmental perturbations between the consecutive acquisitions of two sets of the coherent Rayleigh traces. Thus the traces from both orthogonal axes must be acquired simultaneously to avoid phase drifts between the two polarisation measurements. Although the depolarisation method is able to retrieve the birefringence in a single measurement, it is difficult to apply this method to the high birefringent fibre in practise, which requires tens of GHz frequency scanning range.

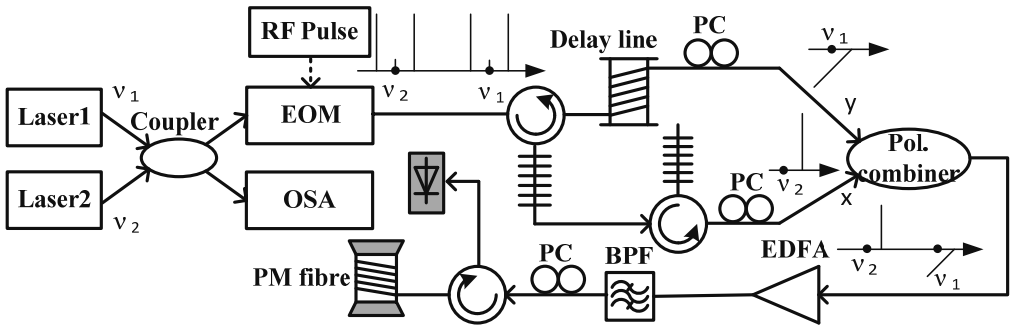

Figure 5-10. Experimental setup for distributed sensing based on birefringence measurement. OSA: optical spectrum analyser, EOM: electro-optic modulator, PM: polarisation maintaining, BPF: band pass filter, EDFA: erbium-doped fiber amplifier, PC: polarisation controller.

An experimental setup to "simultaneously" acquire the Rayleigh trace from two orthogonal axes is shown in Fig. 5-10. Two semiconductor lasers working around 1534 nm are employed for the fast and slow axes, respectively. The optical frequency difference between the lasers is tuned by the driving current to roughly match the birefringence of the PM fibre. The CW light from the two lasers is coupled together. One part of the combined light is detected by a high resolution OSA to monitor the optical frequency of the lasers, while the other part passes through an EOM driven by the RF pulse to realise the frequency sweeping and the conversion of the sidebands into pulses at the same time. In addition, an extremely high extinction ratio can be achieved for the generated optical pulses by this method [149]. Then two FBGs with the spectral width of 5 GHz and 10 GHz are used to select one sideband from each laser. A delay line is placed to one of the selected sidebands in order to temporarily offset the optical pulses at different frequencies, and the delay fibre must be at least twice the length of the sensing fibre. Then, the polarisation of the optical pulses is adjusted by PCs, and pulses are recoupled together by a polarisation combiner. The optical pulses are amplified by an EDFA and an optical bandpass filter is employed to suppress the ASE from the EDFA. A third PC is used to align the orthogonally-polarised pulses to the corresponding axes of the PM fibre. The Rayleigh scattered light is obtained by a 125 MHz photodetector.

The spatial resolution is chosen to be 2 m, corresponding to 20 ns, which is limited by our microwave generator. The frequency scanning range is 2 GHz with 5 MHz step. The obtained trace is averaged 500 times to enhance the SNR, leading to a whole measurement time of ~ 1 min. In order to validate the sensing ability of this technique, a PANDA and an elliptical core PM fibres are tested with the applied temperature or strain change at the last few metres of the fibres. The temperature change are realised by using the same thermal bath used in the COTDR measurement and strain variations are introduced by attaching a short section of the optical fibre to a precise moving stage with an accuracy of 20 μm.

A 100 m long elliptical core PM fibre is tested first. The optical frequency difference of the two lasers is set to be 43.1 GHz according to the measurement result shown in Fig. 5-2a. A ~ 680 m delay line is employed to

offset the optical pulses in the time domain. As a result, the pulse for the fast axis is delayed by ~ 3.4 μs, which can be considered as small enough, thus ensuring that environmental conditions do not change significantly during the acquisition time of traces at the two orthogonal axes.

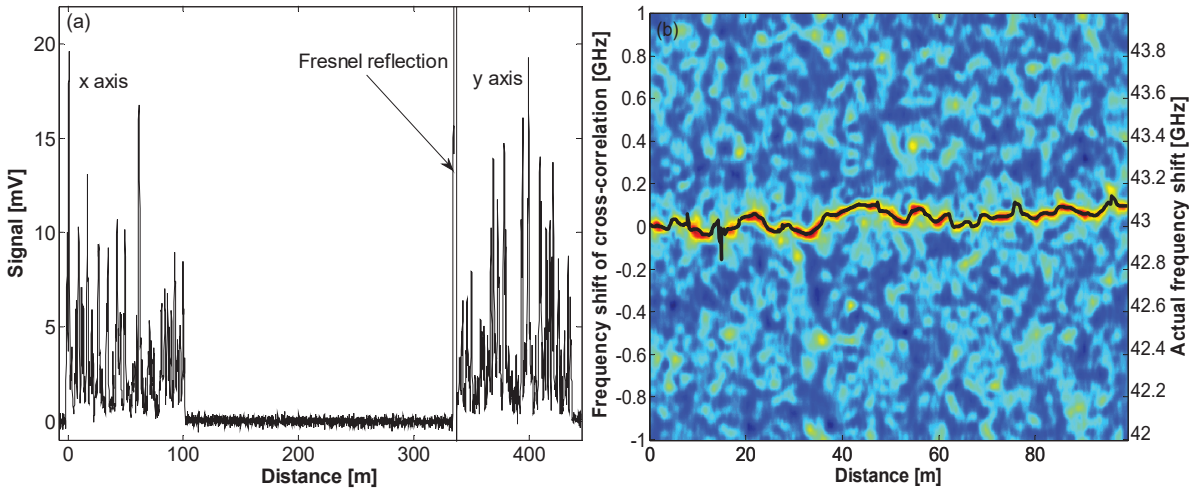

Figure 5-11. (a) Obtained Rayleigh trace for both axes and (b) cross-correlation result of Rayleigh trace.

The obtained Rayleigh traces from orthogonal fibre axes are shown in Fig. 5-11a, and the trace in the fast axis is delay by ~ 340 m, due to the round trip of the optical pulse inside the fibre. The spectral cross-correlation of the Rayleigh traces from both axes is presented in Fig. 5-11b as a function of the distance. The left-hand side vertical axis shows the measurement result of the cross-correlation and the vertical axis on the right-hand shows the actual frequency shift induced by the fibre birefringence. By fitting the correlation peak spectrum with a quadratic curve, the correlation frequency profile is obtained, which is represented by the black line in Fig. 5-11b.

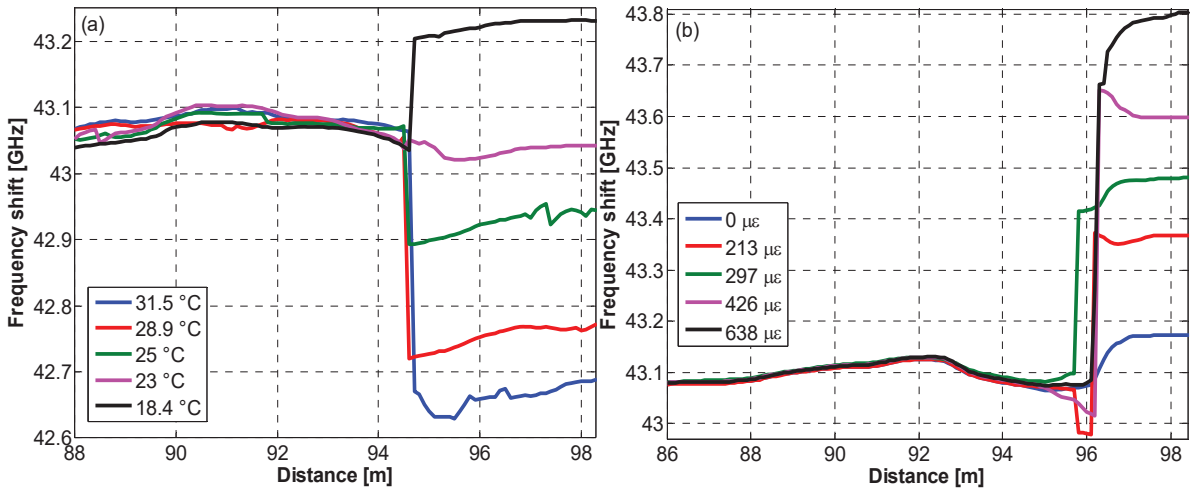

Figure 5-12. Frequency shift versus distance under different (a) temperature and (b) strain conditions for the elliptical core PM fibre.

Then, temperature and strain changes are introduced independently to the far end of the fibre and the distributed profile of the birefringence induced frequency shift is measured under different conditions. The experimental results are shown in Fig. 5-12 for temperature and strain changes, respectively. Obviously, the obtained frequency shift changes due to the environmental variations, demonstrating the ability of the implemented technique to measure temperature and strain. Some fluctuations of the frequency shifts retrieved in

different measurements are observed at the non-sensing part fibre (i.e. up to ~ 94.5 m) in Fig. 5-12a. This is probably due to the thermal perturbations induced by the thermal bath during the experiment and a long temporal interval required between measurements to ensure the thermal stabilisation of the heated fibre section. On the other hand, the strain measurement takes less time, thus minimising the impact of the environmental thermal fluctuations. Hence the obtained frequency shift fluctuates in the range of ±3 MHz, which is lower than the frequency scanning step of 5 MHz.

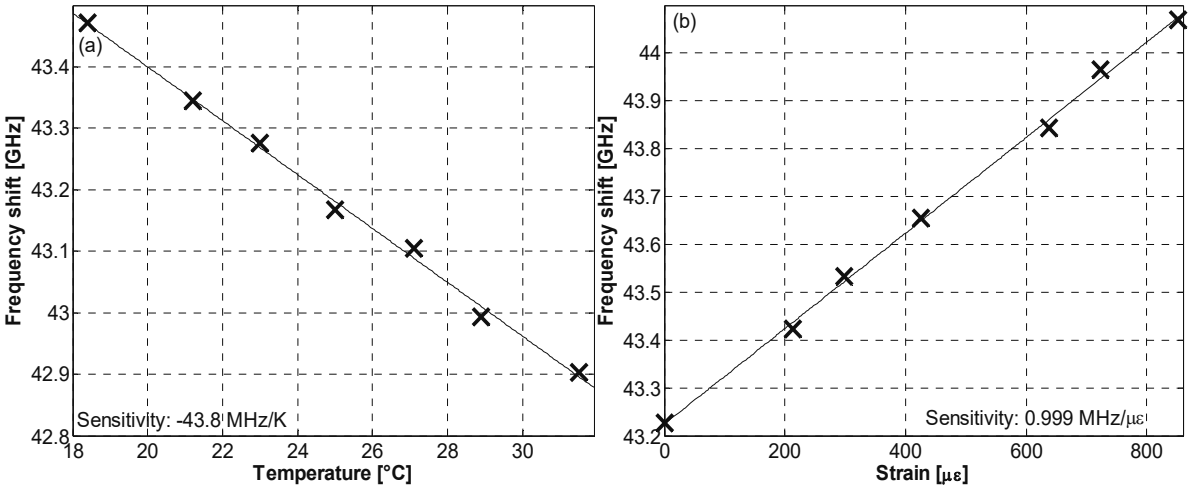

Figure 5-13. Measured frequency shift versus (a) temperature and (b) strain for the elliptical core PM fibre.

The measured frequency shift changes as functions of the applied temperature and strain are plotted respectively in Fig. 5-13a and Fig. 5-13b for the elliptical-core PM fibre. Both figures show a linear dependence of the birefringence on the temperature and strain, while the slopes represent the corresponding sensitivities. The temperature sensitivity is about −44 MHz/K, which is 40 times higher than the sensitivity shown by a standard fibre sensor on Brillouin scattering. And the strain sensitivity reaches ~ 1 MHz/με as shown in Fig. 5-13b, meaning that this technique is ~ 20 times more strain sensitive than a Brillouin sensor.

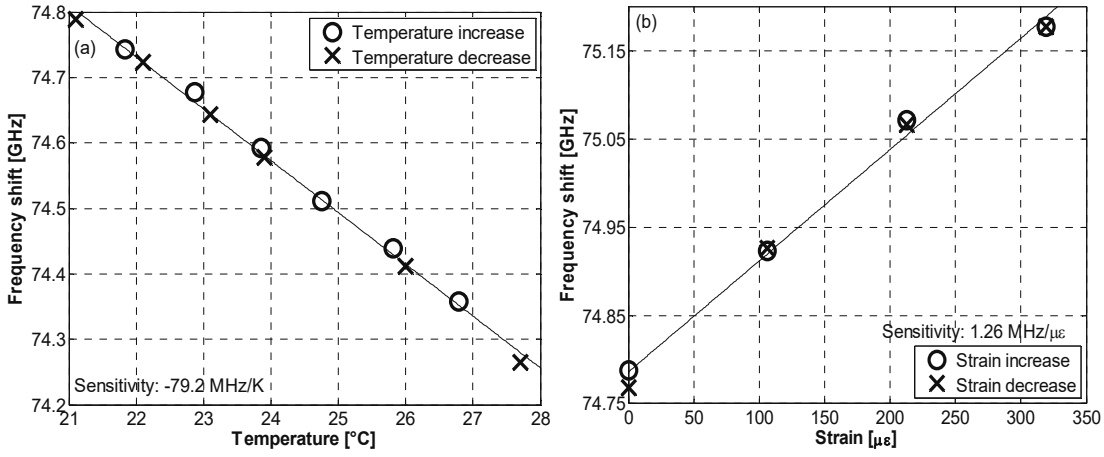

Figure 5-14. Measured frequency shift versus (a) temperature and (b) strain for a PANDA PM fibre.

The same measurement procedure is repeated to obtain the temperature and strain responses of a PANDA PM fibre, which is 20 m long and its birefringence is around 5.6×10^{-4}. The sensing performance is tested in a thermal or strain cycle to demonstrate the robustness of this technique. The temperature and strain sensitivities are shown in Fig. 5-14a and Fig. 5-14b, respectively. The temperature sensitivity roughly scales with the

fractional increase in birefringence, while the strain sensitivity is less enhanced than the simple fractional increase, highlighting the influence of the fibre birefringence design for scaling the temperature response. Only a very small discrepancy can be observed during a thermal or strain cycle, which remains within the uncertainty range of the measurand (given by the noise of the measurement), demonstrating a high repeatability of this technique.

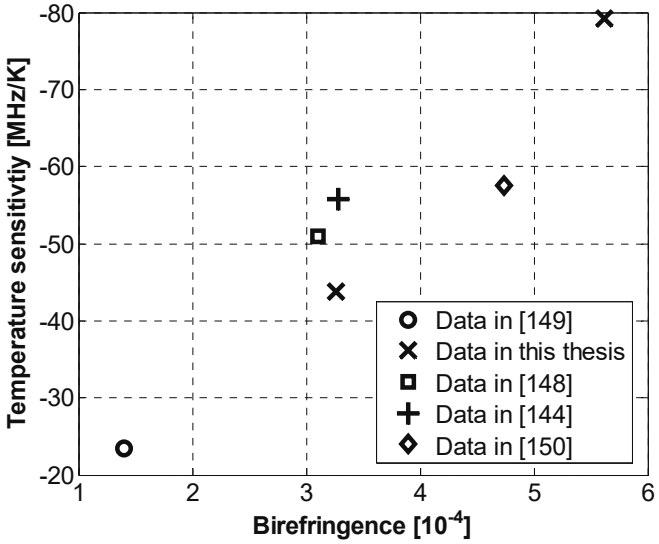

Figure 5-15. Temperature sensitivity measured in PM fibres with different birefringence.

According to Figs. 5-13 and 5-14, the PANDA fibre demonstrates higher sensitivities than the elliptical core fibre, which is probably due to its larger birefringence. Actually, the temperature and strain sensitivities of a PANDA fibre are linearly dependent on its birefringence [146]. Thus fibre sensors with different responses can be realised by designing the fibre birefringence. Figure 5-15 shows the temperature sensitivities obtained in different types of PM fibres with different birefringence [146, 150-152]. It is obvious that sensors tend to be more sensitive when highly birefringent fibres are used. However, the relation between temperature sensitivity and phase birefringence is not linear, because the sensitivity also depends on other factors, such as cladding diameter and coating thickness [152, 153].

5.2.2 Discrimination of temperature and strain

The COTDR sensor demonstrates a very high sensitivity in Chapter 3, but this measurement contains the combined information of the strain and temperature, just like the Brillouin and FBG sensors, making it impossible to discriminate between these two physical quantities. To solve this problem in fibre sensing based on Brillouin scattering, a combination measurement of Brillouin frequency and birefringence has been proposed based on the BDG scheme [146]. The same idea can be applied to the Rayleigh sensor, because the birefringence measurement described above is essentially based on a COTDR scheme, which is much simpler than the BDG implementation. So temperature and strain information is retrieved by a standard COTDR sensor and the birefringence measurement based on a polarisation-resolved COTDR system, as shown in Fig. 5-10.

The obtained frequency shifts in both sensing systems are induced by temperature and strain variations:

$$\begin{bmatrix} \Delta\nu_{COTDR} \\ \Delta\nu_{bire} \end{bmatrix} = \begin{bmatrix} Sen_{T,COTDR} & Sen_{\varsigma,COTDR} \\ Sen_{T,bire} & Sen_{\varsigma,bire} \end{bmatrix} \begin{bmatrix} \Delta T \\ \Delta\zeta \end{bmatrix}, \tag{5-9}$$

where ΔT and $\Delta\zeta$ are the temperature and strain changes, $Sen_{T,COTDR}$ and $Sen_{\zeta,COTDR}$ are the temperature and strain sensitivities of the COTDR sensor, $Sen_{T,bire}$ and $Sen_{\zeta,bire}$ are the temperature and strain sensitivities of the fibre birefringence, $\Delta\nu_{COTDR}$ and $\Delta\nu_{bire}$ are correlation spectral shifts of the COTDR sensor and the birefringence measurement, respectively. So the temperature and strain change can be obtained from a simple inversion of Eq. 5-9:

$$\begin{bmatrix}\Delta T\\ \Delta\zeta\end{bmatrix}=\frac{1}{Sen_{T,COTDR}Sen_{\zeta,bire}-Sen_{\zeta,COTDR}Sen_{T,bire}}\begin{bmatrix}Sen_{\zeta,bire} & -Sen_{\zeta,COTDR}\\ -Sen_{T,bire} & Sen_{T,COTDR}\end{bmatrix}\begin{bmatrix}\Delta\nu_{COTDR}\\ \Delta\nu_{bire}\end{bmatrix}. \tag{5-10}$$

The discrimination can be realised by the experimental setup shown in Fig. 5-9. The birefringence induced frequency shift is obtained by the cross-correlation of coherent Rayleigh traces from orthogonal axes in a single measurement, while $\Delta\nu_{COTDR}$ is calculated based on the cross-correlation of COTDR traces from the same axis between two consecutive measurements.

The 100 m long elliptical core PM fibre tested above is used in this measurement, so $S_{T,bire}$ = −43.8 MHz/K and $S_{\zeta,bire}$ = 0.99 MHz/με as shown in Fig. 5-13. Then the thermal and strain responses of this PM fibre are characterised by a COTDR sensor. For temperature measurement, the method used in Chapter 3 is applied to this fibre, while the far end of the fibre is attached to a moving stage for strain measurement. And the strained fibre section must be thermally isolated because of the high sensitivity of the COTDR sensor.

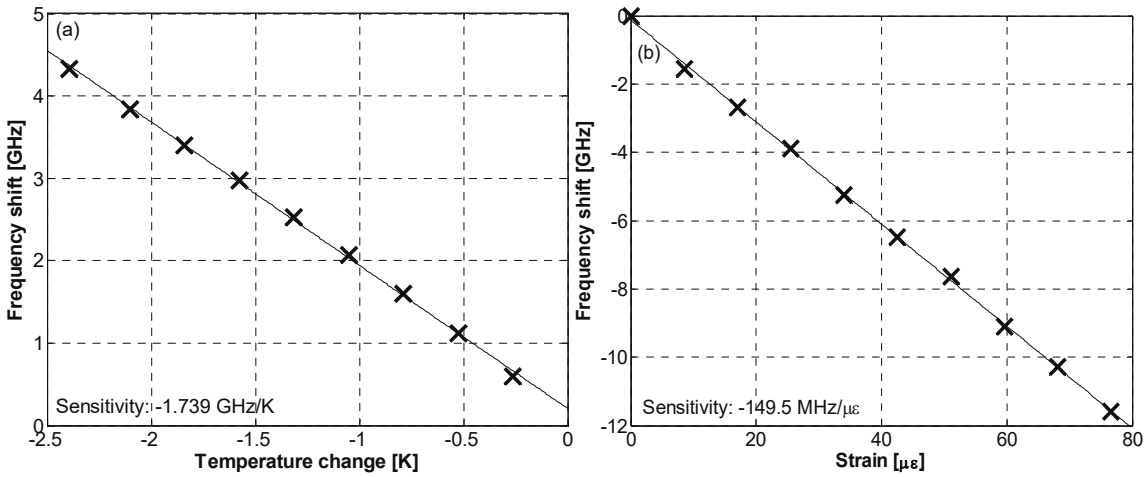

Figure 5-16. (a) Temperature and (b) strain sensitivities of the elliptical-core PM fibre measured by a COTDR sensor.

Figure 5-16 show the frequency shifts under different temperature and strain conditions. The measured temperature sensitivity is higher than expected, which might be explained by doping in the fibre core. On the other hand, the strain sensitivity is almost the same as a standard FBG sensor (−150 MHz/με in Ref. [85]).

In order to reduce the error in the simultaneous evaluation of strain and temperature, a small conditional number is desired [95]. The number associated with Eq. 5-10 is calculated to be ~ 367.9 based on the temperature and strain sensitivities of the COTDR technique and birefringence measurement. And it is much smaller than the conditional number (~ 989.7) using the BDG scheme [146]. Thus the matrix related to sensitivities in Eqs. 5-6 and 5-7 is better conditioned using the method proposed in this thesis than the reported BDG technique, which is probably due to the higher sensitivity of the COTDR sensor.

To demonstrate the discrimination of temperature and strain, the birefringence measurement based on the experimental setup shown in Fig. 5-9 is repeated twice, in-between a temperature variation of 1.9 K and a strain

change of 25.5 με are introduced to the sensing part. Due to the high sensitivity of the COTDR sensor, the frequency scanning range is set as 9 GHz with 10 MHz step.

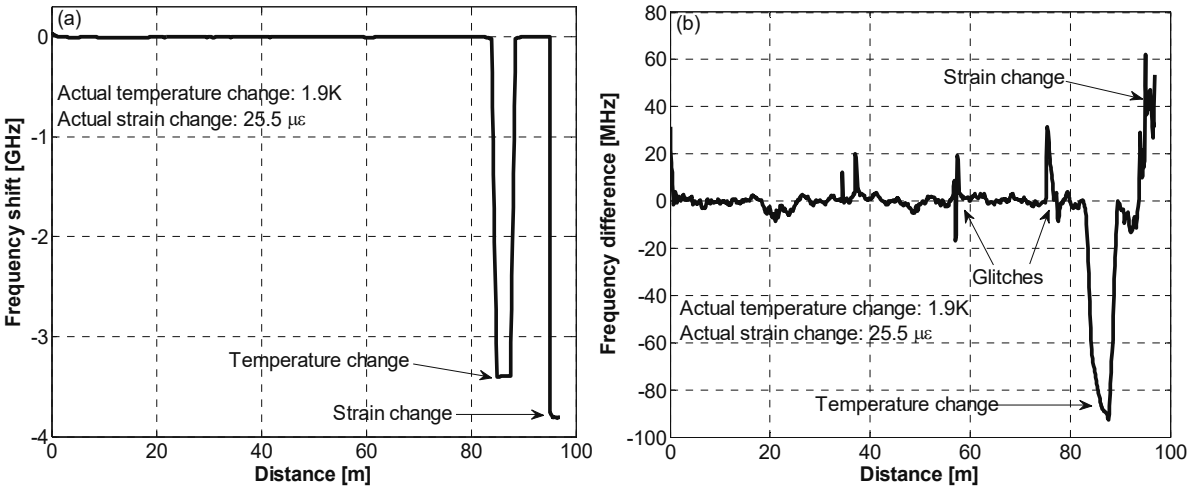

Figure 5-17. (a) Frequency shift obtained from a standard COTDR sensor and (b) frequency difference of birefringence measurements.

The cross-correlation of the coherent Rayleigh traces from slow axis obtained in two measurements provides the frequency shift of the standard COTDR sensor, as shown in Fig. 5-17a. The frequency profile is very clean and two very sharp frequency changes are observed at heated and strained fibre sections. This can be explained by the huge strain and temperature sensitivities of the COTDR sensor. Figure 5-17b shows the frequency difference between two birefringence measurements, representing the longitudinal variations of the fibre birefringence due to the environmental changes. In this case, the obtained frequency profile is noisier than the result obtained by a standard COTDR because of the lower strain and temperature sensitivities of the birefringence. In addition, some spurious, sharp and random peaks shown outside the sensing parts, are observed in Fig. 5-17b, which might be explained by local fast variations of the fibre birefringence with respect to the spatial resolution of 2 m. These fast variations can actually lead to a local broadening of the cross-correlation spectrum, introducing measurement errors.

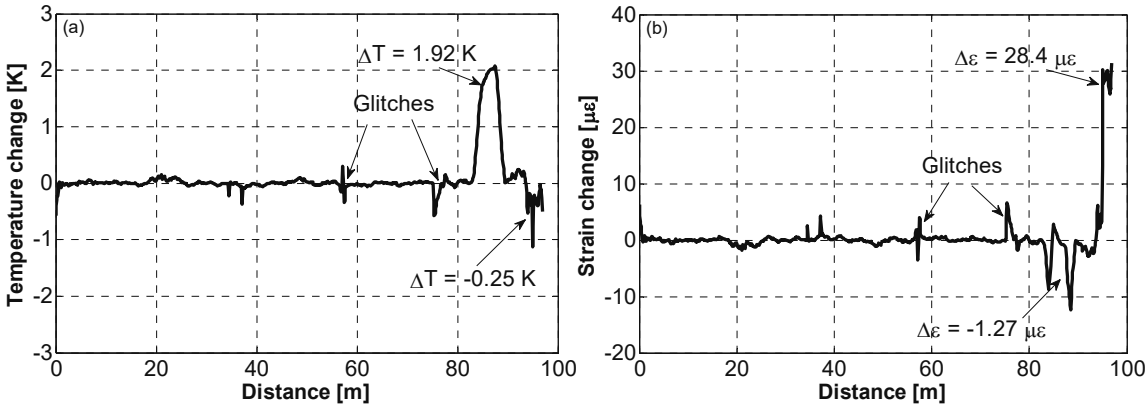

Figure 5-18. Retrieved (a) temperature and (b) strain variation profiles along the elliptical core PM fibre.

Based on the frequency profile shown in Fig. 5-17, the temperature and strain distribution along the fibre can be retrieved using Eq. 5-7. The measured temperature and strain changes are shown in Fig. 5-18a and 5-18b, respectively. Obviously, the temperature and strain can be discriminated by this technique because the

measurement results (1.9 K and 28.4 με) agree very well with the actual temperature and strain changes. But some cross sensitivity is also observed: a temperature change of −0.25 K is obtained at the strained section and a strain variation of −1.3 με at the heated part. This is eventually attributed to the measurement error of the birefringence measurement. Actually, the obtained temperature and strain profiles present noise and glitches in the birefringence measurement. Thus the error of this discrimination method is determined by the noise in the birefringence measurement. In addition, two peaks in the strain profile can be observed along the heated fibre section, due to the transitions of the temperature measurement with 2 m spatial resolution. As a result, short pulses are necessary to suppress spurious residual peaks and realise a more precise determination of temperature and strain.

5.2.3 Conclusion

It is experimentally demonstrated that the distributed birefringence measurement based on the COTDR technique is suitable for temperature and strain sensing, offering a higher sensitivity than that of a Brillouin fibre sensor and the absolute value, which is an advantage over the COTDR sensor. In addition, a PANDA and an elliptical core PM fibres give different sensitivities, revealing the fact that the sensitivity can be designed by tailoring the fibre birefringence.

Simultaneous temperature and strain sensing is experimentally realised by combining the birefringence measurement and the COTDR technique, and the measurement errors are essentially determined by the uncertainty on the birefringence measurement.

Chapter 6

Conclusions and Perspectives

Currently, the research on fibre sensing is strongly stimulated by the industrial demand, such as high precision, low cost and multiple applications. Generally speaking, a point sensor is able to realise a more precise measurement due to its higher sensitivity, but the cost of distributed sensors is lower per sensing point when a large number of points is measured. In phase with this research trend, fibre sensors based on coherent Rayleigh scattering have been investigated in this thesis, since they accumulate the advantages of distributed sensors (large number of sensing points) and point sensors (high sensitivity). Hence this fibre sensor meets the industrial requirements and has the potential to be applied to the distributed measurements requiring high precision. In addition, the COTDR technique has been applied to retrieve the birefringence profile along fibres, achieving a simultaneous discriminated measurement of temperature and strain.

6.1 Main contributions

The core of this thesis is the investigation of distributed sensing based on the COTDR technique leading to the analysis of several related problems. It has been experimentally confirmed the high temperature and strain sensitivities, and a temperature resolution in the milli-Kelvin range, even at cryogenic temperatures. Furthermore, this technique is applied to retrieve the distribution of phase birefringence along PM fibres and old SMFs. A novel distributed sensor is proposed based on the birefringence measurement, which can remove solve the cross-sensitivity of temperature and strain in connection with a standard COTDR sensing technique.

- Thus the temperature sensitivity of a COTDR sensor is calculated based on the FBG sensing theory over a wide temperature range from 300 K to 4.5 K and the theoretical result turns to be 2~3 orders of magnitude higher than the sensitivity of a fibre sensor based Brillouin scattering. Such a high sensitivity is experimentally validated at ambient and cryogenic temperatures. In addition, the temperature resolution is found to be in the milli-Kelvin scale even at liquid Nitrogen temperatures. Consequently, the COTDR technique has an advantage in highly precise distributed sensing, moreover under cryogenic conditions. But this method only provides a relative value instead of an absolute measurement.

- The high temperature sensitivity of the COTDR sensor designates this technique to measure very small refractive index changes induced by temperature variations. Therefore, this novel sensor also has the ability to measure the index difference between the two principal birefringence axes in the fibre. The set-up based on the COTDR technique has successfully retrieved the phase birefringence profile along highly-birefringent and standard optical fibres of a precision in the order of 10^{-7}. The minimum measurable birefringence depends on the incident optical pulse width, which can be further improved at the expense of spatial resolution.

- Birefringence measurements based on coherent Rayleigh scattering are intrinsically capable of sensing environmental changes because the birefringence turns out to depend on temperature and strain. Such distributed temperature and strain measurements are realised along a PANDA and an elliptical core PM fibres. The obtained sensitivities are tens of times higher than the corresponding value for a standard DFS based on Brillouin scattering. Although the same idea can be also be realised by a Brillouin dynamic grating, the birefringence measurement based on the COTDR technique is much simpler to implement and requires the access to a single end.

- The temporal and spectral characteristics of the coherent Rayleigh trace have been investigated in order to find the minimum detection bandwidth required by a given COTDR system. Due to the random distribution of the refractive index along the fibre, the coherent Rayleigh scattering is assimilated to a random walk process. Hence the statistical properties of a coherent Rayleigh trace are analysed based on the random walk theory. The amplitude and intensity of the coherent backscattered light obey a Rayleigh and an exponential distributions, respectively, which is in excellent agreement with the reported results. In addition, the spectrum of the COTDR trace is investigated theoretically and experimentally, and it shows a tight dependence on the incident pulse shape. The amplitude spectrum is the same as the pulse amplitude spectrum and the corresponding intensity spectrum is the self-convolution of the amplitude spectrum. By analysing the statistical features and the visibility of the COTDR intensity trace filter by different bandwidth, the minimum 3-dB bandwidth of a photodetector has to satisfy the condition to be twice larger than that of the incident rectangular pulse spectrum.

- The impacts of fibre coating and birefringence on the sensitivity of different DFSs are explored in the process of analysing their sensing performance, so that a sensitivity scaling can be realised. The thermally induced strain in the coating can improve the temperature sensitivity, which has been validated in a COTDR and a BOTDA sensor. Furthermore, the sensitivity of a DFS based on the measurement of birefringence turns to be roughly proportional to the fibre birefringence. This result paves the way to a possible future tailoring of the sensitivity by different birefringence and/or coating design.

6.2 Future work

The COTDR technique has already been applied to intrusion monitoring and vibration measurement. In this thesis, this method demonstrates its extremely high sensitivity, superior measurand resolution and excellent performance even under harsh working conditions for distributed temperature and strain sensing. Consequently, the COTDR sensor shows a broader application area than the DFSs based on Brillouin and Raman scatterings. However the performance of the COTDR system is still limited by the interrelation of sensing distance, spatial resolution, measurand resolution and measurement time, like any other distributed sensors, which needs further investigations. Moreover, there are some special aspects in COTDR sensing to be further studied due to the random interference process.

- Despite the wide application area of the COTDR sensor, the quality of a coherent Rayleigh trace is still difficult to define due to its spiky shape. In a DFS based on Brillouin and Raman scatterings, the quality of the obtained trace is usually quantified by its SNR. But the signal power in a COTDR sensor is difficult to determine because the obtained signal is a random variable. It is true that the concept of trace quality is not very important in vibration sensing, which cares more about the trace variations among different measurements, but it is supposed to play the main role in determining the measurand error, like in a Brillouin sensor [105]. The visibility used in this thesis can only evaluate the trace contrast, which is not enough to represent the trace quality. In this

case, the quality of a COTDR trace may be determined in the same way as to evaluate a speckle image [154], which can also be assimilated to a random walk process.

- The high sensitivity of the COTDR sensor requires a broad frequency scanning range, which not only increase measurement time and cost but also makes the sensor more vulnerable to environmental perturbations. This will actually result in more measurement errors for the method presented in this thesis. A possible way to overcome this problem is to reduce the sensitivity. Although many methods have been proposed to enhance the sensitivity, few researches focus on the desensitisation of the distributed sensors, because the thermal response of the DFS depends on different physical processes that are intrinsically difficult to change.

- The COTDR technique can realise phase birefringence measurements along old SMFs, but it fails in the evaluation of current standard SMFs, in which the birefringence is possibly below 10^{-7} range. This is probably due to spinning drawing of the fibre, resulting in the fast rotation of the polarisation axes in the fibre. Hence, a spatial resolution smaller than the rotation period should be realised in this case, but this will degrade the measurement accuracy. Consequently, it is worth analysing the relation of the measurable rotation period and the birefringence resolution in the measurement.

- Recently, the image processing method has been applied to enhance the performance of white-noise-limited distributed fibre sensors, which are based on Brillouin and Raman scatterings [155]. It is interesting to investigate the possible application of this method to COTDR sensors, which might be correlation-noise-limited in temperature and strain sensing.

Appendix

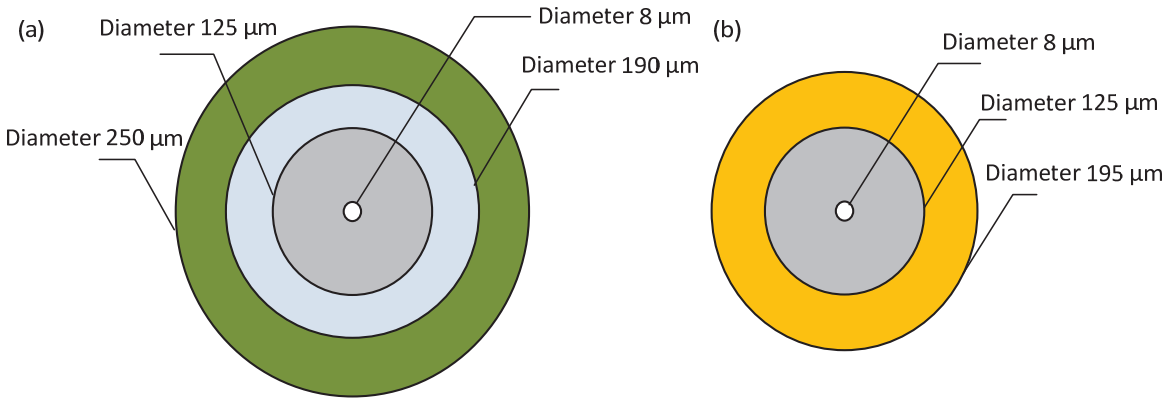

Figure A-1. Cross-section of (a) a standard SMF and (b) a ORMOCER® coated SMF.

	Standard SMF	ORMOCER® coated SMF
Thermal expansion of silica	0.45×10^{-6} K^{-1} @ 25 °C	
Young's modulus of silica	70 GPa @ 25 °C	
Thermo-optic coefficient of silica	8.36×10^{-6} K^{-1} (Sellmeier model) 9.31×10^{-6} K^{-1}(Quartic model)	@ 25 °C
Thermal expansion of coating	Primary: 6.34×10^{-4} K^{-1} (25 to −50 °C)	1.23×10^{-4} K^{-1}
	Secondary: 2.38×10^{-4} K^{-1} (25 to −100 °C)	
Young's modulus of coating	Primary: 10 MPa @ 25 °C 1 GPa @ −50 °C	1.5 GPa @ 25 °C
	Secondary: 1.3 GPa @ 25 °C	

Table A-1. Thermal and mechanical information of the standard and ORMOCER® coated SMF.

Bibliography

[1] K. C. Kao and G. A. Hockham, "Dielectric-fibre surface waveguides for optical frequencies," *Proceedings of the Institution of Electrical Engineers,* vol. 113, pp. 1151-1158, 1966.

[2] B. Culshaw and A. Kersey, "Fiber-optic sensing: a historical perspective," *Journal of Lightwave Technology,* vol. 26, pp. 1064-1078, 2008.

[3] F. Yu and S. Yin, *Fiber Optic Sensors*: Marcel Dekker, p. 1, 130, 132, 2002.

[4] D. Krohn, "Know your market," *Nature Photonics,* vol. 4, pp. 436-436, 2010.

[5] M. Nazarathy, S. A. Newton, R. P. Giffard, D. S. Moberly, F. Sischka, W. R. Trutna*, et al.*, "Real-time long range complementary correlation optical time domain reflectometer," *Journal of Lightwave Technology,* vol. 7, pp. 24-38, 1989.

[6] H. F. Taylor and C. E. Lee, "Apparatus and method for fiber optic intrusion sensing," Pantent Number: US5194847A, 1993.

[7] L. Palmieri and L. Schenato, "Distributed optical fiber sensing based on Rayleigh scattering," *The Open Optics Journal,* vol. 7, pp. 104-127, 2013.

[8] A. Denisov, M. A. Soto, and L. Thevenaz, "Going beyond 1000000 resolved points in a Brillouin distributed fiber sensor: theoretical analysis and experimental demonstration," *Light Science & Application,* vol. 5, p. e16074, 2016.

[9] X. Angulo-Vinuesa, S. Martin-Lopez, J. Nuño, P. Corredera, J. D. Ania-Castañon, L. Thévenaz*, et al.*, "Raman-assisted Brillouin distributed temperature sensor over 100 km featuring 2 m resolution and 1.2 C uncertainty," *Journal of Lightwave Technology,* vol. 30, pp. 1060-1065, 2012.

[10] Z. Xie, L. Xia, Y. Wang, C. Yang, C. Cheng, and D. Liu, "Fiber Fault Detection With High Accuracy Using Chaotic Signal From an SOA Ring Reflectometry," *IEEE Photonics Technology Letters,* vol. 25, pp. 709-712, 2013.

[11] Y. Koyamada, E. Yousuke, S. Hirose, S. Nakamura, and K. Hogari, "Novel fiber-optic distributed strain and temperature sensor with very high resolution," *IEICE Transactions on Communications,* vol. 89, pp. 1722-1725, 2006.

[12] M. K. Barnoski and S. M. Jensen, "Fiber waveguides: a novel technique for investigating attenuation characteristics," *Applied Optics,* vol. 15, pp. 2112-2115, 1976.

[13] C. F. Bohren and D. R. Huffman, *Absorption and Scattering of Light by Small Particles*: John Wiley & Sons, p., 2008.

[14] A. J. Rogers, "Polarization-optical time domain reflectometry: a technique for the measurement of field distributions," *Applied Optics,* vol. 20, pp. 1060-1074, 1981.

[15] J. Park and H. F. Taylor, "Fiber optic intrusion sensor using coherent optical time domain reflectometer," *Japanese Journal of Applied Physics,* vol. 42, p. 3481, 2003.

[16] A. Hartog, A. Leach, and M. Gold, "Distributed temperature sensing in solid-core fibres," *Electronics Letters,* vol. 21, pp. 1061-1062, 1985.

[17] T. Kurashima, T. Horiguchi, H. Izumita, S. Furukawa, and Y. Koyamada, "Brillouin optical-fiber time domain reflectometry," *IEICE Transactions on Communications,* vol. 76, pp. 382-390, 1993.

[18] B. E. Saleh and M. C. Teich, *Fundamentals of Photonics*: Wiley New York, p. 152, 2007.

[19] R. Boyd, *Nonlinear Optics*: Academic Press, p. 2, 4, 72, 394, 406, 412, 413, 438,439,, 2008.

[20] R. Loudon, *the Quantum Theory of Light*: OUP Oxford, p. 98, 2000.

[21] G. R. Fowles, *Introduction to Modern Optics*: Courier Corporation, p. 69, 2012.

[22] A. Galtarossa and C. R. Menyuk, *Polarization Mode Dispersion* vol. 1: Springer Science & Business Media, p. 1,2,4, 2006.

[23] A. Rogers, *Polarization in Optical Fibers*: Artech House, p. 7-8, 2008.

[24] A. Mendez and T. F. Morse, *Specialty Optical Fibers Handbook*: Academic Press, p. 115-116, 252-254, 2007.

[25] T. R. Woliński, "Polarimetric optical fibers and sensors," in *Progress in Optics*. vol. Volume 40, E. Wolf, Ed., ed: Elsevier, 2000, p. 23.

[26] J. Noda, K. Okamoto, and Y. Sasaki, "Polarization-maintaining fibers and their applications," *Journal of Lightwave Technology,* vol. 4, pp. 1071-1089, 1986.
[27] R. B. Miles, W. R. Lempert, and J. N. Forkey, "Laser rayleigh scattering," *Measurement Science and Technology,* vol. 12, p. R33, 2001.
[28] P. W. Milonni and J. H. Eberly, *Lasers*: Wiley, p. 35, 48, 50, 1988.
[29] I. L. Fabelinskii, *Molecular Scattering of Light*: Springer Science & Business Media, p. 23, 2012.
[30] S. Foaleng Mafang, "Brillouin Echoes for Advanced Distributed Sensing in Optical Fibres," Doctoral dissertation, p. 16, École Polytechnique Fédérale de Lausanne, 2011.
[31] L. Thévenaz, *Advanced Fiber Optics: Concepts and Technology*: EPFL Press, p. 265, 268, 2011.
[32] A. Hartog and M. Gold, "On the theory of backscattering in single-mode optical fibers," *Journal of Lightwave Technology,* vol. 2, pp. 76-82, 1984.
[33] W. Zhi, R. Guobin, L. Shuqin, and J. Shuisheng, "Loss properties due to Rayleigh scattering in different types of fiber," *Optics Express,* vol. 11, pp. 39-47, 2003.
[34] R. Hui and M. O'Sullivan, *Fiber Optic Measurement Techniques*: Academic Press, p. 386, 2009.
[35] A. Hartog, "A distributed temperature sensor based on liquid-core optical fibers," *Journal of Lightwave Technology,* vol. 1, pp. 498-509, 1983.
[36] A. A. Boiarski, G. Pilate, T. Fink, and N. Nilsson, "Temperature measurements in power plant equipment using distributed fiber optic sensing," *IEEE Transactions on Power Delivery,* vol. 10, pp. 1771-1778, 1995.
[37] Z. Zhang and X. Bao, "Distributed optical fiber vibration sensor based on spectrum analysis of Polarization-OTDR system," *Optics Express,* vol. 16, pp. 10240-10247, 2008.
[38] J. N. Ross, "Measurement of magnetic field by polarisation optical time-domain reflectometry," *Electronics Letters,* vol. 17, pp. 596-597, 1981.
[39] L. Palmieri, D. Sarchi, and A. Galtarossa, "Distributed measurement of high electric current by means of polarimetric optical fiber sensor," *Optics Express,* vol. 23, pp. 11073-11079, 2015.
[40] P. Healey, "Fading in heterodyne OTDR," *Electronics Letters,* vol. 20, pp. 30-32, 1984.
[41] K. Shimizu, T. Horiguchi, and Y. Koyamada, "Characteristics and reduction of coherent fading noise in Rayleigh backscattering measurement for optical fibers and components," *Journal of Lightwave Technology,* vol. 10, pp. 982-987, 1992.
[42] H. Izumita, S. i. Furukawa, Y. Koyamada, and I. Sankawa, "Fading noise reduction in coherent OTDR," *IEEE Photonics Technology Letters,* vol. 4, pp. 201-203, 1992.
[43] Y. Koyamada, M. Imahama, K. Kubota, and K. Hogari, "Fiber-optic distributed strain and temperature sensing with very high measurand resolution over long range using coherent OTDR," *Journal of Lightwave Technology,* vol. 27, pp. 1142-1146, 2009.
[44] M. S. Maughan, H. H. Kee, and P. T. Newson, "Simultaneous distributed fibre temperature and strain sensor using microwave coherent detection of spontaneous Brillouin backscatter," *Measurement Science and Technology,* vol. 12, pp. 834-842, 2001.
[45] P. C. Wait, K. De Souza, and T. P. Newson, "A theoretical comparison of spontaneous Raman and Brillouin based fibre optic distributed temperature sensors," *Optics Communications,* vol. 144, pp. 17-23, 1997.
[46] L. Thevenaz, A. Fellay, M. Facchini, W. Scandale, M. Nikles, and P. A. Robert, "Brillouin optical fiber sensor for cryogenic thermometry," in *9th Annual International Symposium on Smart Structures and Materials,*, 2002, pp. 22-27.
[47] R. Vacher and J. Pelous, "Behavior of thermal phonons in amorphous media from 4 to 300 K," *Physical Review B,* vol. 14, pp. 823-828, 1976.
[48] F. Galeener, J. Mikkelsen Jr, R. H. Geils, and W. Mosby, "The relative Raman cross sections of vitreous SiO2, GeO2, B2O3, and P2O5," *Applied Physics Letters,* vol. 32, pp. 34-36, 1978.
[49] A. M. Soto, "Advanced techniques for distributed optical fiber sensors based on Raman and Brillouin scattering," Doctor Doctoral dissertation, p. 63, Scuola Superiore Sant'Anna Pisa di Studi Universitari e di Perfezionamento, 2011.
[50] M. Balkanski, R. F. Wallis, and E. Haro, "Anharmonic effects in light scattering due to optical phonons in silicon," *Physical Review B,* vol. 28, pp. 1928-1934, 1983.
[51] G. P. Agrawal, *Nonlinear Fiber Optics*: Academic press, p. 15, 397-398, 2007.
[52] R. H. Stolen and C. Lin, "Self-phase-modulation in silica optical fibers," *Physical Review A,* vol. 17, pp. 1448-1453, 1978.
[53] S. M. Foaleng, F. Rodríguez-Barrios, S. Martin-Lopez, M. González-Herráez, and L. Thévenaz, "Detrimental effect of self-phase modulation on the performance of Brillouin distributed fiber sensors," *Optics Letters,* vol. 36, pp. 97-99, 2011.

[54] M. N. Alahbabi, Y. T. Cho, T. P. Newson, P. C. Wait, and A. H. Hartog, "Influence of modulation instability on distributed optical fiber sensors based on spontaneous Brillouin scattering," *Journal of the Optical Society of America B,* vol. 21, pp. 1156-1160, 2004.

[55] H. F. Martins, S. Martin-Lopez, P. Corredera, P. Salgado, O. Frazão, and M. González-Herráez, "Modulation instability-induced fading in phase-sensitive optical time-domain reflectometry," *Optics Letters,* vol. 38, pp. 872-874, 2013.

[56] M. González Herráez, L. Thévenaz, and P. Robert, "Distributed measurement of chromatic dispersion by four-wave mixing and Brillouin optical-time-domain analysis," *Optics Letters,* vol. 28, pp. 2210-2212, 2003.

[57] A. Motil, A. Bergman, and M. Tur, "State of the art of Brillouin fiber-optic distributed sensing," *Optics & Laser Technology,* vol. 78, Part A, pp. 81-103, 2016.

[58] J. Urricelqui, M. Sagues, and A. Loayssa, "Brillouin optical time-domain analysis sensor assisted by Brillouin distributed amplification of pump pulses," *Optics Express,* vol. 23, pp. 30448-30458, 2015.

[59] Z. N. Wang, J. Li, M. Q. Fan, L. Zhang, F. Peng, H. Wu*, et al.*, "Phase-sensitive optical time-domain reflectometry with Brillouin amplification," *Optics Letters,* vol. 39, pp. 4313-4316, 2014.

[60] C. Headley and G. Agrawal, *Raman Amplification in Fiber Optical Communication Systems*: Academic Press, p. 1, 2005.

[61] H. Martins, S. Martin-Lopez, P. Corredera, M. L. Filograno, O. Frazao, and M. Gonzalez-Herraez, "Phase-sensitive optical time domain reflectometer assisted by first-order raman amplification for distributed vibration sensing over > 100 km," *Journal of Lightwave Technology,* vol. 32, pp. 1510-1518, 2014.

[62] S. Martin-Lopez, M. Alcon-Camas, F. Rodriguez, P. Corredera, J. D. Ania-Castañon, L. Thévenaz*, et al.*, "Brillouin optical time-domain analysis assisted by second-order Raman amplification," *Optics express,* vol. 18, pp. 18769-18778, 2010.

[63] A. Yariv, H. Blauvelt, and S. W. Wu, "A reduction of interferometric phase-to-intensity conversion noise in fiber links by large index phase modulation of the optical beam," *Journal of Lightwave Technology,* vol. 10, pp. 978-981, 1992.

[64] D. Marcuse, *Principles of Optical Fiber Measurements*: Academic Press, p. 51, 1981.

[65] J. Zhou, Z. Pan, Q. Ye, H. Cai, R. Qu, and Z. Fang, "Characteristics and explanations of interference fading of a φ-OTDR with a multi-frequency source," *Journal of Lightwave Technology,* vol. 31, pp. 2947-2954, 2013.

[66] R. K. Staubli and P. Gysel, "Crosstalk penalities due to coherent Rayleigh noise in bidirectional optical communication systems," *Journal of Lightwave Technology,* vol. 9, pp. 375-380, 1991.

[67] W. Burns and R. Moeller, "Rayleigh backscattering in a fiber gyroscope with limited coherence sources," *Journal of Lightwave Technology,* vol. 1, pp. 381-386, 1983.

[68] J. W. Goodman, *Speckle phenomena in optics: theory and applications*: Roberts and Company Publishers, p. 8, 12, 2007.

[69] J. C. Dainty, *Laser speckle and related phenomena* vol. 9: Springer Science & Business Media, p. 14, 2013.

[70] J. W. Goodman, *Statistical optics*: John Wiley & Sons, p. 25, 71-73, 2000.

[71] R. K. Staubli and P. Gysel, "Statistical properties of single-mode fiber Rayleigh backscattered intensity and resulting detector current," *IEEE Transactions on Communications,* vol. 40, pp. 1091-1097, 1992.

[72] P. Healey, "Statistics of Rayleigh backscatter from a single-mode optical fibre," *Electronics Letters,* vol. 21, pp. 226-228, 1985.

[73] H. F. Martins, S. Martin-Lopez, P. Corredera, M. L. Filograno, O. Frazao, and H. M. Gonzalez, "Coherent noise reduction in high visibility phase-sensitive optical time domain reflectometer for distributed sensing of ultrasonic waves," *Journal of Lightwave Technology,* vol. 31, pp. 3631-3637, 2013.

[74] L. B. Liokumovich, N. A. Ushakov, O. I. Kotov, M. A. Bisyarin, and A. H. Hartog, "Fundamentals of optical fiber sensing schemes based on coherent optical time domain reflectometry: signal model under static fiber conditions," *Journal of Lightwave Technology,* vol. 33, pp. 3660-3671, 2015.

[75] A. Alekseev, V. Vdovenko, B. Gorshkov, V. Potapov, and D. Simikin, "A phase-sensitive optical time-domain reflectometer with dual-pulse diverse frequency probe signal," *Laser Physics,* vol. 25, p. 065101, 2015.

[76] P. Healey, "Instrumentation principles for optical time domain reflectometry," *Journal of Physics E: Scientific Instruments,* vol. 19, p. 334, 1986.

[77] P. Gysel and R. K. Staubli, "Spectral properties of Rayleigh backscattered light from single-mode fibers caused by a modulated probe signal," *Journal of Lightwave Technology,* vol. 8, pp. 1792-1798, 1990.

[78] I. Reed, "On a moment theorem for complex Gaussian processes," *IRE Transactions on Information Theory,* vol. 3, pp. 194-195, 1962.
[79] B. Moslehi, "Noise power spectra of optical two-beam interferometers induced by the laser phase noise," *Journal of Lightwave Technology* vol. 4, pp. 1704-1710, 1986.
[80] E. Ip, A. P. T. Lau, D. J. Barros, and J. M. Kahn, "Coherent detection in optical fiber systems," *Optics Express,* vol. 16, pp. 753-791, 2008.
[81] M. A. Soto, G. Bolognini, and F. D. Pasquale, "Long-range simplex-coded BOTDA sensor over 120km distance employing optical preamplification," *Optics Letters,* vol. 36, pp. 232-234, 2011.
[82] D. Mermelstein, E. Shacham, M. Biton, and S. Sternklar, "Brillouin amplification and processing of the Rayleigh scattered signal," *Optics Letters,* vol. 40, pp. 3340-3343, 2015.
[83] Z. Wang, L. Zhang, S. Wang, N. Xue, F. Peng, M. Fan*, et al.*, "Coherent ϕ-OTDR based on I/Q demodulation and homodyne detection," *Optics Express,* vol. 24, pp. 853-858, 2016.
[84] J. C. Juarez, E. W. Maier, K. N. Choi, and H. F. Taylor, "Distributed fiber-optic intrusion sensor system," *Journal of Lightwave Technology,* vol. 23, p. 2081, 2005.
[85] A. D. Kersey, M. A. Davis, H. J. Patrick, M. LeBlanc, K. Koo, C. Askins*, et al.*, "Fiber grating sensors," *Journal of Lightwave Technology,* vol. 15, pp. 1442-1463, 1997.
[86] B. H. Lee, Y. H. Kim, K. S. Park, J. B. Eom, M. J. Kim, B. S. Rho*, et al.*, "Interferometric fiber optic sensors," *Sensors,* vol. 12, pp. 2467-2486, 2012.
[87] M. A. Muriel and A. Carballar, "Internal field distributions in fiber Bragg gratings," *IEEE Photonics Technology Letters,* vol. 9, pp. 955-957, 1997.
[88] E. S. d. L. Filho, M. D. Baiad, M. Gagné, and R. Kashyap, "Fiber Bragg gratings for low-temperature measurement," *Optics Express,* vol. 22, pp. 27681-27694, 2014.
[89] M. Imahama, Y. Koyamada, and K. Hogari, "Restorability of Rayleigh backscatter traces measured by coherent OTDR with precisely frequency-controlled light source," *IEICE Transactions on Communications,* vol. 91, pp. 1243-1246, 2008.
[90] D. Yang, L. Tiegen, D. Zhenyang, H. Qun, L. Kun, J. Junfeng*, et al.*, "Cryogenic temperature measurement using Rayleigh backscattering spectra shift by OFDR," *IEEE Photonics Technology Letters,* vol. 26, pp. 1150-1153, 2014.
[91] X. Lu, M. A. Soto, and L. Thévenaz, "MilliKelvin resolution in cryogenic temperature distributed fibre sensing based on coherent Rayleigh scattering," in *OFS2014 23rd International Conference on Optical Fiber Sensors*, 2014, pp. 91573R-91573R-91574.
[92] D. B. Leviton and B. J. Frey, "Temperature-dependent absolute refractive index measurements of synthetic fused silica," in *SPIE Astronomical Telescopes+ Instrumentation*, 2006, pp. 62732K-62732K-62711.
[93] M. Frovel, J. M. Pintado, A. Guemes, E. D. Olmo, and A. Obst, "Multiplexable fiber Bragg grating temperature sensors embedded in CFRP structures for cryogenic applications," presented at the 3rd European Conference on Structural Health Monitoring, Granada, Spain, 2006.
[94] M. Okaji, N. Yamada, K. Nara, and H. Kato, "Laser interferometric dilatometer at low temperatures: application to fused silica SRM 739," *Cryogenics,* vol. 35, pp. 887-891, 1995.
[95] H.-J. Yoon, D. M. Costantini, H. G. Limberger, R. P. Salathé, C.-G. Kim, and V. Michaud, "In situ strain and temperature monitoring of adaptive composite materials," *Journal of Intelligent Material Systems and Structures,* vol. 17, pp. 1059-1067, 2006.
[96] C. D. Boyd, B. D. Dickerson, and B. K. Fitzpatrick, "Monitoring distributed temperatures along superconducting degaussing cables via Rayleigh backscattering in optical fibers," in *Proceedings of the Intelligent Ships Symposium IX (ISSIX) Drexel University, Philadelphia, PA USA*, 2011.
[97] G. J. Koch, "Automatic laser frequency locking to gas absorption lines," *Optical Engineering,* vol. 42, pp. 1690-1693, 2003.
[98] I. Dicaire, "Optical Gas-Phase Frequency References Based on Photonic Crystal Technology: Impact of Slow Light on Molecular Absorption," Doctoral dissertation, p. 40, 48, École Polytechnique Fédérale de Lausanne, 2012.
[99] L. W. Richards, "The infrared spectra of C2H2 and C2D2: An experiment on molecular structure and symmetry," *Journal of Chemical Education,* vol. 43, p. 644, 1966.
[100] M. Nikles, L. Thevenaz, and P. Robert, "Brillouin gain spectrum characterization in single-mode optical fibers," *Journal of Lightwave Technology,* vol. 15, pp. 1842-1851, 1997.
[101] K. Schuster, J. Kobelke, K. Rose, M. Helbig, M. Zoheidi, and A. Heinze, "Innovative fiber coating systems based on organic modified ceramics," in *Optical Components and Materials VII*, 2010, p. 75980H.

[102] T. Habisreuther, E. Hailemichael, W. Ecke, I. Latka, K. Schröder, C. Chojetzki*, et al.*, "ORMOCER coated fiber-optic Bragg grating sensors at cryogenic temperatures," *IEEE Sensors Journal,* vol. 12, pp. 13-16, 2012.

[103] Kongsberg. (July, 2016). *Platinum resistance temperature sensors Pt100 (Pt1000)*. Available: https://www.km.kongsberg.com/ks/web/nokbg0397.nsf/AllWeb/A707D00EE0F558D6C12574E1002C2D1C/$file/tsiec751_ce.pdf?OpenElement

[104] D. Sengupta, M. S. Shankar, P. S. Reddy, R. S. Prasad, K. Narayana, and P. Kishore, "An improved low temperature sensing using PMMA coated FBG," in *SPIE/OSA/IEEE Asia Communications and Photonics*, 2011, p. 831103.

[105] M. A. Soto and L. Thévenaz, "Modeling and evaluating the performance of Brillouin distributed optical fiber sensors," *Optics express,* vol. 21, pp. 31347-31366, 2013.

[106] M. D. Mermelstein, R. Posey, G. A. Johnson, and S. T. Vohra, "Rayleigh scattering optical frequency correlation in a single-mode optical fiber," *Optics Letters,* vol. 26, pp. 58-60, 2001.

[107] M.-C. Wu, R. H. Pater, and S. L. DeHaven, "Effects of coating and diametric load on fiber Bragg gratings as cryogenic temperature sensors," in *The 15th International Symposium on: Smart Structures and Materials & Nondestructive Evaluation and Health Monitoring*, 2008, p. 693303.

[108] Y.-C. Yang, H.-L. Lee, and H.-M. Chou, "Elasto-optics in double-coated optical fibers induced by axial strain and hydrostatic pressure," *Applied Optics,* vol. 41, pp. 1989-1994, 2002.

[109] F. Pigeon, S. Pelissier, A. Mure-Ravaud, H. Gagnaire, and C. Veillas, "Optical fibre Young modulus measurement using an optical method," *Electronics Letters,* vol. 28, pp. 1034-1035, 1992.

[110] F. I. NV. (2015). *DTG coating Ormocer-T for temperature sensing applications*. Available: http://www.fbgs.com/technology/why-we-have-chosen-to-use-an-ormocer-coating/

[111] D. Betz, M. Trutzel, L. Staudigel, W. Martin, and O. Krumpholz, "Fiberoptic smart sensing of component deformations in adaptive wings," in *22nd International Congress of Aeronautical Sciences*, Harrogate, United Kingdom, 2000, p. 495.

[112] K. Kishida, Y. Yamauchi, and A. Guzik, "Study of optical fibers strain-temperature sensitivities using hybrid Brillouin-Rayleigh system," *Photonic Sensors,* vol. 4, pp. 1-11, 2014.

[113] M. Buric, T. Chen, M. Maklad, P. R. Swinehart, and K. P. Chen, "Multiplexable low-temperature fiber Bragg grating hydrogen sensors," *IEEE Photonics Technology Letters,* vol. 21, pp. 1594-1596, 2009.

[114] T. Chen, Q. Wang, B. Zhang, R. Chen, and K. P. Chen, "Distributed flow sensing using optical hot -wire grid," *Optics Express,* vol. 20, pp. 8240-8249, 2012.

[115] A. M. Striegl, I. Loheide, and P. Steven, "Heated distributed temperature sensing for field scale soil moisture monitoring," *Groundwater,* vol. 50, pp. 340-347, 2012.

[116] H. G. Limberger, K. Nguyen Hong, D. M. Costantini, R. P. Salathe, C. A. P. Muller, and G. R. Fox, "Efficient miniature fiber-optic tunable filter based on intracore Bragg grating and electrically resistive coating," *IEEE Photonics Technology Letters,* vol. 10, pp. 361-363, 1998.

[117] D. M. Costantini, C. A. P. Muller, S. A. Vasiliev, H. G. Limberger, and R. P. Salathe, "Tunable loss filter based on metal-coated long-period fiber grating," *IEEE Photonics Technology Letters,* vol. 11, pp. 1458-1460, 1999.

[118] S. Gao, A. P. Zhang, H.-Y. Tam, L. Cho, and C. Lu, "All-optical fiber anemometer based on laser heated fiber Bragg gratings," *Optics Express,* vol. 19, pp. 10124-10130, 2011.

[119] X. Wang, X. Dong, Y. Zhou, Y. Li, J. Cheng, and Z. Chen, "Optical fiber anemometer using silver-coated fiber Bragg grating and bitaper," *Sensors and Actuators A: Physical,* vol. 214, pp. 230-233, 2014.

[120] B. McMillen, C. Jewart, M. Buric, K. P. Chen, Y. Lin, and W. Xu, "Fiber Bragg grating vacuum sensors," *Applied Physics Letters,* vol. 87, p. 234101, 2005.

[121] D. C. Brown and H. J. Hoffman, "Thermal, stress, and thermo-optic effects in high average power double-clad silica fiber lasers," *IEEE Journal of Quantum Electronics,* vol. 37, pp. 207-217, 2001.

[122] J. Li, K. Duan, Y. Wang, X. Cao, W. Zhao, Y. Guo*, et al.*, "Theoretical analysis of the heat dissipation mechanism in Yb3+-doped double-clad fiber lasers," *Journal of Modern Optics,* vol. 55, pp. 459-471, 2008.

[123] Y. Tanaka, T. Furusawa, M. Nakauchi, and K. Nagashima, "Heat transfer characteristics under cryogenic, low pressure environments," *Physica C: Superconductivity,* vol. 469, pp. 1862-1865, 2009.

[124] Tong Chen, Qingqing Wang, Botao Zhang, Rongzhang Chen, and K. P. Chen, "Distributed flow sensing using optical hot -wire grid," *Optics Express,* vol. 20, pp. 8240-8249, 2012.

[125] D. Coric, R. Chatton, Y. Luchessa, H. G. Limberger, R. Salathé, and F. Caloz, "Light-controlled reconfigurable fiber Bragg gratings written in attenuation fiber," in *National Fiber Optic Engineers Conference*, 2007, p. JWA17.

[126] L. Li, J. Geng, L. Zhao, G. Chen, G. Chen, Z. Fang*, et al.*, "Response characteristics of thin-film-heated tunable fiber Bragg gratings," *IEEE Photonics Technology Letters,* vol. 15, pp. 545-547, 2003.
[127] J. A. Rogers, P. Kuo, A. Ahuja, B. J. Eggleton, and R. J. Jackman, "Characteristics of heat flow in optical fiber devices that use integrated thin-film heaters," *Applied Optics,* vol. 39, pp. 5109-5116, 2000.
[128] T. R. Salamon, J. A. Rogers, and B. J. Eggleton, "Analysis of heat flow in optical fiber devices that use microfabricated thin film heaters," *Sensors and Actuators A: Physical,* vol. 95, pp. 8-16, 2001.
[129] S. Sogaard and J. Henningsen, "Thermal tuning and modulation of a DFB fibre laser with a thin-film heater," *Applied Physics B,* vol. 75, pp. 497-501, 2002.
[130] K. Kalli, H. L. Dobb, D. J. Webb, K. Carroll, M. Komodromos, C. Themistos*, et al.*, "Electrically tunable Bragg gratings in single-mode polymer optical fiber," *Optics Letters,* vol. 32, pp. 214-216, 2007.
[131] P. D. Desai, H. James, and C. Y. Ho, "Electrical resistivity of aluminum and manganese," *Journal of Physical and Chemical Reference Data,* vol. 13, pp. 1131-1172, 1984.
[132] C. N. Suryawanshi, T. Kim, and C.-T. Lin, "An instrument for evaluation of performance of heat dissipative coatings," *Review of Scientific Instruments,* vol. 81, p. 035105, 2010.
[133] M. A. Soto, S. Chin, and L. Thévenaz, "Double-pulse Brillouin distributed optical fiber sensors: analytical model and experimental validation," in *22nd International Conference on Optical Fiber Sensor*, 2012, p. 842124.
[134] Y. Nakajima, H. Tanaka, K. Mochizuki, K. Fuse, Y. Arashitani, T. Nishimoto*, et al.*, "A study for estimating thermal strain and thermal stress in optical fiber coatings," *Furukawa Review,* vol. 34, pp. 8-14, 2008.
[135] L. Mosquera, J. H. Osório, and C. M. Cordeiro, "Determination of Young's modulus using optical fiber long-period gratings," *Measurement Science and Technology,* vol. 27, p. 015102, 2015.
[136] L. Thévenaz, "Brillouin distributed time-domain sensing in optical fibers: state of the art and perspectives," *Frontiers of Optoelectronics in China,* vol. 3, pp. 13-21, 2010.
[137] M. Wuilpart, P. Megret, M. Blondel, A. J. Rogers, and Y. Defosse, "Measurement of the spatial distribution of birefringence in optical fibers," *IEEE Photonics Technology Letters,* vol. 13, pp. 836-838, 2001.
[138] Y. Lu, X. Bao, L. Chen, S. Xie, and M. Pang, "Distributed birefringence measurement with beat period detection of homodyne Brillouin optical time-domain reflectometry," *Optics Letters,* vol. 37, pp. 3936-3938, 2012.
[139] M. E. Froggatt, D. K. Gifford, S. Kreger, M. Wolfe, and B. J. Soller, "Characterization of polarization-maintaining fiber using high-sensitivity optical-frequency-domain reflectometry," *Journal of Lightwave Technology,* vol. 24, pp. 4149-4154, 2006.
[140] Y. Dong, L. Chen, and X. Bao, "Truly distributed birefringence measurement of polarization-maintaining fibers based on transient Brillouin grating," *Optics Letters,* vol. 35, pp. 193-195, 2010.
[141] M. A. Soto, X. Lu, H. F. Martins, M. Gonzalez-Herraez, and L. Thévenaz, "Distributed phase birefringence measurements based on polarization correlation in phase-sensitive optical time-domain reflectometers," *Optics Express,* vol. 23, pp. 24923-24936, Sep. 2015.
[142] M. Legre, M. Wegmuller, and N. Gisin, "Investigation of the ratio between phase and group birefringence in optical single-mode fibers," *Journal of Lightwave Technology,* vol. 21, p. 3374, 2003.
[143] T. Geisler and S. Herstrøm, "Measured phase and group birefringence in elliptical core fibers with systematically varied ellipticities," *Optics Express,* vol. 19, pp. B283-B288, 2011.
[144] D.-H. Kim and J. U. Kang, "Sagnac loop interferometer based on polarization maintaining photonic crystal fiber with reduced temperature sensitivity," *Optics Express,* vol. 12, pp. 4490-4495, 2004.
[145] D. Chowdhury and D. Wilcox, "Comparison between optical fiber birefringence induced by stress anisotropy and geometric deformation," *IEEE Journal of Selected Topics in Quantum Electronics,* vol. 6, pp. 227-232, 2000.
[146] W. Zou, Z. He, and K. Hotate, "Complete discrimination of strain and temperature using Brillouin frequency shift and birefringence in a polarization-maintaining fiber," *Optics Express,* vol. 17, pp. 1248-1255, 2009.
[147] W. Li, L. Chen, and X. Bao, "Compensation of temperature and strain coefficients due to local birefringence using optical frequency domain reflectometry," *Optics Communications,* vol. 311, pp. 26-32, 2013.
[148] C. Crunelle, M. Legre, M. Wuilpart, P. Megret, and N. Gisin, "Distributed temperature sensor interrogator based on polarization-Sensitive Reflectometry," *IEEE Sensors Journal,* vol. 9, pp. 1125-1129, 2009.
[149] A. Zornoza, D. Olier, M. Sagues, and A. Loayssa, "Brillouin distributed sensor using RF shaping of pump pulses," *Measurement Science and Technology,* vol. 21, p. 094021, Jul. 2010.

[150] K. Y. Song, W. Zou, Z. He, and K. Hotate, "Optical time-domain measurement of Brillouin dynamic grating spectrum in a polarization-maintaining fiber," *Optics Letters,* vol. 34, pp. 1381-1383, 2009.
[151] Y. Dong, X. Bao, and L. Chen, "Distributed temperature sensing based on birefringence effect on transient Brillouin grating in a polarization-maintaining photonic crystal fiber," *Optics Letters,* vol. 34, pp. 2590-2592, 2009.
[152] K. Y. Song, "High-sensitivity optical time-domain reflectometry based on Brillouin dynamic gratings in polarization maintaining fibers," *Optics Express,* vol. 20, pp. 27377-27383, 2012.
[153] K. S. Chang, "Pressure-induced birefringence in a coated highly birefringent optical fiber," *Journal of Lightwave Technology,* vol. 8, pp. 1850-1855, 1990.
[154] B. M. Welsh, "Speckle imaging signal-to-noise ratio performance as a function of frame integration time," *Journal of the Optical Society of America A,* vol. 12, pp. 1364-1374, 1995.
[155] M. A. Soto, J. A. Ramirez, and L. Thevenaz, "Intensifying the response of distributed optical fibre sensors using 2D and 3D image restoration," *Nature Communications,* vol. 7, p. 10870, 2016.

List of Acronyms

ϕOTDR	Phase-sensitive optical time-domain reflectometry
ASE	Amplified spontaneous emission
AWG	Arbitrary waveform generator
BPF	Band pass filter
BDG	Brillouin dynamic grating
BOTDA	Brillouin optical time-domain analyser
BOTDR	Brillouin optical time-domain reflectometry
CCG	Circular complex Gaussian
COTDR	Coherent optical time-domain reflectometry
CW	Continuous wave
DC	Direct current
DFS	Distributed fibre sensor
DFB	Distributed-feedback laser
ESA	Electric spectrum analyser
EM	Electromagnetic
EOM	Electro-optic modulator
EDFA	Erbium-doped fibre amplifier
FBG	Fibre Bragg grating
FUT	Fibre under test
FWM	Four-wave mixing
FWHM	Full width at half maximum
LD	Laser diode
LO	Local oscillator
MI	Modulation instability
OFDR	Optical frequency-domain reflectometry
OSA	Optical spectrum analyser
OTDR	Optical time-domain reflectometry
PC	Polarisation controller
POTDR	Polarisation optical time-domain reflectometry
PSw	Polarisation switch
PM	Polarisation-maintaining
PSD	Power spectrum density
RF	Radio frequency
SOA	Semiconductor optical amplifier
SNR	Signal-to-noise ratio

SMF	Single mode fibre
SOP	State of polarisation
SBS	Stimulated Brillouin scattering

List of Symbols

A_0	Amplitude of light
A_{eff}	Effective are of fibre
a	Radius of fibre core
B	Birefringence
b	Radius of fibre cladding
Coh	Coherence
C_p	Compressibility
C_R	Constant of receiver response
C_s	Adiabatic compressibility
c	Light speed in vacuum
c_p	Constant pressure heat capacity
d	Thickness of fibre coating
E	Electrical field
EV	Expected value
F()	Fourier transform
f	Frequency
g	Gain coefficient
H	Convective coefficient
H_E	Fibre response
h	Planck constant
I	Optical intensity
I_c	Current
K	Bulk modulus
K_B	Boltzmann constant
K_D	Thermal diffusivity
k	Wave vector of light
L	Fibre length
l_1	Outer radius of the stress-applying parts for PANDA fibre
l_2	Inner radius of the stress-applying parts for PANDA fibre
l_a	Major core radius of elliptical core fibre
l_b	Minor core radius of elliptical core fibre
M	Atom density
M'	Number of scattering points within the pulse width
N.A.	Numeric aperture
n	Refractive index
n_1	Refractive index of fibre core
n_2	Refractive index of fibre cladding
n_n	Nonlinear part of refractive index
n_x	Refractive index of slow axis
n_y	Refractive index of fast axis

P	Power
Pol.	Polarisation field
P_E	Pulse shape
P_K	Poisson coefficient
Pr	Pressure
p	Dipole moment
p_α	Dipole polarizability
Q	Heat power density
q	Wave vector of pressure wave
R	Autocorrelation
R_R	Equivalent Rayleigh reflection coefficient
r	Radius
r_R	Reflection coefficient
S	Power spectrum density
Sen	Sensitivity
$\mathbf{S_P}$	Poynting vector
S_r	Recapture factor
s	Entropy
T	Temperature
t	Time
V	Normalised frequency of fibre
V_a	Speed of sound
v_g	Group velocity
W_0	Spot size of light beam
Y	Young's modulus
z	Distance
z_R	Index correlation length

α	Fibre attenuation coefficient
α_{RS}	Fibre attenuation coefficient due to Rayleigh scattering
β	Propagation constant
Γ	Detuning factor
Γ'	Damping parameter
γ	Thermal expansion coefficient
γ_e	Electrostrictive constant
γ_r	Adiabatic index
δ	Damping rate
δ_{SB}	Stefan-Boltzmann constant
$\Delta\varepsilon$	Dielectric fluctuation
ε_0	Dielectric permittivity in vacuum
ε_e	Emissivity
ζ	Strain
η	Polarisation mixing efficiency
η_b	Bulk viscosity coefficient
η_s	Shear viscosity coefficient
κ	Thermal conductivity
Λ	Grating period for FBG
λ	Wavelength
μ_0	Magnetic permittivity in vacuum
ν	Optical frequency
ρ	Density
ρ_r	Resistivity
σ	Cross section for scattering
σ_T	Temperature resolution
τ	Temporal pulse width
τ_w	Spatial pulse width
φ	Optical phase
ϕ	Optical phase of the scattered light
χ	Dielectric susceptibility
Ω	Frequency of the acoustic wave
ω	Angular frequency

Publications

Journal papers

- M. A. Soto, **X. Lu**, H. F. Martins, M. Gonzalez-Herraez and L. Thévenaz, "Distributed phase birefringence measurements based on polarization correlation in phase-sensitive optical time-domain reflectometers," *Opt. Express*, **23**(19), 24923–24936 (2015).

Conference papers

- **X. Lu**, M. A. Soto and L. Thévenaz, "Novel technique for distributed fibre sensing based on coherent Rayleigh scattering measurements of birefringence," in 6th European Workshop on Optical Fibre Sensors, Limerick, Ireland, June 2016
- **X. Lu**, M. A. Soto and L. Thévenaz, "Characterisation of an electrical heating method for metallic-coated optical fibres for distributed sensing applications," in 6th European Workshop on Optical Fibre Sensors, Limerick, Ireland, June 2016
- **X. Lu**, M. A. Soto and L. Thévenaz, "Optimal detection bandwidth for phase-sensitive optical time-domain reflectometry," in 6th European Workshop on Optical Fibre Sensors, Limerick, Ireland, June 2016
- **X. Lu**, M. A. Soto and L. Thévenaz, "MilliKelvin resolution in distributed fibre sensing based on coherent Rayleigh scattering," oral presentation in Doctor Conference on Optics, Eisenach, Germany, Oct. 2015.
- H. F. Martins, **X. Lu**, M. A. Soto, M. Gonzalez-Herraez and L. Thévenaz, "Distributed birefringence measurements using polarisation correlation in phase-sensitive OTDR," in 40th European Conference on Optical Communication, Cannes, France, Sep. 2014.
- **X. Lu**, M. A. Soto and L. Thévenaz, "MilliKelvin resolution in cryogenic temperature distributed fibre sensing based on coherent Rayleigh scattering," oral presentation in 23rd International Conference on Optical Fibre Sensors, Santander, Spain, Jun. 2014.
- **X. Lu**, M. A. Soto and L. Thévenaz, "Brillouin distributed fibre sensing using phase modulated probe," in 5th European Workshop on Optical Fibre Sensors, Krakow, Poland, May 2013.

Xin LU

E-mail: luxin1026@gmail.com

Educational Qualifications

06.2016	PhD in Photonics *École Polytechnique Fédérale de Lausanne*
07.2011	Master in Optical engineering *University of Electronic Science and Technology of China*
07.2008	Bachelor in Optical information of science and technology *Taiyuan University of Science and Technology*

Professional Experience

Doctoral assistant — **Group for Fiber Optics**, **École Polytechnique Fédérale de Lausanne**
05.2012 – present

- Successfully completed two projects in coherent Rayleigh fiber temperature sensing for European Space Agency and International Thermonuclear Experimental Reactor
- Applied coherent Rayleigh scattering to distributed temperature and birefringence sensing, and realized mK temperature resolution and 10^{-7} birefringence accuracy
- Investigated thermal transfer for metal coated optical fibers
- Designed novel scheme to enhance the performance of fibre sensors based on Brillouin scattering
- Developed software for equipment control and data analysis in Labview and Matlab
- Authored and coauthored scientific publications, patents and project report, presented results at the highest-impact conference in the field

Research assistant — **Microelectronics division**, **Nanyang Technological University**
08.2011 – 03.2012

- Designed and fabricated novel optoelectronic devices based on graphene

Research assistant — **Key Lab of Optical Fiber Sensing & Communications**, **University of Electronic Science and Technology of China**
09.2008 – 07.2011

- Analyzed the potential of the fiber Bragg grating for dynamic dispersion compensation and magnetic field measurement
- Teaching assistant in electronics and photonics for undergraduate students

Technical and Additional Skills

Basic software	MS Office (Word, Power Point, Visio, Excel), LaTex
Data analysis	Matlab, Matplotlib
Programming	Python, Labview
Cleanroom skills	Wet-etching, sputtering, wire-bonding, photolithography, etc.
Language	Chinese (native speaker), English (working language), French (basic)

Interests

Sports	Swimming, badminton, football, hiking
Online learning	Politics, economy, data science, management